# DISSERTATION

# NEW FLUORESCENCE TECHNIQUE TO SEARCH FOR NEUTRINO MASSES BY IDENTIFICATION OF $0\nu\beta\beta$ DECAY $^{136}Ba^{+}$ ION DAUGHTERS IN LIQUID XENON


**Submitted by**

**Shie-Chang Jeng**

**Department of Physics**


**In partial fulfillment of the requirements**

**for the Degree of Doctor of Philosophy of Science**

**Colorado State University**

**Fort Collins, Colorado**

**Spring, 2004**

INFORMATION TO USERS

The quality of this reproduction is dependent upon the quality of the copy submitted. Broken or indistinct print, colored or poor quality illustrations and photographs, print bleed-through, substandard margins, and improper alignment can adversely affect reproduction.

In the unlikely event that the author did not send a complete manuscript and there are missing pages, these will be noted. Also, if unauthorized copyright material had to be removed, a note will indicate the deletion.



ProQuest Information and Learning Company
300 North Zeeb Road
P.O. Box 1346
Ann Arbor, MI 48106-1346

COLORADO STATE UNIVERSITY

JANUARY 29, 2004

WE HEREBY RECOMMEND THAT THE DISSERTATION PREPARED UNDER OUR SUPERVISION BY SHIE-CHANG JENG ENTITLED NEW FLUORESCENCE TECHNIQUE TO SEARCH FOR NEUTRINO MASSES BY IDENTIFICATION OF $0\nu\beta\beta$ DECAY $^{136}Ba^{+}$ ION DAUGHTERS IN LIQUID XENON BE ACCEPTED AS FULFILLING IN PART REQUIREMENTS FOR THE DEGREE OF DOCTOR OF PHILOSOPHY.

Committee on Graduate Work

Adviser

Department Head

# ABSTRACT OF DISSERTATION

## NEW FLUORESCENCE TECHNIQUE TO SEARCH FOR NEUTRINO MASSES BY IDENTIFICATION OF $0\nu\beta\beta$ DECAY $^{136}Ba^{+}$ ION DAUGHTERS IN LIQUID XENON

This work presents the initial research on the development of a new fluorescence technique for laser tagging of single $^{136}Ba^{+}$ daughters from $0\nu\beta\beta$ decay of $^{136}Xe$. $0\nu\beta\beta$ decay is the only probe which is able to reach the absolute neutrino mass scale with meV sensitivity. The current limit of mass sensitivity is about 0.33-1.5 eV, and the next generation $0\nu\beta\beta$ experiments with meV sensitivity require new techniques for background rejection in order to gain the full benefit of large fiducial mass and long running time. By detecting the decay daughter $Ba^{+}$ in liquid xenon at the observed position of the decay, we expect to suppress essentially all of the radioactive backgrounds. As a first step in realization this technique, the measurement of the mobility of $Ba^{+}$ in liquid xenon is finished and the study of the optical spectra of $Ba^{+}$ in liquid xenon is in progress.

In this work, measurements of the mobility of alkaline earth ions, $Mg^{+}$, $Ca^{+}$, $Sr^{+}$, and $Ba^{+}$, in liquid xenon are presented for the first time. The mobility of $Tl^{+}$ is also measured in order to make a comparison to the reported value by others with a different measurement system. Akins's cluster model of positive ions in non-polar liquids, based on the electrostriction effect, gives general agreement with the magnitude of the mobility values. This might indicate that the positive ions form a snowball structure in liquid xenon.

The excitation and fluorescence spectra of $Ba^{+}$ in liquid xenon are also observed for the first time. The evidence that $Ba^{+}$ does fluoresce in liquid xenon is a positive sign for

achievement of the long-term goal. The spectra show much narrower absorption width and smaller emission shift compared to alkali atoms in solid noble gas matrix. Agreement is better with the spectra of $Ca^+$ in solid argon. More detailed and careful experimental data will be required for a full understanding of the spectra properties of $Ba^+$ in liquid xenon.

Shie-Chang Jeng
Physics Department
Colorado State University
Fort Collins, CO 80523
Spring, 2004

# ACKNOWLEDGMENTS

This thesis work is the result of many help from others. I would like to thank my adviser, Dr. William M. Fairbank, Jr., for his support and guidance in the past 6 years. He provided me an opportunity to begin this interesting application of laser spectroscopy to the forefront topic of neutrino physics. I also like to thank Dr. Siu Au Lee for her a lot of assistance over the years. Dr. Mitsuhiro Miyajima and his students, Hidemi Nawa, helped me a lot when I stayed in Japan for two months. I appreciate very much for their help and hospitality.

I also like to thank my committee members, Dr. Stephen R. Lundeen, Dr. Robert J. Wilson and Dr. Alan Van Orden for their time to revise my thesis and to provide their helpful suggestions.

I have got assistance from members in laser group. I appreciate their help very much. I also like to thank high pressure group for their generous loan of optics.

I had the great fortune to work with an excellent machine shop manager, Bob Adame. His help made my homemade parts working very well and contributed to the success of my experiment.

Lastly, I thank my parents for their patience and support for my any decision.

# Table of Contents

# Chapter 1

## Introduction

The existence of the neutrino was first postulated by Pauli in 1930 for explaining the continuous $\beta$-spectrum in nuclear beta decay [1], and the electron antineutrino was first observed by Cowan and Reines using the reaction $\bar{\nu}_e p \rightarrow e^+ n$ in 1956 [2]. Although the neutrino was born 70 years ago, it is still the most unknown particle among the Standard Model. The Standard Model of particle physics is a theory of the strong, weak and electromagnetic interactions conceived by Glashow, Salam, and Weinberg in the 1960s, and it has successfully passed numerous experimental tests [3]. Neutrinos were introduced in the Standard Model as left-handed neutral fermions without mass since there was no direct evidence for their mass at that time and no gauge-invariant renormalizable mass term could be constructed. Consequently, there is neither mixing nor CP violation in the lepton sector. There are three flavors of neutrinos in the Standard Model: the electron neutrino ($\nu_e$), the muon neutrino ($\nu_\mu$) and the tau neutrino ($\nu_\tau$). The measurement of the decay width of the $Z$ boson into neutrinos confirmed the existence of three and only three flavors of neutrinos [3]. The Standard Model also treats the neutrinos as Dirac particles, that is, they are distinct from their antiparticles. Various extensions of the Standard Model, such as the grand unified theories, predict that right–handed neutrinos exist through the Yukawa interaction with a finite mass, and also suggest the neutrinos might be Majorana particles, which mean that neutrinos are identical to their antiparticles [4]. Experimental evidence for neutrinos masses, mixing, and leptonic CP

violation will provide an unambiguous signature of new physics beyond the Standard Model and might also answer some questions in particle physics and cosmology.

Various theoretical models have suggested the mass scale of neutrino mass is on the order of 0.01-1 eV [5]. Three types of experiments have been conducted to search for neutrinos mass with this level of sensitivity: neutrino oscillations, kinematics of weak decay, and double beta decay [4]. Although the experiments of neutrino oscillations can reach mass sensitivity as low as $10^{-5}$ eV, only the difference of neutrinos masses squared is determined. Kinematics of weak beta decay, pion decay and tau decay have been used to study the upper limits of mass for $\nu_e$, $\nu_\mu$, and $\nu_\tau$, of which the most sensitive experiment is the study of tritium beta decay [6]. The most precise result from tritium beta decay has set the upper bond of electron neutrino mass on the order 2.2 eV [7]. It is expected that the sensitivity can be improved to the order of 0.2 eV in the future [8]. Neutrinoless double beta decay ($0\nu\beta\beta$) is the only experiment can measure the absolute neutrino mass with the sensitivity better than 0.1 eV. The sensitivity of the best $0\nu\beta\beta$ experiment to date is 0.33-1.35 eV [9,10]. It is expected that this limit can be improved to 0.01 eV in the future with a large-scale experiment [11]. The mass sensitivity of such an experiment is proportional to $1/(Nt)^{1/2}$ without background and $1/(Nt)^{1/4}$ with background scaled as $Nt$, where $N$ is the number of nuclei in the experiment and $t$ is the duration of the experiment. It is clear that there is much more gain in going to larger and larger experiments if the background is reduced to zero. Thus, the next generation $0\nu\beta\beta$ experiments require new techniques for background rejection in order to gain the full benefit of large mass and time. The exploration of a new technique for background

elimination in a liquid xenon $0\nu\beta\beta$ experiment is the subject of this thesis, and the decay of interest is $^{136}Xe \rightarrow {}^{136}Ba^{++} + 2e^{-}$.

The leading $0\nu\beta\beta$ decay experiments detect the electron pulses from the two $\beta$ particles only, and background discrimination relies on good energy resolution, pulse shape and tracking information [9,10]. Even for few kg size experiments with one year of duration, these methods have not been sufficient for complete background elimination. A new technique based on tagging of daughter $Ba^{+}$ ion from double beta decay of $^{136}Xe$ with laser-induced fluorescence was first proposed by Moe in 1991 [12], and has been considered by Miyajima and the EXO collaboration [13,14]. Evidence for the existence of the daughter $^{136}Ba^{+}$ ion near the decay site will provide the unambiguous signature for the true decay event, and a large-scale background-free experiment is thought possible with this additional signature.

The main purpose of this thesis work is to investigate the unique technique for tagging a $Ba^{+}$ ion in liquid xenon with lasers. In particular, it is necessary to understand how the $Ba^{+}$ ion moves in liquid xenon, i.e., measure its mobility, and to confirm that a $Ba^{+}$ ion does fluoresce after laser excitation in liquid xenon by measuring its excitation and emission spectra. This thesis is divided into eight chapters. Chapter two is a brief overview of the neutrino physics and experimental efforts to search for neutrino mass. Our proposed concept to realize this new fluorescence technique is also discussed. Chapter three discusses the theory of ion transport, fluid motion and ion structure in liquid xenon. Chapter four summarizes laser spectroscopy results to date for various atoms and a few ions in liquid helium and in solid noble gas matrices. Based on these results, an educated guess for the spectra of $Ba^{+}$ ion in liquid xenon is presented. Chapter

five describes the cryogenic and purification systems and the various detection methods for mobility and laser spectroscopy measurements. In Chapter six and Chapter seven, our experimental results for mobility measurement and the spectroscopy of $Ba^+$ ion in liquid xenon, respectively, are presented and discussed. Chapter six also summarizes all the mobility measurements of alkaline earth ions, $Mg^+$, $Ca^+$, $Sr^+$ and $Ba^+$, and $Tl^+$. Finally, Chapter eight summarizes the major results of this work. Some improvements are suggested, and the studies required for the final goal of a demonstration of the detection of single $Ba^+$ ion in liquid Xe are also described.

# References


1. W. Pauli, transl. in L.M. Brown, Phys. Today, Sept. 23 (1978).
2. C.L. Cowan, Jr., F. Reines, F.B. Harrison, H.W. Kruse, and A.D. McGuire, Science 124, 103 (1956).
3. R.M. Barnett et al., Rev. Mod. Phys. 68, 611 (1996).
4. K. Zuber, Phys. Reports 305, 295 (1998).
5. S.M. Bilenky et al., Phys. Rev. D 64, 053010 (2001).
6. J.F. Wilkerson and R.G.H. Robertson, Current Aspects of Neutrino Physics, Chapter 3, Springer-Verlag, 1st Edition, 2001.
7. J. Bonn et al., Nucl. Phys. B (Proc. Suppl.) 110, 395 (2002).
8. C. Weinheimer, Nucl. Phys. B (Proc. Suppl.) 118, 279 (2003).
9. H.V. Klapdor-Kleingrothaus et al., Eur. Phys. J. A 12, 147 (2001).
10. C. E. Aalseth et al., Phys. Rev. D 65, 092007 (2002)
11. S.R. Elliott and P. Vogel, Annu. Rev. Nucl. Part. Sci. 52, 115 (2002).
12. M.K. Moe, Phys. Rev. C 44, R931 (1991).
13. M. Miyajima et al., KEK proceedings 91-5, 19 (1991).
    M. Miyajima et al., IEEE Trans. Nucl. Sci. 41, 835 (1994).
14. Danilov M et al., Phys. Lett. B 480, 12 (2000).

# Chapter 2

## Neutrinos Physics and Double Beta Decay

This chapter provides background information on neutrino physics, various experiments to search for neutrino mass and the proposed $Ba^+$ tagging method. Neutrino oscillations are discussed in Section 2-1. In Section 2-2, kinematic methods to search for neutrino mass are reviewed. Limits on neutrino mass from cosmic structure formation are briefly discussed in Section 2-3. Double beta decay is discussed in Section 2-4, and the last section, Section 2-5, outlines our proposed fluorescence technique to detect the single $Ba^+$ ion daughter in liquid xenon.

### 2-1 Neutrino oscillations

Bruno Pontecorvo first realized that the existence of neutrino masses implied the possibility of neutrino oscillations [1]. If neutrinos are massive particles, which behave in analogy to quarks, the states with a definite mass (mass eigenstates) are not necessarily the same as the weak eigenstates that participate in electroweak interactions. In other words, the weak eigenstates $|\nu_l\rangle$ ($l$=$e,\mu,\tau$) will be linear superposition of the mass eigenstates $|\nu_i\rangle$ ($i$=1,2,3) as given by

$$|\nu_l\rangle = \sum_i U_{l,i}|\nu_i\rangle, \qquad 2\text{-}1$$

where the coefficients $U_{l,i}$ is the leptonic mixing matrix. In the phenomena of neutrino oscillations, a neutrino created initially in weak eigenstate $|\nu_l\rangle$ can become mixed with other weak eigenstates as it evolves in time. For a simplified case with predominantly

two-neutrino mixing, $\nu_e$ and $\nu_\mu$ and $m_1$ *and* $m_2$, for example, the mixing matrix U can be written in terms of the mixing angle $\theta$ as

$$U = \begin{pmatrix} \cos\theta & \sin\theta \\ -\sin\theta & \cos\theta \end{pmatrix}. \qquad 2\text{-}2$$

The oscillation probability for travel in free space over a distance L is given by

$$P(\nu_e \rightarrow \nu_\mu, L) = \sin^2 2\theta \sin^2(\Delta m^2 L/4E), \qquad 2\text{-}3$$

where $\Delta m^2 \equiv m_1^2 - m_2^2$, and $E$, and $m_{1,2}$ are the neutrino energy and the masses of the two mass eigenstates. There have been numerous experiments to search for neutrino oscillations for the last three decades [2]. Experiments are classified according to the source of the neutrinos: nuclear fusion reaction in the sun, by-products of cosmic-ray collisions in the atmosphere, and production in reactors or accelerators. The SuperKamiokande, Sudbury Neutrino Observatory (SNO) and Kamioka Liquid-scintillator Anti-Neutrino Detector (KamLand) have reported the strongest evidence of neutrino oscillations in recent years [3,4,5].

**2-1-1 Solar neutrinos**

In the solar neutrino experiments, electron neutrinos are produced by the thermonuclear reactions in the center of the sun. The Standard Solar Model (SSM) has been well developed, so the flux and energy spectrum of the solar neutrinos can be fairly confidently predicted. The pioneering experiment in neutrino astrophysics was the chlorine solar neutrino experiment conducted by R. Davis in the Homestake Mine in South Dakota. The detection reaction is $^{37}Cl + \nu_e \rightarrow {}^{37}Ar + e^-$, and the numbers of $^{37}Ar$ are counted roughly every two months. First published in 1970, the current average measured neutrino flux is 2.56±0.16 (stat.)±0.16 (sys.) SNU, where one SNU is defined

as $10^{-36}$ captures per target atom per second [6]. This is approximately one third of the SSM prediction. In the early days, this discrepancy was called "the solar neutrino problem". Two other similar experiments, SAGE and GALLEX/GNO, using $^{71}$Ga targets, started taking data in the early 1990s, and confirmed that the "solar neutrino problem" does exist. Their results were reported as $R_{SAGE} = 67.2^{7.2+3.5}_{-7.0-3.0}$ SNU [7] and $R_{GALLEX+GNO} = 71 \pm 6 \pm 3.0$ SNU [8], while the prediction of the SSM is 130 SNU.

The first real time solar neutrino detection experiment led by M. Koshiba was a Cerenkov detector with 2140 tons of water located in the Kamioka mine in Japan. The detector could detect electrons scattered from the water by elastic interaction of the solar neutrinos in real time by the reaction, $\nu_x + e^- \rightarrow \nu_x + e^-$ ($\nu_x$=$\nu_e$, $\nu_\mu$, $\nu_\tau$). The scattered electrons emit Cerenkov light detected by photomultipliers. The results of Kamiokande and its successor SuperKamiokande were given as [3]

$$\Phi_{Kam} = (2.80 \pm 0.19 \pm 0.33) \times 10^6 cm^{-2} s^{-1}$$
$$\Phi_{SK} = (2.42 \pm 0.06^{+0.10}_{-0.07}) \times 10^6 cm^{-2} s^{-1},$$

which correspond to about 40-50% of the SSM prediction.

SNO is another detector with about 1000 tons of heavy water located in the Sudbury Mine in Canada. SNO was designed to give sensitivity to all flavors of active neutrinos and not just to $\nu_e$. Electron neutrinos may interact via the charged-current (CC) reaction, $\nu_e + d \rightarrow p + p + e^-$, and all active neutrinos $\nu_x$ interact via the neutral-current (NC) reaction, $\nu_x + d \rightarrow n + p + \nu_x$, and electron elastic scattering (ES) reaction, $\nu_x + e^- \rightarrow \nu_x + e^-$. The main feature of SNO is its capability to detect the NC reaction, in which all three neutrino flavors have the same cross section. Therefore, any significant

difference between the neutrino fluxes as measured by the CC and NC reactions is an unambiguous signal of neutrino oscillations. The results were reported as [4]

$$\Phi_{CC} = (1.76^{0.06}_{-0.05} \pm 0.09) \times 10^6 cm^{-2} s^{-1}$$

$$\Phi_{NC} = (5.09^{+0.44+0.46}_{-0.43-0.43}) \times 10^6 cm^{-2} s^{-1}$$

$$\Phi_{ES} = (2.39 \pm 0.24 \pm 0.12) \times 10^6 cm^{-2} s^{-1}.$$

The flux of the NC interaction is in excellent agreement with the predicted flux by SSM, $5.05^{+0.2}_{-0.16} \times 10^6 cm^{-2} s^{-1}$, and the low CC flux indicates that $\nu_e$ oscillates directly to $\nu_\mu$ or $\nu_\tau$ neutrinos.

All of the solar neutrino experiments show the disappearance of $\nu_e$. This deficit is more easily explained by neutrino oscillations rather than by modifying the well-understood SSM. The results from SNO confirm that the electron neutrino changes flavor in the travel from the Sun to the Earth.

**2-1-2 Atmospheric neutrinos**

Atmospheric neutrinos are produced in a cascade initiated by collisions of cosmic rays with the Earth's atmosphere. Pions are produced in these collisions, and then subsequently decay via $\pi \rightarrow \mu + \nu_\mu$ and $\mu \rightarrow e + \nu_e + \nu_u$. The ratio of neutrinos of different flavor $\nu_\mu : \nu_e = 2:1$ is expected. Atmospheric neutrinos were first observed in 1960s, and the results did not show significant difference from theoretical predictions [2]. The first formulation of the atmospheric neutrino anomaly, in which the measured $\nu_\mu/\nu_e$ ratio was noticeably small, only about 60 % of the expected value of 2, was reported in 1992 by two water Cerenkov detectors, IMB [9] and Kamiokande [10]. The zenith angular dependence of the deficit was also measured in Kamiokande, and it suggested

that the deficit increases with the distance between the neutrino production and interaction points ranging from ~ 15 km above the detector to ~$10^4$ km below the detector [3]. The iron calorimeter detectors, Soudan2 [11] and MACRO [12], have also confirmed the atmospheric neutrino anomaly in recent years. The scenario involving $\nu_\mu \rightarrow \nu_\tau$ oscillations is preferred to explain the atmospheric neutrino anomaly.

Due to their pioneering contributions to astrophysics, in particular for the detection of cosmic neutrinos, Davis and Koshiba won the 2002 Nobel Prize in Physics.

**2-1-3 Laboratory neutrinos**

"Laboratory" neutrinos generated by accelerators or nuclear reactors have also been used to search for neutrino oscillations. Only two positive results were reported so far. In the Liquid Scintillator Neutrino Detector (LSND) running in Los Alamos, two possible oscillation channels, $\bar{\nu}_\mu \rightarrow \bar{\nu}_e$ and $\nu_\mu \rightarrow \nu_e$, were reported for muon neutrinos produced by pion and muon decay [13,14]. These appearance experiments measure the flux of electron neutrinos, which should be absent if muon neutrinos do not oscillate. Because the short distance of L (~30m), the results from LSND give evidence for a much larger mass square difference ($0.2 < \Delta m^2 < 2.0$ $eV^2$) than the others. At present, these results are quite controversial. If confirmed in the future, a fourth sterile neutrino might need to be included in the theoretical model. A new experiment called MiniBooNE, the first phase of BooNE (Booster Neutrino Experiment), is in progress to confirm or refute the LSND experiment [15].

Recently, the evidence for reactor antineutrino disappearance on the 150-200 km distance scale has been reported from KamLand. By measuring the flux of $\bar{\nu}_e$ from distant reactors, the KamLAND collaboration showed that the ratio of the observed

inverse β-decay events to the number of events expected without oscillation is 0.661±0.094. The deficit can be interpreted in terms of $\overline{\nu}_e$ oscillations to $\overline{\nu}_x(\overline{\nu}_\mu,\overline{\nu}_\tau)$ [5].

In summary, strong evidence for neutrino oscillations has been shown in various experiments in recent years. Conclusions of a global analysis of the solar and atmospheric data by Gonzalez-Garcia *et. al.* in terms of three-neutrino oscillations are summarized in Table 2-1. The best fit results of mass squared difference and mixing angle are given based on large mixing angle (LMA) solution, which provides the best description of neutrino oscillations [16].

**Table 2-1 Limits on the $\Delta m^2$, mixing angle and best fit from global fitting [16].**

| Experiment | $\Delta m^2$ ($eV^2$) | $\tan^2\theta$ | best-fit of $\Delta m^2$ ($eV^2$) | best-fit of $\tan^2\theta$ |
|---|---|---|---|---|
| Solar (LMA) | $1\times10^{-5}<\Delta m^2_{21}<1\times10^{-3}$ | $0.1<\tan^2\theta_{12}<10$ | $3.3\times10^{-5}$ | $\tan^2\theta_{12}=0.37$ $\tan^2\theta_{13}=0.0$ |
| Atmospheric | $1.6\times10^{-3}<\Delta m^2_{32}<6\times10^{-3}$ | $0.43<\tan^2\theta_{23}<4.2$ $\tan^2\theta_{13}<0.34$ | $3.3\times10^{-3}$ | $\tan^2\theta_{13}=0.025$ $\tan^2\theta_{23}=1.6$ |

## 2-2 Kinematic search for neutrino mass

Probing neutrino mass through direct measurements of decay kinematics includes studies of the shape of beta decay spectra, measurements of muon momentum in pion decay, and invariant-mass studies of multiparticle semileptonic decays of the tau $\tau$ [17]. To date, only upper limits of neutrinos masses have been obtained. Among of them, the best limit is for $\nu_e$ by the tritium beta decay experiment. The technique is based on

measuring the distortion in the shape of the beta spectrum in the endpoint energy region. The number of decays in this region for the case of nonzero neutrino mass will be less than that expected in the case of a massless electron neutrino. The current upper limits on neutrino mass in these experiments are presented in Table 2-2 [18-20]. The upper limit for the electron neutrino mass is 2.2 eV, and the limit for the masses of $\nu_\mu$ and $\nu_\tau$ are much higher. The limit for $m_{\nu e}$ might be improved one order of magnitude in the future [21].

**Table 2-2 Neutrino mass limits from kinematic search.**

| Neutrino | mass limit | experiment [Ref.] |
|---|---|---|
| $\nu_e$ | < 2.2 eV | Mainz [18] |
| $\nu_\mu$ | < 170 eV | [19] |
| $\nu_\tau$ | < 18.2 MeV | Aleph [20] |

## 2-3 Cosmological limit on the neutrino mass

The Big Bang model predicts the existence today of not only a relic photon background but also a relic neutrino background from atomic and nuclear synthesis. The predicted contribution of massive neutrinos to the matter density in the present universe is given as $0.0108\Sigma m_\nu/h^2$ eV, where $\Sigma m_\nu$ is the total mass of various types of neutrinos, and $h=H_0/100 kms^{-1}Mpc^{-1}$ is the normalized Hubble constant [22]. A careful analysis of constraints on the neutrino mass from current cosmological dada provides an upper limit on $\Sigma m_\nu$, given as 2.5~3 eV [23]. At present, the questions of the quantity and composition of dark matter in the galaxy and the universe are forefront topics in physics. The experimental determination of individual neutrino masses in the future will be important to our understanding of cosmology and astrophysics.

## 2-4 Double beta decay

Double beta decay is a rare second-order weak interaction process in which the nuclear charge changes by two units while the mass number remains the same. Three possible decay channels for the double beta decay are

$$(Z,A) \rightarrow (Z+2,A)+2e+2\bar{\nu}_e, \quad 2\text{-}4$$

$$(Z,A) \rightarrow (Z+2,A)+2e, \quad 2\text{-}5$$

$$(Z,A) \rightarrow (Z+2,A)+2e+X, \quad 2\text{-}6$$

The Feynman diagrams for these three decays are illustrated in Fig. 2-1.

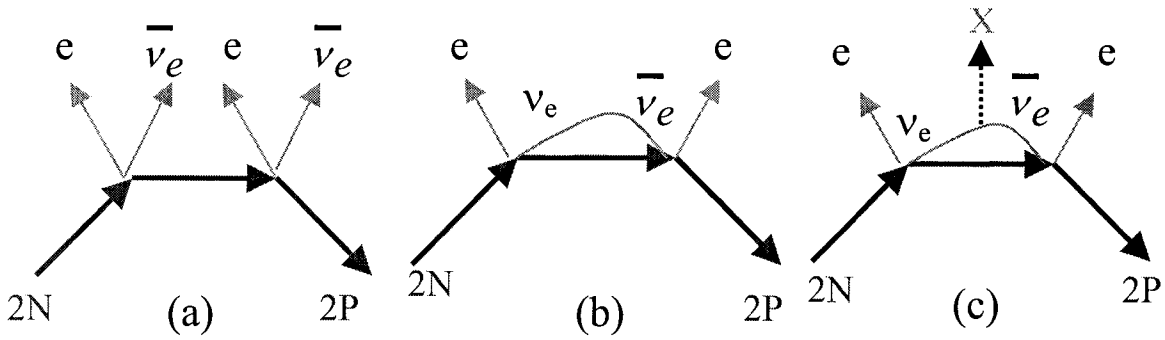


**Figure 2-1 Double beta decay: (a) $2\nu\beta\beta$ (b) $0\nu\beta\beta$ (c) $0\nu\beta\beta$ with $X$ emission.**

Process 2-4 is called $2\nu\beta\beta$ decay. Two neutrons decay into two protons, two electrons and two anti-neutrinos. Lepton number is conserved in this process, and it is allowed in the Standard Model. $2\nu\beta\beta$ decay has been observed in about a dozen different isotopes, but it has not been observed for xenon. The measured lifetimes and the two main theoretical predictions of the quasiparticle random phase approximation (QRPA) model and the nuclear structure model (NSM) are summarized in Table 2-3. The agreement between different theoretical predictions and between theory and experimental

results is generally not better than a factor of 2 or 3. The measured results can be used to improve the theory leading to better accuracy for determining nuclear transition matrix elements.

**Table 2-3 Summary of experimentally measured $2\nu\beta\beta$ half-lives and theoretical predictions.**

| Isotope | $T_{1/2}^{2\nu}$(y) | Reference | QRPA[49] | NSM[50] |
|---|---|---|---|---|
| $^{48}$Ca | $(4.2\pm1.2)\times10^{19}$ | [25,26] | | $5.5\times10^{19}$ |
| $^{76}$Ge | $(1.3\pm0.1)\times10^{21}$ | [27-29] | $3.0\times10^{21}$ | $2.2, 3.6\times10^{21}$ |
| $^{82}$Se | $(9.2\pm1.0)\times10^{19}$ | [30,31] | $1.1\times10^{20}$ | $5.0, 8.0\times10^{21}$ |
| $^{96}$Zr | $1.4^{+3.5}_{-0.5}\times10^{19}$ | [32-34] | $1.1\times10^{19}$ | |
| $^{100}$Mo | $(8.0\pm0.6)\times10^{18}$ | [35-40] | $1.1\times10^{18}$ | |
| $^{116}$Cd | $(3.2\pm0.3)\times10^{19}$ | [41-43] | $6.3\times10^{19}$ | |
| $^{128}$Te | $(7.2\pm0.3)\times10^{24}$ | [43,45] | $2.6\times10^{24}$ | |
| $^{130}$Te | $(2.7\pm0.1)\times10^{21}$ | [44] | $1.8\times10^{21}$ | $2.3\times10^{20}$ |
| $^{136}$Xe | $>8.1\times10^{20}$ (90% CL) | [46] | $4.6\times10^{21}$ | $1.7\text{-}2.0\times10^{21}$ |
| $^{150}$Nd | $7.0^{+11.8}_{-0.3}\times10^{18}$ | [38,47] | $7.4\times10^{18}$ | |
| $^{238}$U | $(2.0\pm0.6)\times10^{21}$ | [48] | $1.5\times10^{23}$ | |

Process 2-5 is $0\nu\beta\beta$ decay, where no neutrino exists at the final state. It violates conservation of lepton number and is therefore forbidden in the Standard Model. Process $0\nu\beta\beta$ only happens if the neutrino and antineutrino are identical particles and they have nonzero neutrino mass. One can see in Fig. 2-1(b), a virtual $\overline{\nu}_e$ changes into a virtual $\nu_e$, making this decay happen. In process 2-6, a hypothetical scalar particle $X$ called a Majoron, associated with spontaneous breaking of the baryon-lepton (B-L) symmetry, is emitted in this $0\nu\beta\beta X$ decay. Neither type of $0\nu\beta\beta$ decay has been observed. The present lifetime limits for $0\nu\beta\beta$ and effective neutrino mass $\langle m_\nu \rangle$ limits are summarized in Table 2-4.

**Table 2-4 Best reported limits on $T_{1/2}^{0\nu}$**

| Isotope | $T_{1/2}^{0\nu}$ ($10^{22}$ years) (C.L.(%)) | $<m_\nu>$ (eV) | Reference |
|---|---|---|---|
| $^{48}$Ca | >0.95(76) | <8.3 | [42] |
| **$^{76}$Ge** | **>1900(90)** | **<0.35** | [18] |
| | **>1600** | **<0.35-1.35** | [43] |
| $^{82}$Se | >2.7(68) | <5 | [21] |
| $^{100}$Mo | >5.5(68) | <2.1 | [44] |
| $^{116}$Cd | >7(90) | <2.6 | [33] |
| **$^{128}$Te** | **>770(90)** | **<1.1-1.5** | [35] |
| **$^{130}$Te** | **>144(90)** | **<1.1-2.6** | [45] |
| **$^{136}$Xe** | **>44(90)** | **<1.8-5.2** | [46] |
| $^{150}$Nd | >0.12(90) | <3 | [29] |

Experimentally, it is possible to distinguish the three types of double beta decay by measuring the spectrum of the total energy of the two electrons, as schematically illustrated in Fig. 2-2. For the $0\nu\beta\beta$, the two electrons carry all the decay energy $E_0$, so a sharp peak at $E=E_0$ can be observed. For $2\nu\beta\beta$ decay and $0\nu\beta\beta X$ decay, the neutrinos or the Majoron $X$ carry some of the decay energy, and there is a broad peak in the total electron energy spectra. Good energy resolution is required in $\beta\beta$ experiments in order to distinguish these three different decay channels.

If $0\nu\beta\beta$ decay occurs, the effective Majorana neutrino mass $<m_\nu>$ is related to the half-life $T_{1/2}^{0\nu\beta\beta}$ as [22]:

$$< m_\nu >^2 = (T_{1/2}^{0\nu\beta\beta} G^{0\nu\beta\beta}(E_0, Z) \left| M_{GT}^{0\nu\beta\beta} - \frac{g_V^2}{g_A^2} M_F^{0\nu\beta\beta} \right|^2 )^{-1}, \qquad 2\text{-}7$$

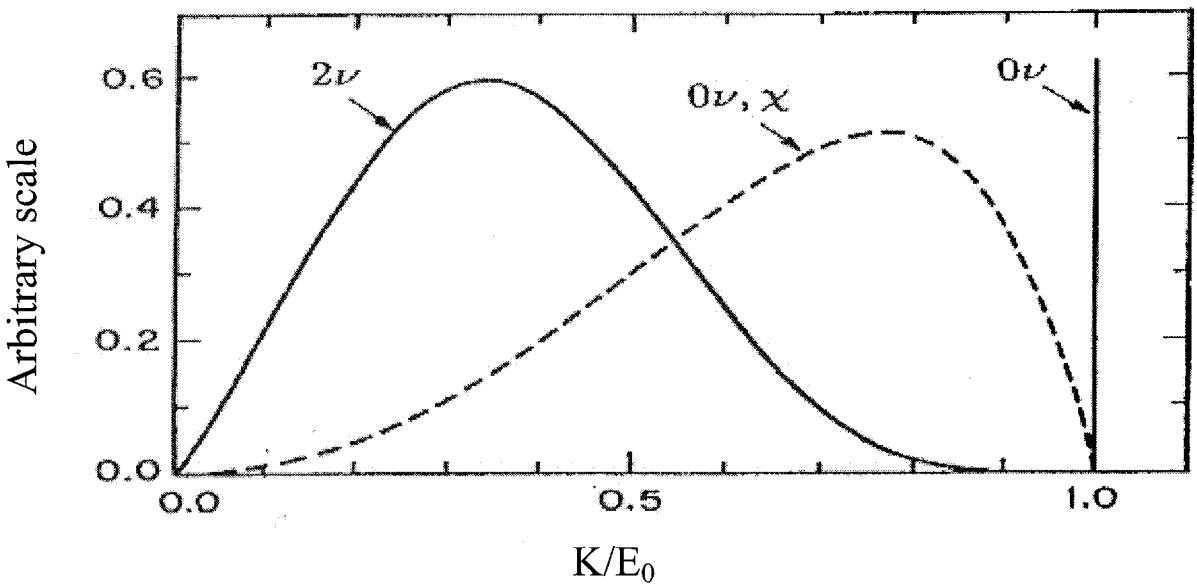


**Figure 2-2. Total electron energy spectra for $2\nu\beta\beta$, $0\nu\beta\beta$ and $0\nu\beta\beta X$ decay.**

where $G^{0\nu\beta\beta}(E_0,Z)$ is a known phase space factor depending on the decay energy $E_0$ and nuclear charge $Z$, and $M_{GT}^{0\nu\beta\beta}$ and $M_F^{0\nu\beta\beta}$ are the Gamow-Teller and Fermi nuclear matrix elements. The effective Majorana neutrino mass $<m_\nu>$ is given by

$$< m_\nu >= \sum m_i U_{ei}^2, \qquad 2\text{-}8$$

where $U$ is the neutrino mixing matrix and $m_i$ are the masses of the neutrino mass eigenstates. Dozens of $0\nu\beta\beta$ decay experiments have been conducted in the past, and no positive result has been observed. Recently, Klapdor-Kleingrothaus *et al.* (Heidelberg-Moscow group) claimed that they have observed the evidence of $0\nu\beta\beta$ of $^{76}$Ge, and the best fitting result of $<m_e>$ is 0.35 eV [56]. However, the result is controversial, and it has not been accepted by the double beta decay community [56].

The lifetime and neutrino mass limit to date for the most sensitivity $0\nu\beta\beta$ experiments are also highlighted in Table 2-4. For a next generation large-scale double beta decay experiment, xenon is particular interesting among them for several reasons:

1. Xenon is in the gas phase at STP and thus is easy to transfer and enrich.

2. Xenon is a good ionization medium, and exhibits substantial scintillation.

3. Xenon is chemically inert, so it can be easily purified with different ways involving molecular sieves, hot metal getters and electric spark.

4. Most importantly for our purpose, xenon gas and liquid are transparent in the visible range, and a new fluorescence technique can be applied to identify the decay daughter.

Future experiments will requires $10^4$-$10^8$ times more mass to reach 0.01 eV sensitivity of neutrino mass if present techniques are merely scaled up. However, only $10^2$-$10^4$ times larger experiments are required if background events can be suppressed completely. Single $Ba^+$ ion tagging with lasers might be realized either in gaseous or in liquid xenon. We propose to detect the double beta decay of $^{136}Xe$ in the liquid phase because the liquid is more compact in size and the energy resolution in liquid xenon is about 2 times better than in gaseous xenon [55,57].

## 2-5 Principle of $Ba^+$ tagging in xenon double beta decay detector

To tag the daughter $Ba^+$ ion from double beta decay of $^{136}Xe$ by laser induced fluorescence was first proposed by Moe in 1991 [58], and has been considered in more experimental detail by Miyajima and the EXO group [59,60]. The technique is based on single atom detection with lasers, which has been realized for 3 decades [61-64]. The basic idea is that a single atom can absorb resonant laser light up to $10^7$-$10^8$ times per second and will emit fluorescence photons at the same rate so that a burst of photon

counts can be recorded in a short time. Detection of a single barium ion in vacuum by this method using a quadrupole RF trap was first realized in 1978 by Dehmelt [65]. However, the atomic resonance of atoms or ions will be greatly broadened and a very high laser power will be required to reach the same burst rate in liquid environment. The stray light (Rayleigh and Brillouin scattering) is also larger in liquid. Thus, detection of a single atom or ion in liquid has not been realized yet. Nevertheless, the observation time can be greater in the liquid because the atom or ion moves very slowly, and stray light can be blocked efficiently because the emission is red-shifted in wavelength. Consequently, single atom or ion detection in a liquid seems possible. The principles of this technique to tag $Ba^+$ in a time projection chamber (TPC) of liquid xenon are discussed in more detail in the following paragraphs.

The general concept for the $Ba^+$ tagging with lasers in a TPC and the time sequence of signals are illustrated in Fig. 2-3. When a $0\nu\beta\beta$ decay,

$$^{136}Xe \rightarrow {}^{136}Ba^{++} + 2\,e^- + 2.479\ MeV,$$

occurs somewhere in the liquid xenon TPC, the two fast electrons carrying the high decay energy will form a short track of ionization and scintillation within about 2 mm of the decay position. The scintillation photons at the wavelength of 175 nm are detected by the small photomultiplier tubes, and this scintillation serves as the time t=0 marker. The electrons drift following the electric field lines and create a signal on the TPC x-y wires. The location of the electron swarm on the wires provides the x and y coordinates of the $0\nu\beta\beta$ decay event. The z-coordinate is determined from the arrival time of the electron swarm since the electron mobility in liquid xenon is known (~2200 $cm^2/Vs$ near the triple point [66]). A parallel laser beam is directed with a scanner mirror controlled by a

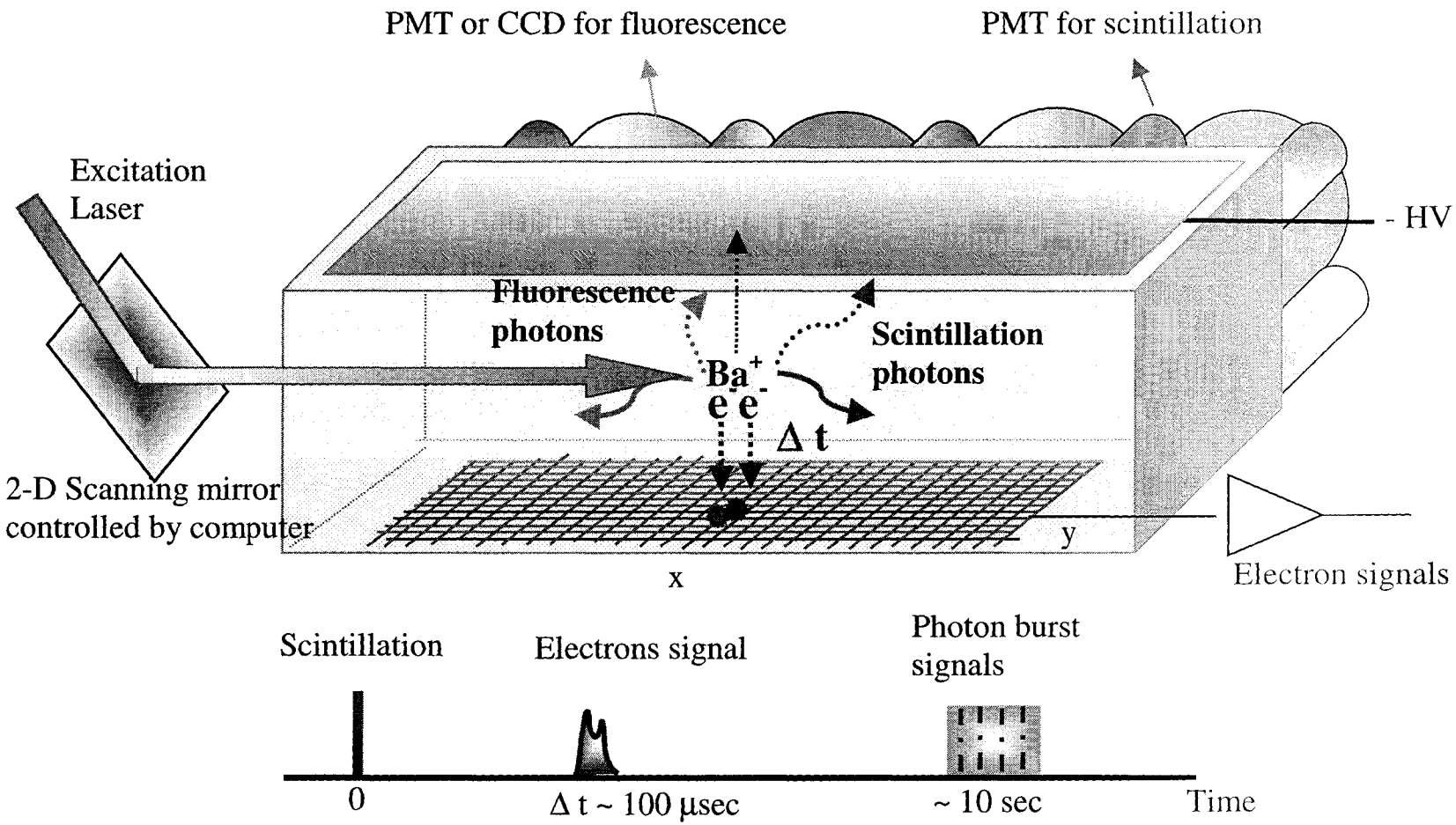


**Figure 2-3 Schematic diagram of a proposed LXe TPC and $Ba^+$ tagging with lasers.**

computer to the calculated decay site. It is expected the $Ba^{++}$ daughter ion will become $Ba^{+}$ quickly in liquid xenon because of the band gap in liquid xenon, i.e. the energy to create an electron-hole pair, is less than the ionization potential of $Ba^{+}$ as shown in Fig. 2-4 [58]. The reaction, $Ba^{++} \rightarrow Ba^{+} + Xe^{h+}$, occurs, where $Xe^{h+}$ is a hole in the xenon band structure. The $Ba^{+}$ will move slowly in the liquid xenon. If the $Ba^{+}$ mobility is known, the computer-controlled mirror can allow the laser beam to follow the $Ba^{+}$ motion, and the fluorescence burst photons from $Ba^{+}$ should be registered and detected by a PMT or a CCD. By modulating the laser position on and off at the calculated $Ba^{+}$ position, one can distinguish a real event from stray light backgrounds. This method should give an unambiguous signature of the presence of the decay daughter ion at the expected position, and a high discrimination against radioactive backgrounds which do not produce a $Ba^{+}$ daughter is obtained. In order to realize this new technique, we need to study the laser spectroscopy and mobility of $Ba^{+}$ in liquid xenon. This is the main focus of this thesis.

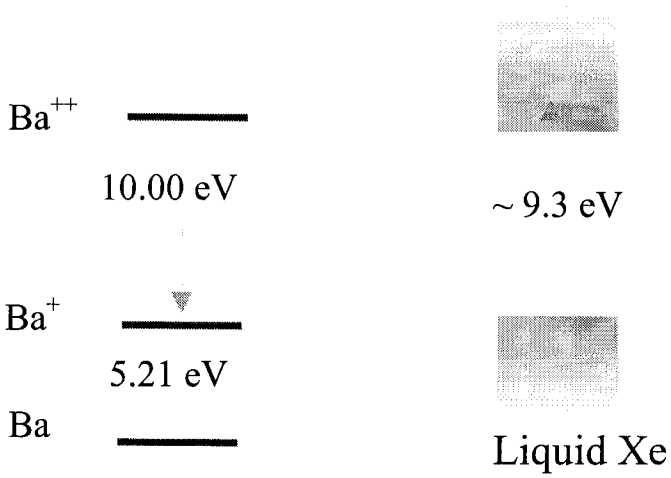


**Figure 2-4 Ionization potential of Ba and band structure of liquid xenon.**

Investigation of this technique was done mostly in collaboration with Miyajima's group at Fukui University in Japan from 1997 to 2002. A 1kg test LXe TPC experiment somewhat like Fig. 2-3 was planned in his laboratory. Achievement of this test experiment now does not show as likely. A later proposal with tons size of enriched $^{136}Xe$, Enriched Xenon Observatory (EXO), was submitted to DOE in 1999 where tagging a single $Ba^{+}$ decay daughter in a high pressure xenon gas was considered [60]. We have joined the EXO collaboration on April 1, 2003. It is anticipated that if our fluorescence tagging method in liquid xenon is shown to work, it will be considered seriously as a tagging method for the EXO experiment.

# References


1. B. Pontecorvo, Zh. Eksp. Teor. Fiz. 33, 549 (1957).
2. M.C. Gonzalez-Garcia and Y. Nir, Rev. Mod. Phys. 75, 345 (2003).
3. The Super-Kamiokande Collaboration, Y. Fukuda et al, Phys. Rev. Lett. 81, 1562 (1998). More publications can be found at http://arxiv.org/find/hepex/1/au:+super_kamiokande/0/1/0/all/0/1
4. The SNO Collaboration, Q.R. Ahmad et al., Phys. Rev. Lett. 89, 011302 (2002). http://www.sno.phy.queensu.ca/sno/publications.html
5. KamLAND Collaboration, K. Eguchi et al., Phys. Rev. Lett. 90, 021802 (2003).
6. B.T. Cleveland et al., Astrophys. J. 496, 505 (1998).
7. SAGE Collaboration, J.N. Abdurashitov et al., Phys. Rev. C 60, 055801 (1999).
8. GNO collaboration, T.A. Kirsten, Nucl. Phys. B (Proc. Suppl.) 118, 33 (2003).
9. R. Becker-Szendy et al., Phys. Rev. D 46, 3720 (1992).
10. K.S. Hirata et al., Phys. Lett. B 280, 146 (1992).
11. W.W.M. Allison et al., Phys. Lett. B 449, 137 (1999).
12. F. Ronga, Nucl. Phys. B (Proc. Suppl.) 87, 135 (2000).
13. C. Athanassopoulos et al., Phys. Rev. Lett. 81, 1774 (1998).
14. C. Athanassopoulos et al., Phys. Rev. C58, 2489 (1998).
15. R. Stefanski, Nucl. Phys. B (Proc. Suppl.) 110, 420 (2002).
16. M.C. Gonzalez-Garcia et al., Phys. Rev. D 63, 033005 (2001).
17. J.F. Wilkerson and R.G.H. Robertson, Current Aspects of Neutrino Physics, Chapter 3, Springer-Verlag, 1st Edition, 2001
18. J. Bonn et al., Nucl. Phys. B (Proc. Suppl.) 110, 395 (2002).
19. K. Assamagan et al., Phys. Rev. D 53, 6065 (1996).
20. I. Nikolic, in *International Workshop on Weak Interactions and Neutrinos*, 214 Elsevier, 1997.
21. C. Weinheimer, Nucl. Phys. B (Proc. Suppl.) 118, 279 (2003).
22. K. Zuber, Phys. Reports 305, 295 (1998).
23. S. Hannestad, Phys. Rev. D 66, 125011 (2002).
24. S.R. Elliott and P. Vogel, Annu. Rev. Nucl. Part. Sci. 52, 115 (2002).

25. A. Balysh et al., Phys. Rev. Lett. 77, 5186 (1996).
26. V.B. Brudanin et al., Phys. Lett. B 495, 63 (2000).
27. H.V. Klapdor-Kleingrothaus et al., Eur. Phys. J. A 12, 147 (2001).
28. F.T. Avignone et al., Phys. Lett. B 256, 559 (1991).
29. C.E. Aalseth et al., Nucl. Phys. B (Proc. Suppl.) 48, 223 (1996).
30. S.R. Elliott et al., Phys. Rev. C 46, 1535 (1992).
31. R. Arnold et al., Nucl. Phys. A 636, 209 (1998).
32. R. Arnold et al., Nucl. Phys. A 658, 299 (1999).
33. A. Kawashima et al., Phys. Rev. C 47, 2452 (1993).
34. M.E. Wieser and J.R. De-Laeter, Phys. Rev. C 64, 024308 (2001).
35. D. Dassie et al., Phys. Rev. D 51, 2090 (1995).
36. H. Ejiri et al., Phys. Lett. B 258, 17 (1991).
37. H. Ejiri et al., J. Phys. G 17, S155 (1991).
38. A. DeSilva et al., Phys. Rev. C 56, 2451 (1997).
39. M. Alston-Garnjost et al, Phys. Rev. C 55, 474 (1997).
40. V.D. Ashitkov et al., JETP Lett. 74, 529 (2001).
41. R. Arnold et al., Z. Phys. C 72, 239 (1996).
42. F.A. Danevich et al., Phys. Rev. C 62, 044501 (2000)
43. H. Ejiri et al., J. Phys. Soc. Jpn. 64, 339 (1995)
44. T. Bernatowicz et al., Phys. Rev. C 47, 806 (1993).
45. M.T.F. da Cruz et al., Phys. Rev. C 48, 3106 (1993).
46. Ju.M. Gavriljuk et al., Phys. Rev. C 61, 035501 (2000).
47. V. Artemiev et al., Phys. Lett. B 345, 564 (1995).
48. A.L. Turkevich et al., Phys. Rev. Lett. 67, 3211 (1991).
49. A. Staudt et al., Europhys. Lett 13, 31 (1990).
50. E. Caurier et al., Phys. Rev. Lett. 77, 1954 (1996).
51. Ke You et al., Phys. Lett. B 265, 53 (1991).
52. C.E. Aalseth et al., Phys. Rev. C 59, 2108 (1999); Nucl. Phys. Russ. Acad. Sci. 63, 1299 (2000); hep-ex/0202026
53. H. Ejiri et al., Phys. Rev. C 63, 065501 (2001).
54. A. Alessandrello et al., Phys. Lett. B 486, 13 (2000).

55. R. Luescher et al., Phys. Lett. B 434, 407 (1998).
56. H.V. Klapdor-Kleingrothaus et al., Mod. Phys. Lett. A 16, 2409 (2001);
see also comments by C.E. Aalseth et al., ibid. 17, 1475 (2002);
reply by H.V. Klapdor-Kleingrothaus, hep-ph/0205228.
57. E. Conti et al., Phys. Rev. B 68, 054201 (2003).
58. M.K. Moe, Phys. Rev. C 44, R931 (1991).
59. M. Miyajima et al., KEK proceedings 91-5, 19 (1991);
M. Miyajima et al., IEEE Trans. Nucl. Sci. 41, 835 (1994).
60. Danilov M et al., Phys. Lett. B 480, 12 (2000).
61. W.M. Fairbank, Jr. et al., J. Opt. Soc. Amer. 65, 199 (1975).
62. G.W. Greenlees et al., Opt. Commun. 23, 236 (1977).
63. G.S. Hurst et al., Appl. Phys. Lett. 30, 229 (1977).
64. V.I. Balykin et al., JETP Lett. 26, 357 (1977).
65. W.Neuhauser et al., Phy. Rev. Lett. 41, 233 (1978).
66. L.S. Miller et al., Phys. Rev. 166, 871 (1968).

# Chapter 3

## Ionic mobility in liquid noble gas

The study of the ionic mobility in dielectric liquids has a history of over 100 years. A simple model of the ion as a sphere moving through a homogeneous fluid is often used to describe the ion transport in liquid. In more detailed models, motion of the impurity ion can be a powerful tool to probe the properties of dielectric liquids on a microscopic scale and the structure of the fluid atoms around the ion.

In this chapter, a brief overview of ionic mobility measurements in liquid helium and xenon is summarized in Section 3-1. The simple Stokes' equation will be introduced and used to model the ionic mobility in a liquid medium in Section 3-2. In this model, it is assumed that the liquid is static during the mobility measurement. However, the momentum transfer from the charge carriers to liquid can cause significant fluid motion if the total charge is large enough, which can cause the apparent mobility to be greater than the true value. In Section 3-3, the effect of fluid motion on mobility measurements will be discussed. Finally, the microstructure of an impurity ion based on a thermodynamic model in liquid xenon will be reviewed in Section 3-4.

### 3-1 Overview of ionic mobility in liquid helium and xenon

A charged impurity in a polarizable liquid is expected to strongly modify the surrounding environment of the liquid. Atkins first presented a model for the solidification of noble gas atoms around a single ion in liquid helium (LHe) due to electrostriction [1]. He predicted that the cluster radius is a function of the ionic charge only. However, mobility measurements in liquid helium have shown the mobility

somewhat depends on the identity of the core ion [2-4]. For the alkali ions, $K^+$, $Rb^+$ and $Cs^+$, the mobility is smaller than that of the $He^+$ ion and slightly decreases as the atomic number increases as shown in Fig. 3-1. On the other hand, the reverse trend was reported for the alkaline earth ions, $Mg^+$, $Ca^+$, $Sr^+$ and $Ba^+$. It is believed that monatomic ions in superfluid helium form two very different structures. Electrons and single-charged alkaline earth ions, except $Be^+$, form a "bubble" in the liquid, while $Be^+$, $He^+$, and alkali ions are thought to have a "snowball" structure of solid helium surrounding the ion as shown in Fig. 3-2. The bubble structure is produced by dominance of the repulsive Pauli force between the outer electron of the ion and the surrounding helium atoms, and the snowball is caused by dominance of the charge-induced dipole interaction, electrostriction, between the positive ion and the helium matrix [5,6].

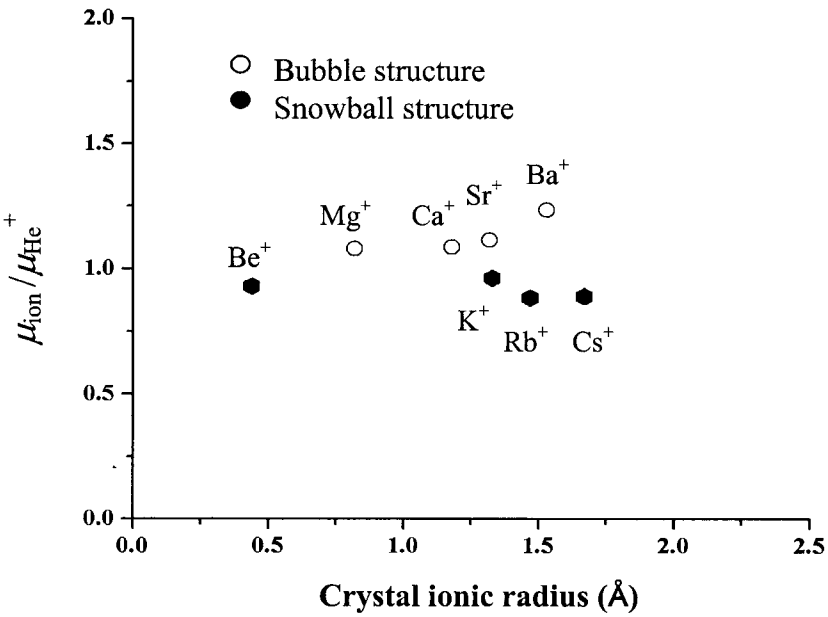


**Figure 3-1 Ionic mobility as a function of ion core in superfluid helium.**

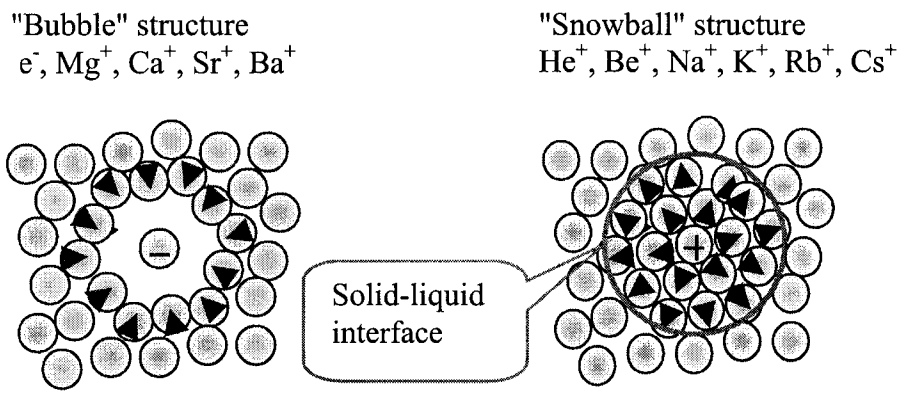


**Figure 3-2 Visualization of snowball and bubble structures of ions in liquid helium.**

Although ionic mobility has been investigated extensively in liquid helium, experimental results and theoretical predictions are scarce for the structure and mobility of monatomic ions in the other noble gas liquids. Hilt *et al.* have studied the mobility of $Xe_h^+$ (actually electron holes in the liquid xenon band structure rather than $Xe^+$ ions), tetramethylsilane ions ($TMSi^+$), n-pentane ions (n-$pentane^+$), sulfur hexafluoride ions ($SF_6^-$) and molecular oxygen ions ($O_2^-$) in liquid xenon in a temperature range from 161K to 280K. The results are shown in Fig. 3-3 [7-10]. The $Xe_h^+$ mobility at 170 K is 0.0035 $cm^2V^{-1}s^{-1}$, which is an order of magnitude faster than the other ions, is not shown here. Based on their results, they claimed that the ions studied in earlier experiments by the other groups were probably some unknown impurity ions. Thus the data of Hilt *et al.* were the first reliable ionic mobility measurements in a liquid noble gas other than helium. Recently, using a radioactive source, the mobilities of the monatomic ions, $Tl^+$ and $Th^+$, in liquid xenon were measured at a single temperature, as shown also in Fig. 3-3 [11,12]. In this thesis, measurements of the mobility of the alkaline earth ions, $Mg^+$, $Ca^+$, $Sr^+$ and $Ba^+$, in liquid xenon are reported for the first time.

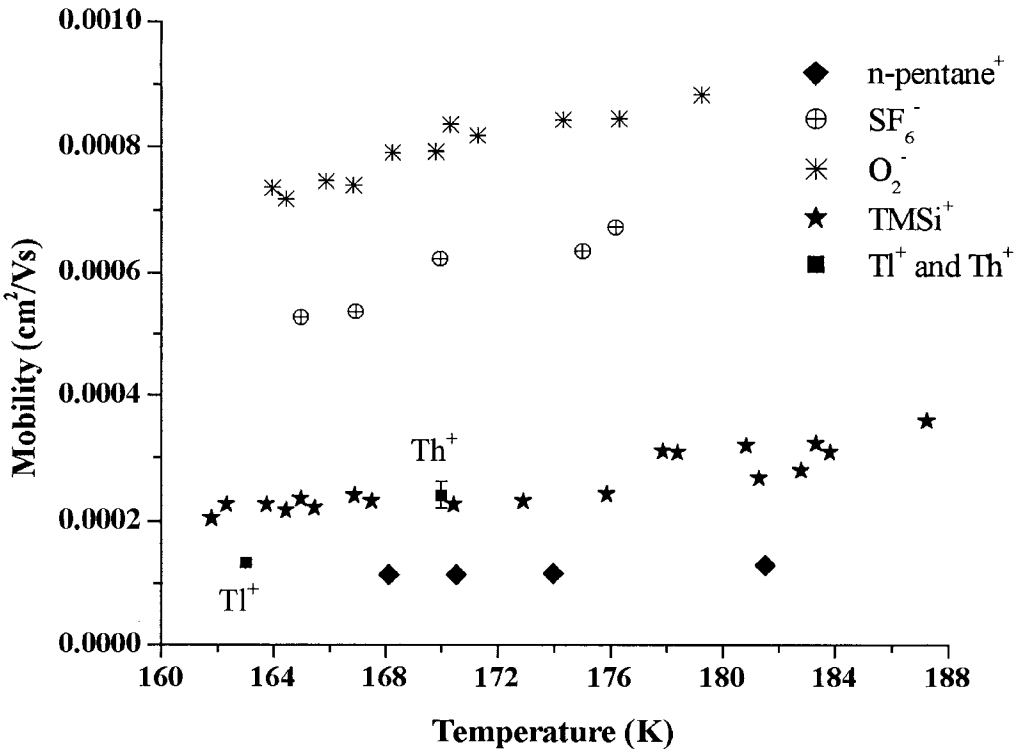


**Figure 3-3 Mobility of $TMSi^+$, n-pentane$^+$, $SF_6^-$, $O_2^-$, $Tl^+$ and $Th^+$ as a function of temperature.**

Hilt *et al.* interpreted the mobility of positive ions in terms of a "snowball" model, i.e., the formation of layers of solid xenon around the ion due to the electrostriction effect [8]. In contrast, a "bubble" model was proposed for the negative ions in liquid xenon due to the strong exchange interaction of the weakly bound valence electron of $O_2^-$ and $SF_6^-$ with the outer electrons of the Xe neighbors [9].

## 3-2 Ion transport in liquid

In a simple model, an individual ion drifts at constant velocity v under constant electric field $E$ because the electric force balances the frictional force of the approximately static fluid on the ion. Ion is treated as a solid sphere of radius $R$ and the

frictional force is described by Stokes' equation, $f=6\pi\eta R$v, where $\eta$ is the viscosity of liquid. Hence, the mobility $\mu$ of the ion is given as

$$\mu = \frac{\mathrm{v}}{E} = \frac{q}{6\pi\eta R}. \qquad 3\text{-}1$$

This can be rewritten as

$$\mu(T)\eta(T) = \frac{q}{6\pi R} = \text{constant}, \qquad 3\text{-}2$$

which is known as Walden's rule, and it is expected to be true if $R$ is independent of temperature $T$. For mobility measurements of molecular ions in some liquids, Walden's rule is known to be approximately correct [13,14]. For constant $E$, the mobility is related to the applied voltage $V$, the drift distance $d$ and the drift time $t_d$ by

$$\mu = \frac{\mathrm{d}/\mathrm{t_d}}{\mathrm{V}/\mathrm{d}} = \frac{\mathrm{d}^2}{\mathrm{V t_d}} \qquad 3\text{-}3$$

## 3-3 Fluid motion

It was assumed in Eq. 3-1 that the liquid xenon is static. However, the momentum transferring from the charge carriers to the liquid through the frictional force can cause significant fluid motion when ion cloud charge is great enough. This can cause the measured mobility to be greater than the true value. Studies of charge-induced fluid motion date back to 1960s [15,16]. The earlier work has shown that the fluid motion depends on the electrode geometry, drift distance and charge. Experimentally, we found that this effect has to be taken into account even the total ion charge in a pulse is as small as a few pC.

The basic equation linking the apparent mobility to the true mobility and liquid speed $\mathrm{v_{liquid}}$ is

$$v_{apparent} = \mu_{true} E + v_{liquid} . \qquad 3\text{-}4$$

Introducing the apparent mobility $\mu_{appa.} = v_{appa.} / E$, yields

$$\mu_{appa.} = \mu_{true} + \frac{v_{liquid}}{E} . \qquad 3\text{-}5$$

An upper limit for $v_{liquid}$ can be obtained from energy conservation [10]. The increase in kinetic energy of a liquid with mass density $\rho$ in a volume $\frac{4}{3}\pi r^3$ is equal to a change in electrostatic potential energy of the charge $Q$ over a distance $d$,

$$\frac{1}{2}(\frac{4}{3}\pi r^3 \rho) v_{liquid}^2 = QEd , \qquad 3\text{-}6$$

since the charges themselves move at constant velocity and do not change kinetic energy. Thus

$$\frac{v_{liquid}}{E} = \sqrt{\frac{3Qd}{2\pi r^3 E\rho}} , \qquad 3\text{-}7$$

where $r$ is the radius of the volume of fluid moving with the charge $Q$.

By combining equation 3-5 and 3-7,

$$\mu_{appa.} = \mu_{true} + c\sqrt{Q} , \qquad 3\text{-}8$$

where $c$ is a constant. Thus, Eq. 3-8 can be used as a guide for the dependence of the apparent mobility on $Q$.

If the dependence of Eq. 3-8 is verified experimentally, the true mobility can be determined by extrapolating to zero $\sqrt{Q}$ with an experimentally determined constant $c$. It is also useful to note in Eq. 3-7 that the effect of fluid motion may be reduced by larger external electric field $E$ and smaller drift distance $d$. However, Eq. 3-8 is a gross oversimplification of the problem. First of all, when the ions are created in the gas phase

by laser ablation and are drawn into the liquid surface by electric field, the longitudinal dimension of the ion cloud will squeeze at the gas-liquid interface because of the three orders of magnitude difference in ion mobility between the gas and liquid phases. It is expected that the ion cloud is disk-like at the beginning of its journey in liquid xenon and becomes more spherical thereafter. Thus, the charge density is not uniform in the drift path. Secondly, due to the electric force on the charges, the ions always tend to move ahead of the liquid. In addition to the applied field, there is an internal field of the ion cloud, which is proportional to $Q$. The force on the ions and the fluid from the internal field does not average to zero because of the asymmetry of the liquid-gas interface. Thus another possible relationship is

$$\mu_{appa.} = \mu_{true} + cQ. \qquad 3\text{-}9$$

In addition, the charge-induced fluid motion might fall nearly into the turbulent regime in some measurements.

Due to the roughness of the above simple energy conservation fluid motion model, the predicted $\sqrt{Q}$ dependence of the fluid motion correction might be not accurate. Experimentally, a power between $Q$ and $\sqrt{Q}$ is found, which depends somewhat on $E$.

There may also exist some residual liquid flow even there is no charge-induced liquid motion. The residual flow might arise either from a small temperature gradient or from ablated particles moving through the liquid. Ignoring the Q-dependence for now, it can be seen from Eq. 3-4,

$$\mathrm{v} = \mu E + \mathrm{v}_{residual}, \qquad 3\text{-}10$$

that the mobility, in that case, is the slope of v vs. $E$. This formula has been used in some previous experimental work in liquid helium where a residual liquid flow was observed

[3]. A phenomenological equation combining equation 3-8, 3-9 and 3-10 is then obtained to determine the true mobility,

$$v = v_{residual}(0) + \frac{dv_{residual}}{dQ^n}Q^n + (\mu_{true} + \frac{d\mu}{dQ^n}Q^n)E \equiv a_0 + a_1Q^n + (b_0 + b_1Q^n)E, \qquad 3\text{-}11$$

where v is the drift velocity, $a_0+a_1Q^n$ is the term of residual fluid flow and $(b_0+b_1Q^n)E$ is the term of charged induced fluid motion. Experimentally as will be discussed in Chapter 6, powers of n=1/2, n=1 and n as a function of $E$ are used to find the best fit to experimental data sets in Chapter 6.

## 3-4 Ion structure in liquid xenon

According to Akins's model, electrostriction will increase the pressure and density of the liquid in the vicinity of the ion, and the increased pressure might exceed the melting pressure, especially when the temperature is close to the triple point. Therefore, one or more layers of xenon atoms around the ion will solidify, and a cluster or snowball structure is formed. Based on this model, the cluster radius ($R_s$) as a function of temperature can be estimated by the thermodynamic considerations of the chemical potential $\mu_c$ $(T, P, E)$ of the liquid at a distance $r$ from the point charge with the electric field $E(r)=q^2/4\pi\varepsilon_0\kappa r^2$. It is given as [1]

$$\mu_c = u - Ts + P\mathcal{V} - E\mathcal{P}, \qquad 3\text{-}12$$

where $\mathcal{P}$ is the polarization per mole and $\mathcal{V}$ is the molar volume. The first and second laws of thermodynamics give the equation

$$Tds = du + Pd\mathcal{V} - Ed\mathcal{P}. \qquad 3\text{-}13$$

By differentiating Eq. 3-12 and using Eq. 3-13,

$$d\mu_c = -sdT + \mathcal{V}dP - \mathcal{P}dE. \qquad 3\text{-}14$$

In equilibrium, $d\mu_c = 0$ (i.e., the Gibbs function $G$ is minimized), and $dT=0$,

$$\mathcal{V}dP = \not{\mu}dE. \qquad 3\text{-}15$$

For a linear dielectric material,

$$\not{\mu} = \mathcal{V}\varepsilon_0(\kappa\text{-}1)E, \qquad 3\text{-}16$$

where $\kappa$ is the dielectric constant.

By combining Eq. 3-15 and Eq. 3-16, and assuming molar volume $\mathcal{V}$ is independent of pressure, the excess pressure $P(r)$ at a distance $r$ from the ion over the saturation pressure of liquid $P_s$ (liquid-gas interface) at r=∞ where E=0 is given as

$$\int_{P_s}^{P} dP = \int_0^E \varepsilon_0(\kappa-1)EdE = \frac{\varepsilon_0(\kappa-1)}{2}E^2 = \frac{(\kappa-1)}{\kappa^2}\frac{q^2}{32\pi^2\varepsilon_0 r^4}. \qquad 3\text{-}17$$

$$P - P_s = \frac{(\kappa-1)}{\kappa^2}\frac{q^2}{32\pi^2\varepsilon_0 r^4}. \qquad 3\text{-}18$$

At some distance $R_s$ near the ion, the pressure $P(R_s)$ might be high enough to reach the melting pressure $P_m$, and a solid cluster of xenon around the ion would be formed spontaneously whose radius $R_s$ will go to infinity as $P_s$ approaches $P_m$ at the triple point. Due to the existence of a solid-liquid surface tension $\sigma_{sl}$ at the interface between the solid cluster and the liquid xenon, $R_s$ does not go to infinity in reality at the triple point. The pressure difference between the phases is $2\sigma_{sl}/R_s$, where $\sigma_{sl}$ is the surface tension along the solid-liquid interface rather than the commonly measured surface tension, $\sigma_{lg}$, determined experimentally along the liquid-gas interface. Because the chemical potential is constant across the interface, at the ion cluster radius $R_s$,

$$\mu_{cs}(P+2\sigma_{sl}/R_s) = \mu_{cl}(P), \qquad 3\text{-}19$$

and

$$\mu_{cs}(P_m) = \mu_{cl}(P_m). \qquad 3\text{-}20$$

By subtracting Eq. 3-20 and Eq. 3-19, and using $(\partial\mu_c/\partial P)_T = \mathcal{V}$

$$P_m - P = -\frac{\mathcal{V}_s}{\mathcal{V}_l - \mathcal{V}_s}\frac{2\sigma_{sl}}{R_s}, \qquad 3\text{-}21$$

where incompressibility of both liquid and solid is assumed. By combining Eq. 3-18 and Eq. 3-21,

$$P_m - P_s = \frac{(\kappa-1)}{\kappa^2}\frac{q^2}{32\pi^2\varepsilon_0 R_s^{\,4}} - \frac{\mathcal{V}_s}{\mathcal{V}_l - \mathcal{V}_s}\frac{2\sigma_{sl}}{R_s}. \qquad 3\text{-}22$$

The radius $R_s$ can then be determined by solving the Eq. 3-22. The surface tension $\sigma_{sl}(T)$, measured along the solid-liquid interface, is not available, so Hilt *et al.* suggested a formula derived by Bachinsky, given as [17,18]

$$\sigma_{sl} \cong \sigma_{\lg}\left(\frac{n_s - n_l}{n_l}\right)^4 \qquad 3\text{-}23$$

Electrostriction may have another effect on ionic mobility. It also leads to an increase of the liquid density around the ionic cluster, which in turn causes an increase of the viscosity near the ion. Hilt *et al.* suggested that one should use the viscosity along the melting line, $\eta_m$, to include this effect in Eq. 3-1 [8]. The viscosity of xenon has been measured only along the liquid-gas interface (saturation line) $\eta_s$, and the viscosity $\eta_m$ along the melting line is not available. The principle of corresponding states allows the transport of known properties for one noble gas species to another. Therefore, the $\eta_m^{Xe}$ of xenon can be determined by the measured $\eta_m^{Ar}$ of argon by [8]

$$\eta_m^{Xe}(T) = \frac{\eta_c^{Xe}}{\eta_c^{Ar}}\eta_m^{Ar}\left(\frac{T_c^{Xe}}{T_c^{Ar}}T\right), \qquad 3\text{-}24$$

where $\eta_c$ and $T_c$ are the viscosity and temperature at the critical point, respectively. $\eta_m^{Xe}$ can also be found in NIST Chemistry Webbook [19].

Rather than modifying the viscosity from $\eta_s$ to $\eta_m$, Ostermeier and Schwartz applied the Navier-Stokes equations to treat the hydrodynamic problem with density and viscosity varying with the radial distance from the ion cluster [20]. The result is that the drag force is changed from $6\pi\eta R\mathrm{v}$ to $(6\pi\eta R\mathrm{v})F$. $F$ is a dimensionless factor which depends on the dimensionless density $\rho(r/R)\rho_s^{-1}$ and viscosity $\eta(r/R)\eta_s^{-1}$ variations due to electrostriction. Here, $\rho_s$ and $\eta_s$ are the values in the fluid far from the ion. Therefore, the mobility of Eq. 3-1 becomes

$$\mu = \frac{\mathrm{v}}{E} = \frac{q}{6\pi\eta RF}. \qquad 3\text{-}25$$

Ostermeier and Schwartz solved the complicated Navier-Stokes differential equations with numerical solutions. Based on their model, the measured ion mobility in normal liquid helium was fit quite well by theory in the temperature range from 2.17 K to 4.2K [20].

By solving the Eq. 3-22, the theoretical cluster radius as a function of temperature can be determined, where $\kappa$=1.94 [21] and $n_s$=3.4 g/cm$^3$ [22] are assumed to be constant. The calculated $R_s$, $F$ and other parameters are summarized in Table 3-1 at various temperatures. The model predicts a rapidly increasing solid radius near the triple point as shown in Fig. 3-4, which leads to a rapid decrease in mobility, according to Eq. 3-1 or Eq. 3-25. The predictions for the mobility using the viscosity $\eta_s$ along the liquid-gas interface line ($\mu_s$) and $\eta_m$ along the solid-liquid interface line ($\mu_m$) by Eq. 3-1, and the mobility using Eq. 3-25 with a modified drag force ($\mu_F$), taking $F$ values from the solutions of

Ostermeier and Schwartz, are all given in Table 3-1 and plotted in Fig. 3-5. A rapid decrease in mobility is observed in all three cases near the triple point, but there is a difference in mobility slope at higher temperature in these three cases. These predictions will be compared with experimental results in Chapter 6.

**Table 3-1 Parameters, and theoretical predictions for cluster radius and mobility at various temperatures.**

| $T$ (K) | $P_m$[a] (atm) | $P_s$[b] (atm) | $\sigma_{lg}$[b] (N/m) | $\eta_s$[b] (Ns/m$^2$) | $n_l$[b] (g/cm$^3$) | $\mathscr{V}_l$[b] (m$^3$/mole) | $\eta_m$[c] (Ns/m$^2$) | $\sigma_{sl}$[d] (N/m) | $F$[e] | $R_s$ (nm) | $\mu_s$ (cm$^2$/Vs) | $\mu_m$ (cm$^2$/Vs) | $\mu_F$ (cm$^2$/Vs) |
|---|---|---|---|---|---|---|---|---|---|---|---|---|---|
| 161.4 | 0.8 | 0.81 | 0.019 | 5.13E-04 | 2.96 | 4.43E-05 | 5.58E-04 | 9.13E-06 | 1 | 2.61E-09 | 6.34E-05 | 5.82E-05 | 6.34E-05 |
| 162.4 | 24.1 | 0.86 | 0.019 | 5.06E-04 | 2.96 | 4.44E-05 | 5.61E-04 | 9.77E-06 | 1 | 9.82E-10 | 1.71E-04 | 1.54E-04 | 1.71E-04 |
| 163.4 | 49.6 | 0.91 | 0.019 | 4.99E-04 | 2.95 | 4.45E-05 | 5.64E-04 | 1.03E-05 | 1.01 | 8.20E-10 | 2.08E-04 | 1.83E-04 | 2.06E-04 |
| 165.4 | 100.9 | 1.02 | 0.018 | 4.85E-04 | 2.94 | 4.47E-05 | 5.70E-04 | 1.14E-05 | 1.01 | 6.87E-10 | 2.55E-04 | 2.17E-04 | 2.52E-04 |
| 169.4 | 204.5 | 1.27 | 0.018 | 4.59E-04 | 2.91 | 4.51E-05 | 5.81E-04 | 1.43E-05 | 1.03 | 5.77E-10 | 3.21E-04 | 2.53E-04 | 3.11E-04 |
| 173.4 | 309.6 | 1.57 | 0.017 | 4.35E-04 | 2.88 | 4.56E-05 | 5.93E-04 | 1.76E-05 | 1.04 | 5.20E-10 | 3.75E-04 | 2.75E-04 | 3.61E-04 |
| 177.4 | 416.2 | 1.92 | 0.016 | 4.12E-04 | 2.86 | 4.60E-05 | 6.04E-04 | 2.15E-05 | 1.06 | 4.83E-10 | 4.26E-04 | 2.91E-04 | 4.02E-04 |
| 181.4 | 524.1 | 2.33 | 0.015 | 3.91E-04 | 2.83 | 4.64E-05 | 6.16E-04 | 2.58E-05 | 1.07 | 4.56E-10 | 4.76E-04 | 3.02E-04 | 4.45E-04 |
| 185.4 | 633.5 | 2.8 | 0.015 | 3.71E-04 | 2.80 | 4.69E-05 | 6.27E-04 | 3.10E-05 | 1.09 | 4.35E-10 | 5.25E-04 | 3.11E-04 | 4.82E-04 |
| 190.4 | 772.1 | 3.48 | 0.014 | 3.48E-04 | 2.76 | 4.75E-05 | 6.41E-04 | 3.87E-05 | 1.12 | 4.14E-10 | 5.89E-04 | 3.20E-04 | 5.26E-04 |

a: reference [23].
b: reference [19].
c: reference [19].
d: derived by Eq. 3-23.
e: from the graphs in reference [20].

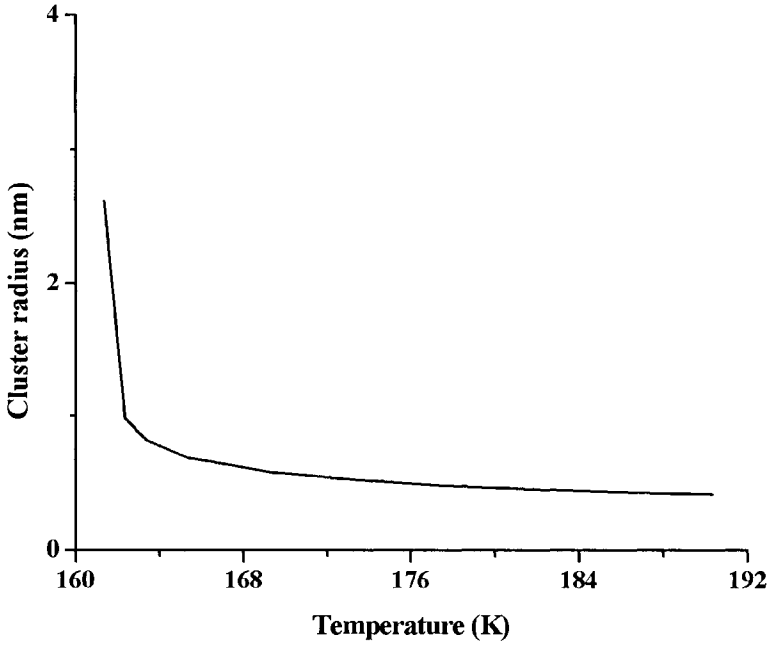


**Figure 3-4 The radius of the ionic cluster as a function of temperature predicted by Akins's model.**

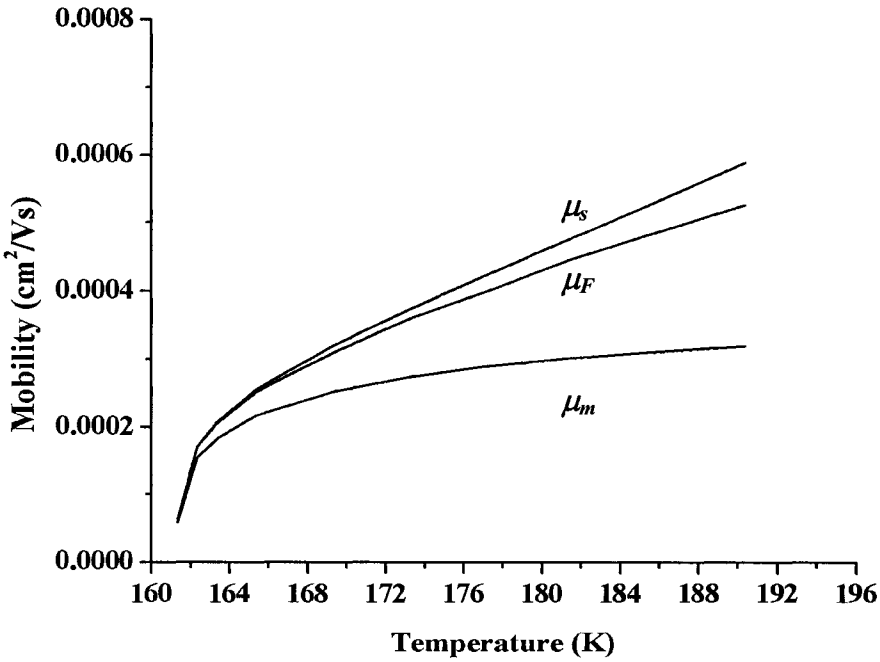


**Figure 3-5 Theoretical predictions for mobility as a function of temperature. $\mu_s$ is the mobility with $\eta_s$ along liquid-gas interface, $\mu_F$ is the mobility with $F\eta_s$ along liquid-gas interface, and $\mu_m$ is the mobility with $\eta_m$ along liquid-solid interface.**

# References


1. K.R. Atkins, Phys. Rev. 116, 1339 (1959).
2. W.I. Glaberson and W.W. Jonson, J. Low Temp. Phys. 20, 313 (1975).
3. H. Gunther, M. Foerste, M. Kunze, G. zu Putlitz and U. von Stein, Z. Phys. B. 101, 613 (1996).
4. M. Foerste, H. Guenther, O. Riediger, J. Wiebe, G. zu Putlitz, J. Low Temp. Phys. 110, 231 (1998).
5. M.W. Cole and R.A. Bachman, Phys. Rev. B. 15, 1388 (1977).
6. M. Buzzacchi, D.E. Galli, and L. Reatto, Phys. Rev. B. 64, 094512 (2001).
7. O. Hilt and W.F. Schmidt, Chem. Phys. 183, 147 (1994).
8. O. Hilt, W.F. Schmidt and A.G. Khrapak, IEEE Trans. Electr. Ins. 1, 648 (1994).
9. A.G. Khrapak and K.F. Volykhin, JETP 88, 320 (1999).
10. W.F. Schmidt, Liquid state electronics of insulating liquids, CRC press, 1997.
11. A.J. Walters and L.W. Mitchell, J. Phys. D. 36, 1323 (2003).
12. K. Wamba, C. Hall and P. C. Rowson, SLAC, private communication.
13. I. Adamczewski, Ionization, conductivity and breakdown in dielectric liquid, Taylor&Francis, London, 1969.
14. O. Gzowski, Nature 194, 173 (1962).
15. E. Gary and T.J. Lewis, J. Phys. D. 2, 93 (1969).
16. V. Essex and P.E. Secker, J. Phys. D. 2, 1107 (1969).
17. J.O. Hirschfelder et al., Molecular Theory of Gases and liquids, John Wiley&Sons, New York, 1964
18. A.G. Khrapak et al., IEEE Trans. Electr. Ins. 26, 582 (1991).
19. E.W. Lemmon et al., "Thermophysical Properties of Fluid Systems" in NIST Chemistry WebBook. http://webbook.nist.govchemistry/fluid/.
20. R.M. Ostermeier and K.W. Schwarz, Phys. Rev. A 5, 2510 (1972).
21. C.A. Whitehead et al., Phys. Rev. B 47, 4979 (1993).
22. B.F. Figgins and B.L. Smith, Philos. Mag. 5, 186 (1960).
23. A.Michels and C. Prins, Physica 28, 101 (1962).
    log [P(atm)+2576]=1.589logT-0.09782 is used to derive the $P_m(T)$.

# Chapter 4

## Optical spectra of impurities in liquid and solid noble gas matrix

The energy levels of a $Ba^+$ ion are well known in vacuum. However, the optical spectra become more complicated once the $Ba^+$ is in an environment with close interaction with other atoms, for example noble gas atoms. Optical spectra of $Ba^+$ in liquid xenon have not been studied prior to this work, and the most intensive previous investigations of optical spectra of impurities in condensed noble gases are conducted in superfluid helium [1], and heavier noble–gas complexes, clusters and solid matrices [2]. In liquid helium, the absorption and emission spectra of impurities show modestly broadened bands with small shift. In contrast, much wider absorption and red-shifted emission bands are common in the solid matrix.

In this chapter, the known properties of the optical spectra of impurities in liquid helium and solid noble gas matrices will be reviewed briefly. On the basis of these results, an educated guess for the $Ba^+$ spectra in liquid xenon is made in order to guide the initial experiments. In Section 4-1, the interaction between the impurity metal atoms (M) and noble gas atoms (also called rare gas atoms, Rg) is briefly discussed to understand qualitatively the change of the optical spectra in the condensed phase. An overview of previous data of impurities in liquid helium and in other solid noble gas matrices is given in Section 4-2. Section 4-3 describes our educated guess for the $Ba^+$ spectra in liquid xenon, and the efficiency of single $Ba^+$ ion detection in liquid xenon is estimated.

## 4-1 Overview of M-Rg interaction

The simplest system with a M-Rg interaction is the diatomic M-Rg molecule, which might also represent the analogous environment of an M atom symmetrically surrounded by Rg atoms except for one vacancy. For M atom with a $(ns)^1$ or $(ns)^2$ spherically symmetric vacuum wavefunction, the interaction *V(R)* with a Rg atom is isotropic and is dominated at large separation R by the dispersion force (van der Waals force or London Force), given roughly as [2]

$$V(R) = \frac{\alpha_M \alpha_{Rg}}{R^6} \frac{I_M I_{Rg}}{I_M + I_{Rg}}, \qquad 4\text{-}1$$

where $\alpha$ is the polarizability and $I$ is the ionization energy of the species. The ionization potential and polarizability of some species are summarized in Table 4-1, which might be useful for our discussions [3,4]. The M-Rg interaction is more complicated when the M atom is excited to the $(np)^1$ or $(ns)^1(np)^1$ state. The potential is no longer isotropic: attractive when the npπ electron wavefunction lobe is perpendicular to the M-Rg axis (bond Π molecular state) and repulsive when npσ electron wavefunction lobe is along M-Rg axis (repulsive $\Sigma^+$ molecular state). Thus the molecular energy curve vs. R and the equilibrium separation $R_{eq}$ for both ground and excited states are different. Schematic curves are shown in Fig. 4-1.

**Table 4-1 Ionization potential and dipole polarizability of various species.**

| species | He | Ne | Ar | Kr | Xe | Na | Ba | Ag | Au |
|---|---|---|---|---|---|---|---|---|---|
| $\alpha$ ($A^3$) | 0.205 | 0.396 | 1.64 | 2.48 | 4.04 | 23.6 | 39.7 | 7.88 | 6.14 |
| I (eV) | 24.59 | 21.56 | 15.6 | 14.0 | 12.13 | 5.14 | 5.21 | 7.58 | 9.23 |

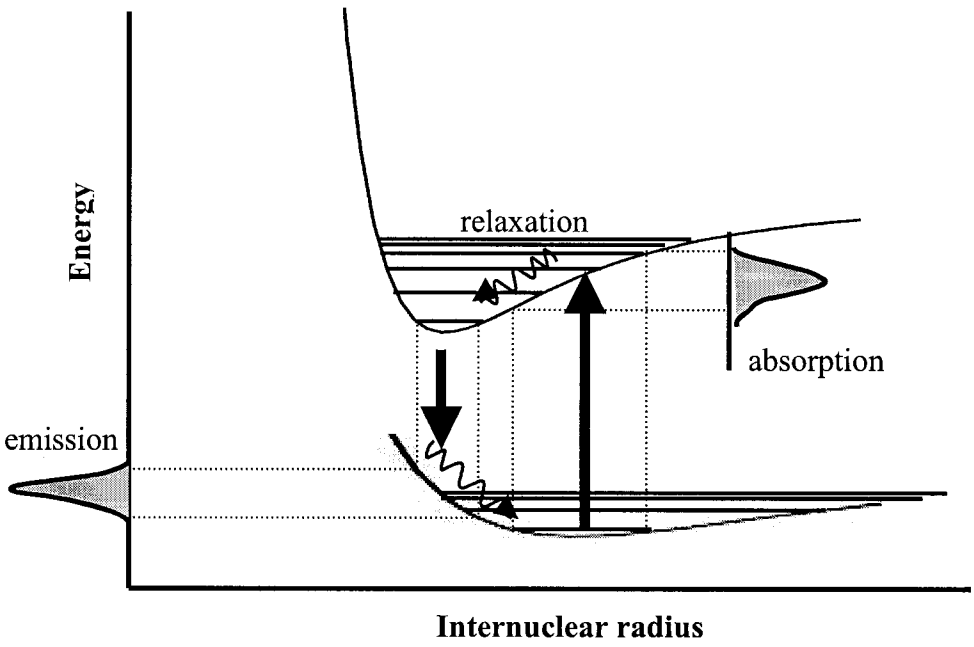


**Figure 4-1. Schematic energy diagram for the ground and the first excited state of an atom with interaction to a Rg atom. A red-shifted emission is occurred due to the Franck-Condon principle.**

According to the Frank-Condon principle, the absorption of a photon involves only a change in the movement of the electrons and not the much heavier nuclei during instantaneous absorption process. The peak absorption then occurs centered on the ground state minimum to high vibrational excited state. The heavier nuclei readjust themselves after the absorption resulting in vibration. A red-shifted emission is then expected after the vibrational energy dissipates and the system drops to the minimum of the upper state curve as shown in Fig. 4-1. Asymmetric absorption and emission bands are also possible in this model. A more detailed model should consider splitting of the upper state due to the spin-orbit coupling (L-S), especially when the L-S interaction is comparable to or bigger than the M-Rg interaction.

The potential curves of an Ag-Ar complex deduced from the experimental data [5] are shown in Fig. 4-2. The crossing between the $^2D_{5/2}$ and $^2P_{3/2}$ states is observed. In the region of these crossings, a mixing of the $^2D$ and the $^2P$ atomic states can occur if the environment is not symmetric, in which even the parity symmetry of the states could be broken. Crossings, particularly near the minimum of the potential curves, can also lead to rapid non-radiative decays.

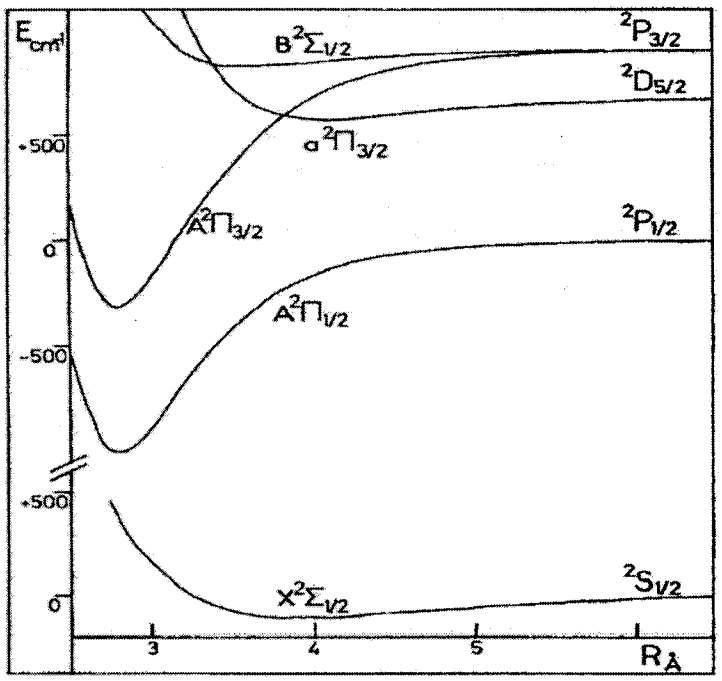


**Figure 4-2 Potential curves of an Ag-Ar complex deduced from the experimental data [5].**

If the impurity is a charged ion $M^+$ rather than a neutral atom M, then there is a big difference in the bonding energy. In the case of $M^+$-Rg complex, the dominant term in $M^+$-Rg interaction is now from the ion-induced dipole force between the $Mg^+$ and Rg atoms, and the interaction energy is given by

$$V(R) = \frac{\alpha q^2}{4\pi\varepsilon_0 R^4}, \qquad 4\text{-}2$$

where $\alpha$ is the polarizability of noble gas atom. The binding is much stronger, especially in the ground state, leading to more similar potential curves in the two states, as shown in Fig. 4-3. It is possible that this might lead to narrower absorption and emission bands with smaller shifts in impurity ions compared to impurity atoms. If the energy difference $\Delta E=E(M\text{-}G^{+})-E(M^{+}\text{-}G)$ is small, less than 1 eV for example, charge transfer is also possible [2].

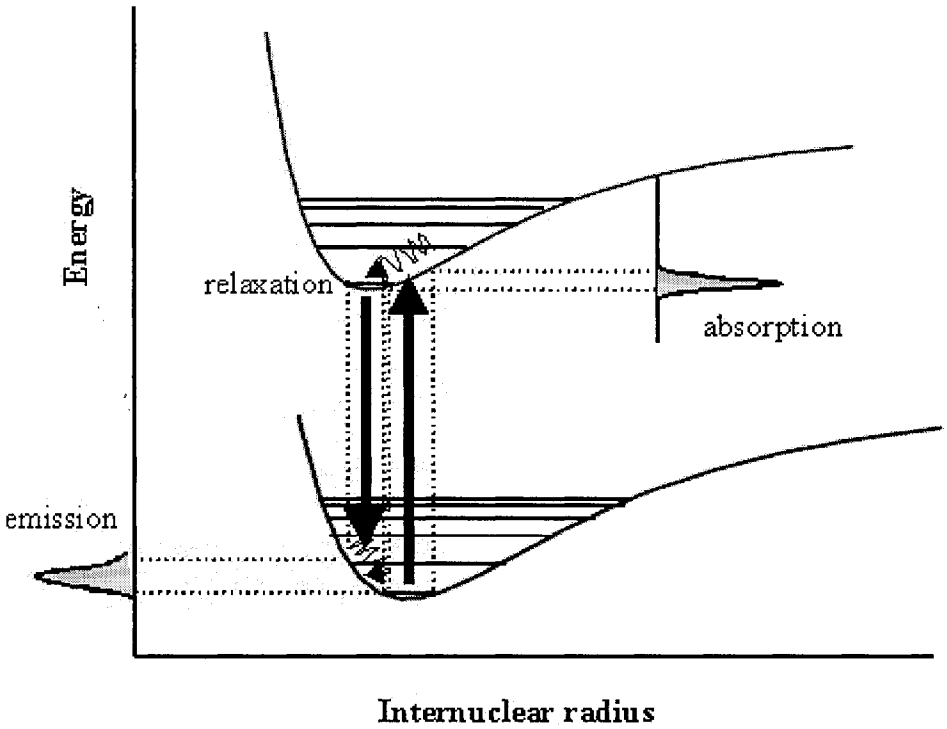


**Figure 4-3 Schematic energy diagram for the ground and the first excited state of an ion with interaction to Rg atoms. A stronger binding is expected for the ground state.**

In a solid matrix, one M atom may replace a single Rg atom and form a one-atom substitution site with conservation of the site symmetry if the van der Waals radius of the M atom is close to the van der Waals radius of the noble gas host. Since the solid noble

gases form a fcc structure, the M atom is surrounded by 12 equivalent nearest neighbors Rg atoms with $O_h$ symmetry. In such environment, an M atom interacts with more than one Rg atom, and results in a large difference of the equilibrium configurations between its ground and excited states. The spectral properties can be understood in terms of the Jahn-Teller effect [6]: every nonlinear molecular or crystal system that has orbital electronic degeneracy when the nuclei are in a symmetrical configuration is unstable with respect to at least one asymmetric distortion of the nuclei which lifts the degeneracy. Therefore, for an impurity in solid matrix, the wavefunction of the nondegenerate ground S state remains centered in the potential of the 12 nearest host neighbors. However, the three-fold orbital degeneracy of the excited P state is spontaneous broken, and the minimum of the potential curve is spatially displaced from the center of symmetry, as shown in Fig. 4-4. The peak absorption occurs centered on the ground state minimum to high vibrational excited states according to the Franck-Condon principle. After rapid vibrational relaxation to the lowest vibrational excited states, the predominant emission occurs off the origin to high vibrational states of the ground state. Thus there is a red-shifted emission relative to the absorption. A more complete picture of the Jahn-Teller effect for the P state is that the P state will split into two bonding $\Pi$ states and one repulsive $\Sigma$ state similar to the Fig. 4-2. It has been suggested that the structure of simple impurity atoms (group I, IA, II and IIA) in a solid matrix is one-atom substitution, which preserves $O_h$ symmetry. In such a highly symmetric structure, it is expected that J is still a good quantum number and the orbital angular momentum is not totally quenched. Therefore the selection rules of $\Delta J=0, \pm 1$ and $\Delta L=\pm 1$ are still valid for absorption. However, if the emission occurs from a configuration of lower symmetry, some vacuum

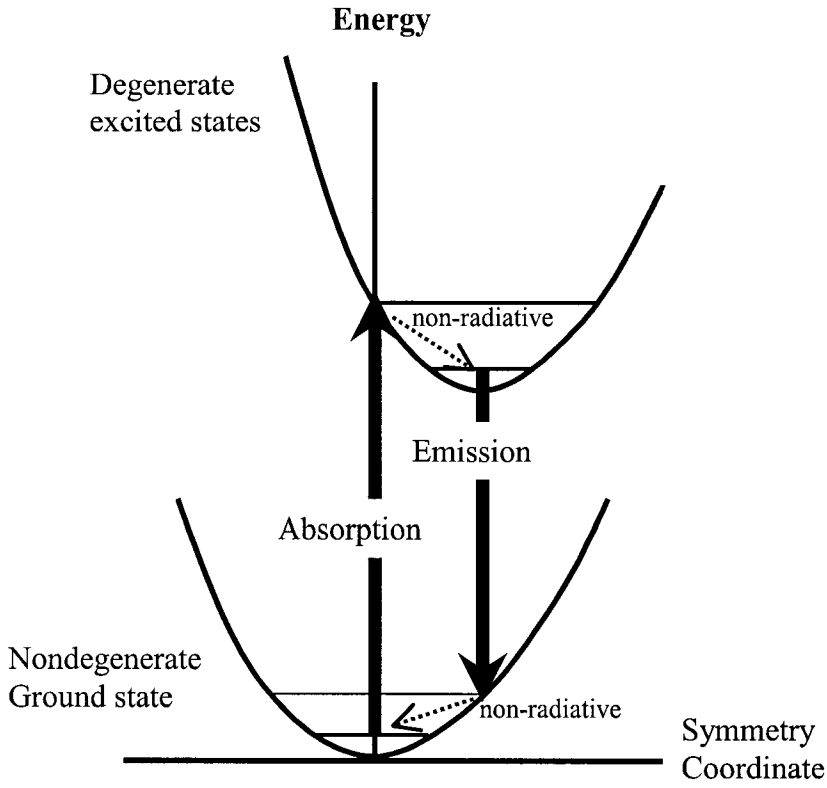


**Figure 4-4. Absorption and emission spectra in solid matrix due to the Jahn-Teller effect.**

atomic selection rules may be broken [2].

In conclusion, the existence of the neighboring Rg atoms around an M atom or ion causes symmetry breaking, mixing and degeneracy lifting of the electronic states. Experimental consequences are that some radiative transitions are missing, forbidden absorption and emission transitions are observed, decay rates are changed, and multiple peaks are found in absorption and emission bands.

## 4-2 Review of previous data

The reported spectra of atomic impurities in liquid helium and other noble gas matrices are mainly from three types of experiments: white light absorption in solid

matrix, laser induced fluorescence (LIF), and recombination emission spectra (RES) of neutral atoms in liquid helium. Matrix isolation spectroscopy has been applied to study various atoms in different solid matrices. Experimental results show that the spectra can depend strongly on the deposition and annealing conditions. It is thought that impurity atoms may occupy different sites corresponding to substitution or interstitial positions. The annealing of the matrix will eliminate the unstable sites. LIF is often used to study the excitation and emission spectra of atoms or ions by exciting them with a wavelength-tunable laser source. The excitation spectrum is obtained by counting the emission rate as a function of excitation wavelength, and the fluorescence spectrum is analyzed by a spectrometer. Recombination emission spectra are obtained by drawing positive ions into LHe, where they are neutralized by field emission electrons from a sharp tip. This recombination process leaves the atom in excited states, from which light emission is observed as the atom cascades down to the ground state. The optical spectra of impurities in LHe and in other solid noble gas matrices will be summarized in Section 4-2-1 and Section 4-2-2 respectively. More detailed information can be found in the review articles [1,2].

**4-2-1 Optical spectra of impurities in liquid He**

It is expected that impurities in LHe form two structures known as bubbles and snowballs as discussed in Chapter 3. Different structures might cause differences in the optical spectra in LHe since the interaction is different; therefore laser spectroscopy is a second method to study the impurity structures besides mobility measurements.

Common features of LIF spectra of atomic impurities in LHe are an absorption band of modest width (~5 nm), blue-shifted by few nm, and a narrower emission band

(~1nm) slightly shifted compared to the vacuum transition. For example, optical spectra for the $6s^2$-6s6p transition of Ba in superfluid helium are shown in Fig. 4-5 [1]. A broader absorption band with 5.5 nm bandwidth and 6.5 nm blue shift is seen in (a), and a narrow emission line with 0.8 nm linewidth and small shift is observed in (b).

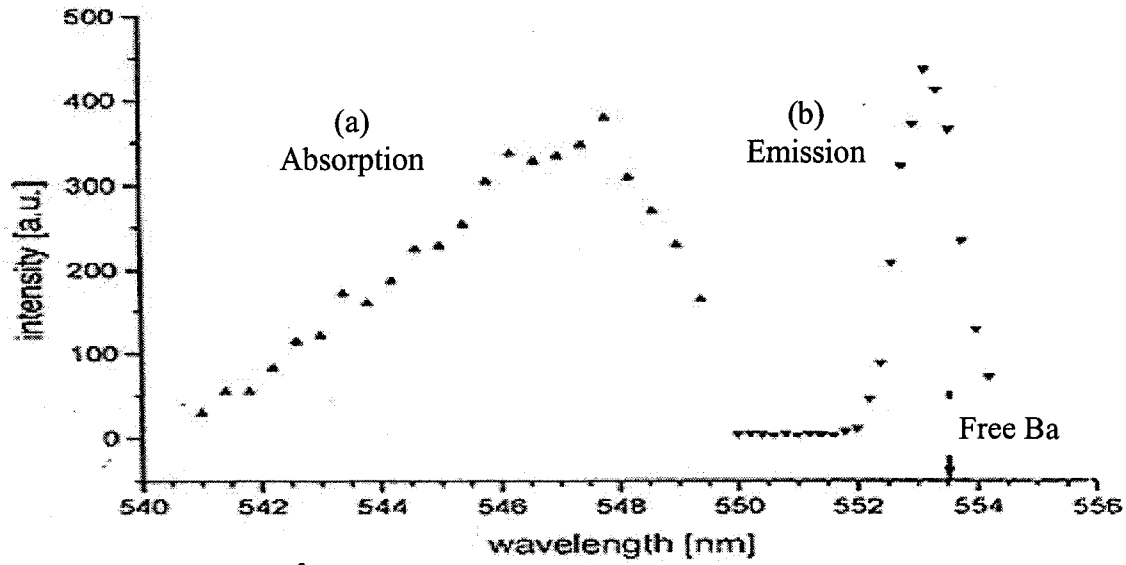


**Figure 4-5 The $6s^2$-6s6p transition of barium in superfluid helium at 1.3 K. The absorption line is wider and is more blue-shifted than the emission line relative to the vacuum transition [1].**

In the recombination spectra, it is of relevance to the proposed experiment to note that emission is observed on strong P→S transition in most of the transitions studied. The possible quenching of strong optical transitions of light alkali atoms (Li, Na and K) was found. No optical emission between 200 and 900 nm was discovered [1,7]. Another example is from the spectra of Cu, Au, and Ag atoms, where some transitions into the atomic ground state are missing even though their upper levels are known to have been populated [1,8]. The absence of allowed transitions might be due to the crossing of states

as in Fig. 4-2, leading to relaxation to other states, or due to the formation of an exciplex structure, which causes the emission to fall into the infrared beyond the detection region.

Some laser-induced fluorescence spectra from the $S_{1/2} \leftrightarrow P_{3/2}$ transition have shown clear splitting of the absorption peak. For example, the transition of $Ba^+$ ions from 6s $^2S_{1/2}$ to 6p $^2P_{3/2}$ in superfluid helium is shown in Fig. 4-6. It is not clear whether the 6p $^2P_{1/2}$ to 6s $^2S_{1/2}$ transition of $Ba^+$ in helium is split or simply has asymmetric shape [9]. The double excitation peaks can be explained by the dynamic Jahn-Teller effect in the 6p $^2P_{3/2}$ state induced by quadrupole deformation of the bubble structure. Once the electrons are excited from the spherical symmetric $^2S_{1/2}$ state to $^2P_{3/2}$ state, the wave function is not isotropic any more. The bubble will deform, and the quadrupole distortion of the helium matrix is strong enough to break the two-fold degeneracy of the $^2P_{3/2}$ state [9].

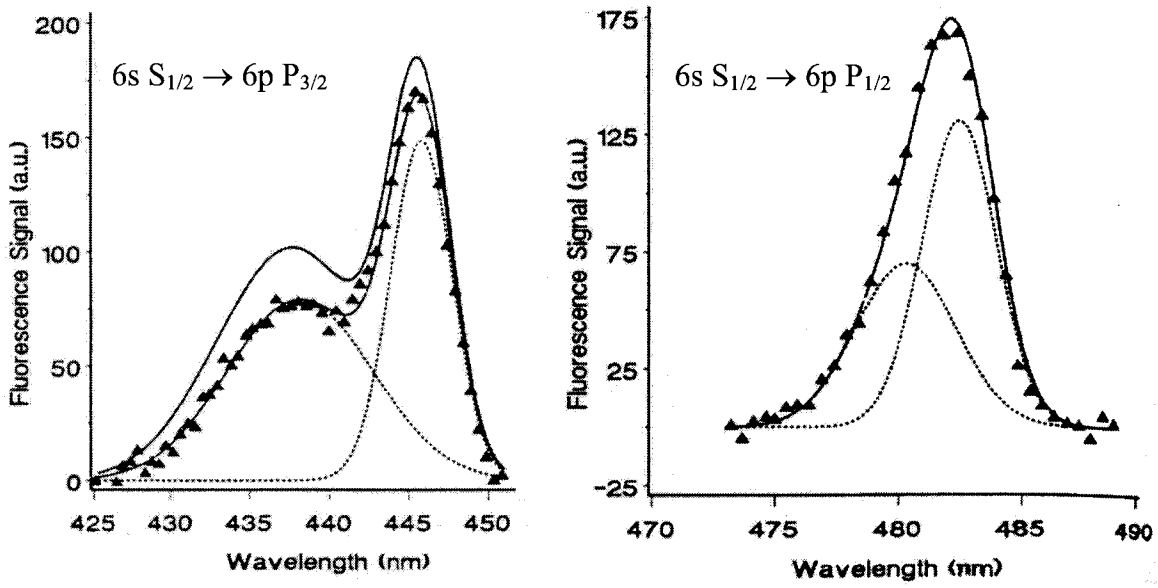


**Figure 4-6 Excitation spectra of $Ba^+$ in liquid helium. The 6s $S_{1/2} \rightarrow$ 6p $P_{3/2}$ transition shows a splitting into two peaks due to the Jahn-Teller effect [9].**

More spectral results of impurities in liquid helium are summarized in Table 4-2. Discrepancies in observations between methods, e.g. for $Sr^+$ in Table 4-2, may indicate that non-observation of emission in one method or experiment may not preclude observation in another.

**Table 4-2 Optical spectra of impurities in liquid helium measured by recombination spectroscopy (RES) and laser-induced fluorescence (LIF) (unit: $cm^{-1}$).**

| Atom | T(K) | Transition | Vacuum Transition | Experimental Method | Absorption S→ | Emission P→S | P→D | Ref. |
|---|---|---|---|---|---|---|---|---|
| Ba | 1.3 | $6s^1S_0$-$6p^1P_1$ | 18060.3 | RES | | 18067.7 | | [8] |
| $Ba^+$ | 1.5 | $6s^2S_{1/2}$-$6p^2P_{1/2}$ | 20261.6 | | 20728.2 | 20356.8 | 15432.6 | [9] |
| $Ba^+$ | 1.5 | $6s^2S_{1/2}$-$6p^2P_{3/2}$ | 21952.4 | | 22430.4 | 20352.7 | 15427.9 | [9] |
| $Ca^+$ | | $4s^2S_{1/2}$-$4p^2P_{1/2}$ | 23715.2 | | | NO | | [10] |
| Cs | | $6s^2S_{1/2}$-$6p^2P_{1/2}$ | 11178.2 | | 11413.0 | 11204.5 | | [10] |
| K | | | | RES/LIF | | NO | | [8] |
| K | | $4s^2S_{1/2}$-$4p^2P_{1/2}$ | 12985.2 | LIF | | NO | | [10] |
| Li | | | | RES/LIF | | NO | | [8] |
| Li | | $2s^2S_{1/2}$-$2p^2P_{1/2}$ | 14903.7 | LIF | | NO | | [10] |
| Na | | | | RES/LIF | | NO | | [8] |
| Na | | $3s^2S_{1/2}$-$3p^2P_{1/2}$ | 16956.2 | LIF | | NO | | [10] |
| Rb | | $5s^2S_{1/2}$-$5p^2P_{1/2}$ | 12579.0 | | 12850.6 | 12598.0 | | [10] |
| $Sr^+$ | | $5s^2S_{1/2}$-$5p^2P_{1/2}$ | 23715.4 | RES | | 23712.0 | | [11] |
| $Sr^+$ | | $5s^2S_{1/2}$-$5p^2P_{3/2}$ | 24516.8 | RES | | 24512.6 | | [11] |
| $Sr^+$ | | $5s^2S_{1/2}$-$5p^2P_{1/2}$ | 23715.4 | LIF | | NO | | [10] |
| $Yb^+$ | 1.4 | $6s^2S_{1/2}$-$6p^2P_{1/2}$ | 27061.8 | | 27706.0 | 27194.0 | | [12] |
| $Yb^+$ | 1.4 | $6s^2S_{1/2}$-$6p^2P_{3/2}$ | 30392.2 | | 30948.0 | 27194.0 | | [12] |
| $Yb^+$ | | $6s^2S_{1/2}$-$6p^2P_{1/2}$ | 27061.8 | | 28253.0 | 27370.0 | | [12] |

### 4-2-2 Optical spectra of impurities in solid matrix

For the experiments with impurities in solid noble gas matrix, only a small fraction ($10^{-3}$-$10^{-4}$) of impurity is imbedded to the sold matrix in order to avoid formation of impurity clusters. Spectra are taken by the methods of white light absorption or laser-induced fluorescence. Three examples, Na, Au and $Ca^+$, in solid matrices are outlined here. The spectra of Na in solid matrices are shown in Fig. 4-7 and Fig. 4-8 [13].

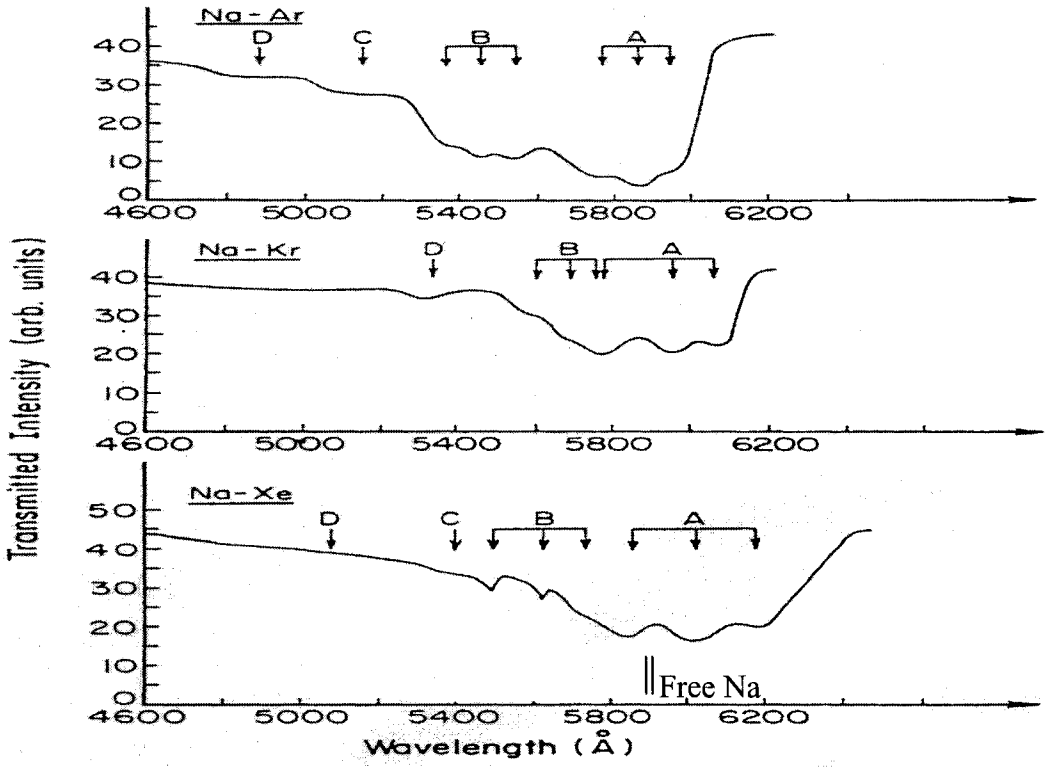


**Figure 4-7 Normalized scans of the absorption of white light by Na atoms trapped in solid Ar, Kr, and Xe at 10 K [13]. The arrows indicate the position of absorption peaks determined by laser excitation.**

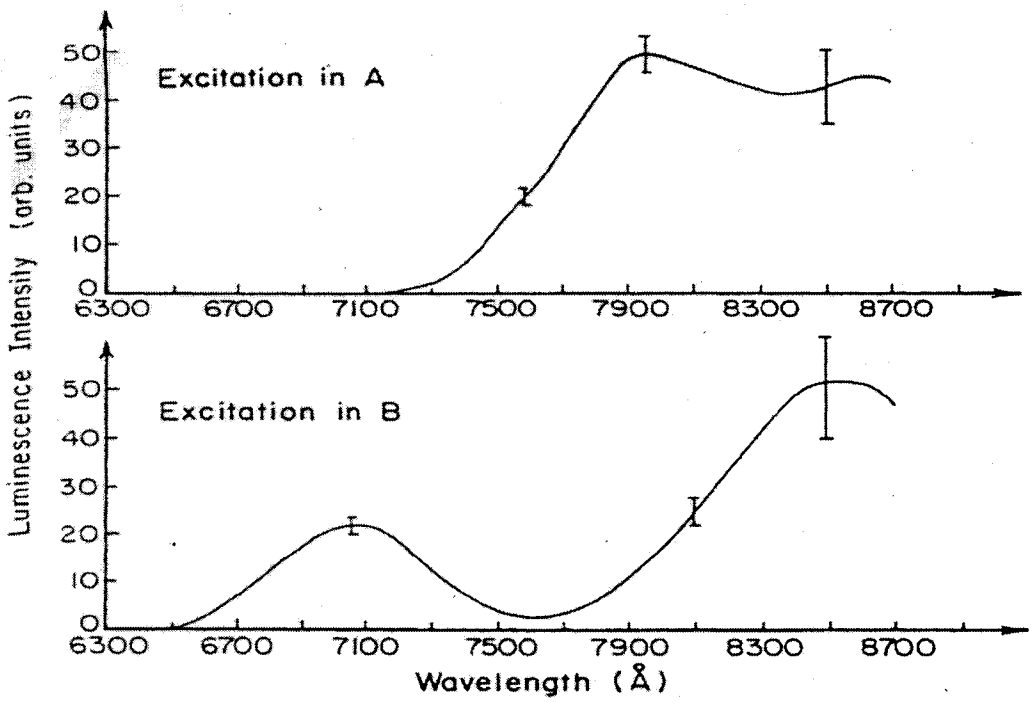


**Figure 4-8 The normalized luminescence of Na atoms in solid Xe at 10 K for excitation in absorption bands A and B [13].**

The absorption spectra consist of several broad absorption bands, in some cases with triplet structures. The center of the main peak is near the vacuum wavelengths, and shifts a little from blue to red with increased polarizability of the host matrix from argon to xenon. Fluorescence spectra of Na in solid xenon are shown in Fig. 4-8 [13]. The emission bands are also very broad and have large red shifts. The different emission spectra after excitation in bands A and B may indicate atoms trapped in different matrix sites. The two-well resolved bands in each fluorescence spectrum might correspond to two energy minima in the potential surface of excited states.

Absorption spectra of Au atoms in solid matrices show much sharper structures than in Na atoms as seen in Fig. 4-9 [14]. The $^2S_{1/2} \rightarrow {}^2P_{3/2}$ absorption band is split into two peaks due to the Jahn-Teller effect. The centers of the absorption bands for both $^2S_{1/2} \rightarrow {}^2P_{3/2}$ and $^2S_{1/2} \rightarrow {}^2P_{1/2}$ shift from blue to red with increased polarizability of the host matrix from argon to xenon. The emission spectra of Au in solid noble gas matrices are interesting and unusual. The schematic energy levels of Au atoms are shown in Fig. 4-10. Fluorescence from the transition $^2P_{1/2} \rightarrow {}^2S_{1/2}$ is completely quenched, but the parity forbidden emission lines of $^2D_{3/2} \rightarrow {}^2S_{1/2}$ and $^2D_{5/2} \rightarrow {}^2S_{1/2}$ are observed for all noble-gas matrices (Ar, Kr and Xe) [15].

Optical spectra of $Ca^+$ in solid argon shown in Fig. 4-11 are the only reported results for a monatomic ion in a solid noble gas matrix [16]. Relatively sharp features are observed both in absorption and emission spectra. The transitions are shifted insignificantly compared to the gas phase. The big differences of spectral properties of Na, Au and $Ca^+$ in solid matrices indicate large differences in their interaction with neighboring Rg atoms. Differences in polarizability, spin-orbit coupling, and bonding

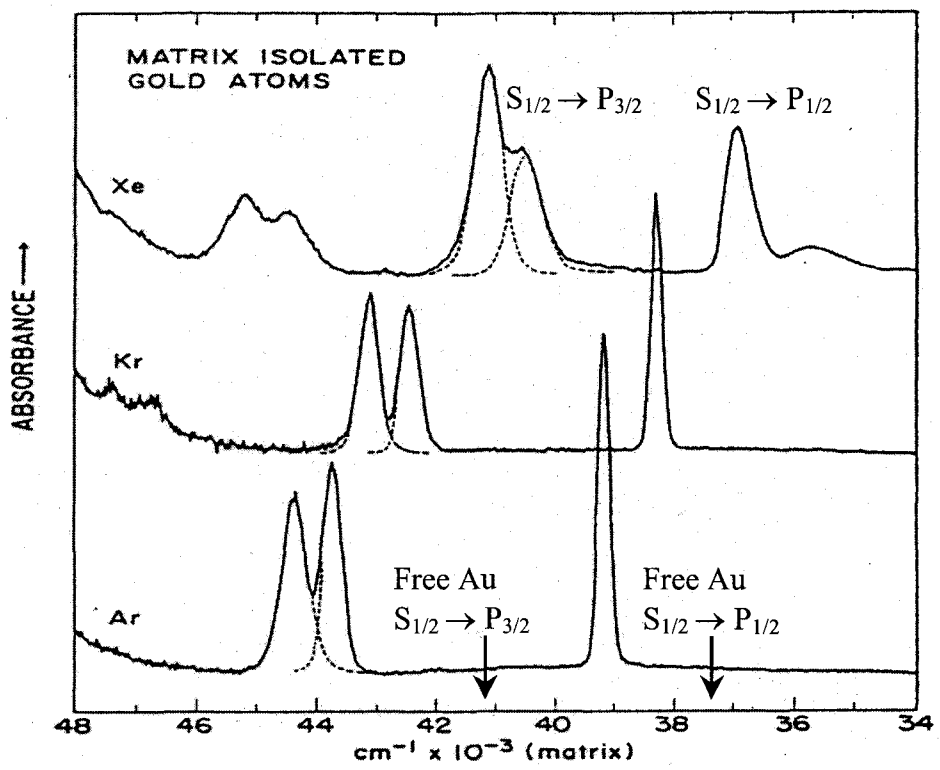


**Figure 4-9 Absorption spectra of Au atoms in solid Ar, Kr, and Xe matrices [14].**

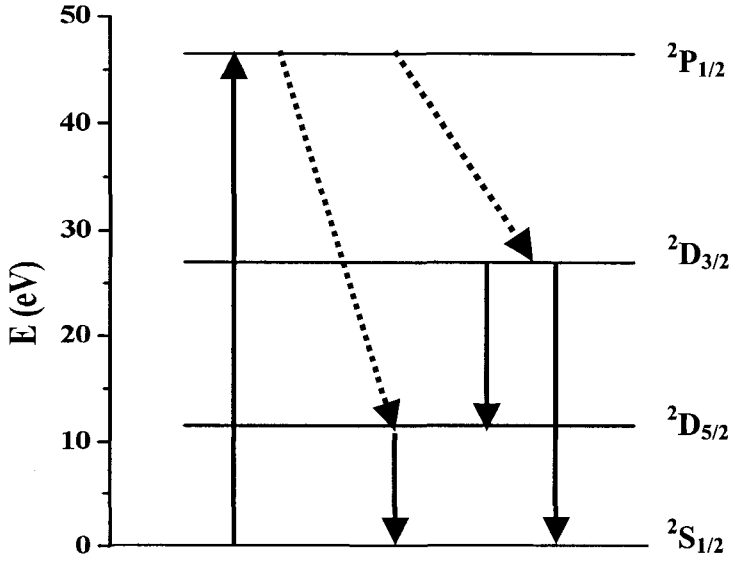


**Figure 4-10 Schematic energy diagram for Au atoms in solid matrix. Solid lines: radiative transitions; dashed line: non-radiative transitions [15].**

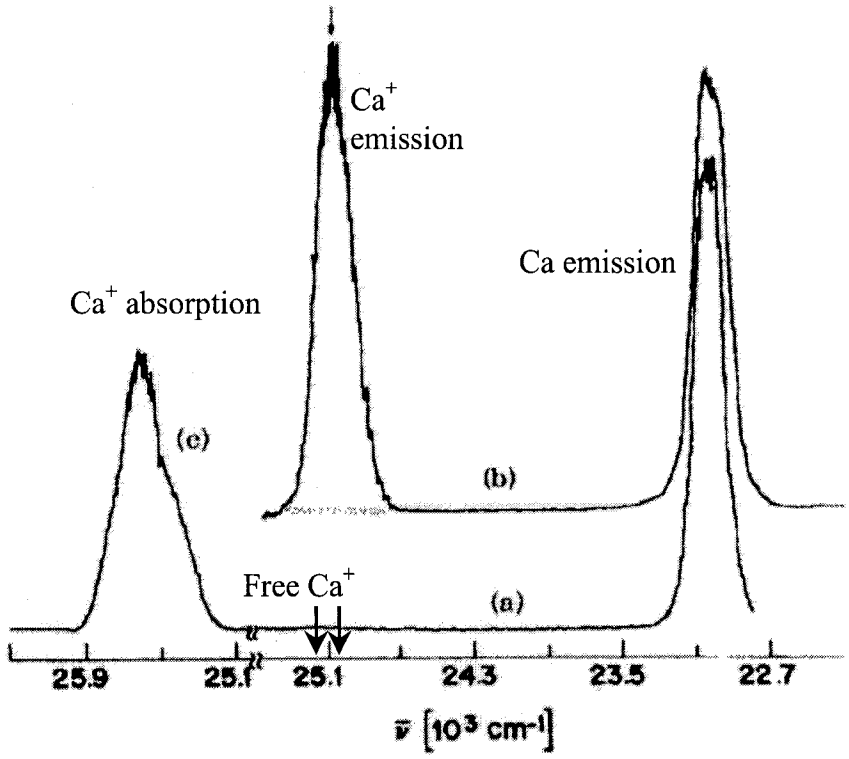


**Figure 4-11 Absorption and emission spectra of $Ca^+$ and Ca in solid Ar matrix [16].**

energy might also play a role.

In summary, there are three main features observed in the absorption spectra of atoms and ions in solid matrices (Ar, Kr and Xe).

1. A multiplet structure arising from the dynamic Jahn-Teller effect and spin-orbit coupling.

2. Differences in bandwidth, but with an increase in bandwidth in the Ar, Kr, Xe series.

3. Absorption band centered near the vacuum transition, with a systematic shift from blue to red in the Ar, Kr, Xe series.

For the fluorescence spectra, the large frequency shift observed in the emission of Na atoms in solid Ar, Kr and Xe is a signature of a large difference between equilibrium configurations of the ground and excited states. On the other hand, the Group I-B atoms (Cu, Ag and Au) and also $Ca^+$ show only small emission shift. It is not clear at present what makes them so different. More experimental spectral results for impurities in solid noble gas matrices are summarized in Table 4-3 [2].

**Table 4-3 Optical spectra of impurities in solid noble gas matrices (unit: $cm^{-1}$).**

| Atom | Host | T(K) | Transition | Vacuum Transition | Absorption S→ | Emission P→S | P→ | D→D | D→S | D→S | Shift | Width | Ref. |
|---|---|---|---|---|---|---|---|---|---|---|---|---|---|
| Au | Ne | 5 | $^2S_{1/2}$-$^2P_{1/2}$ | 37358.9 | 38891 | NO | NO | 12284 | 21502 | 9275 | 1532 | | [15] |
| Au | Ar | 5 | $^2S_{1/2}$-$^2P_{1/2}$ | 37358.9 | 39214 | NO | NO | 12267 | 22027 | 9799 | 1855 | | [15] |
| Au | Kr | 5 | $^2S_{1/2}$-$^2P_{1/2}$ | 37358.9 | 38295 | NO | NO | 12227 | 22099 | 9799 | 936 | | [15] |
| Au | Xe | 5 | $^2S_{1/2}$-$^2P_{1/2}$ | 37358.9 | 36819 | NO | NO | 12227 | 22027 | 9824 | -540 | | [15] |
| Ba | Ar | 10 | $^1S_0$-$^1P_1$ | 18060.3 | 18975 | 17606 | | | | | -454 | | [17] |
| Ba | Kr | 10 | $^1S_0$-$^1P_1$ | 18060.3 | 18587 | 17167 | | | | | -893 | | [17] |
| Ba | Xe | 10 | $^1S_0$-$^1P_1$ | 18060.3 | 17963 | NO | | | | | | | [17] |
| Ba | He | | $^1S_0$-$^1P_1$ | 18060.3 | 18445 | 18121 | | | | | 61 | | [18] |
| Ca | Ar | | $^1S_0$-$^1D_2$ | 21849.61 | 22200 | | | | | NO | | | [19] |
| Ca | Ar | | $^1S_0$-$^1P_1$ | 15157.91 | | 15272 | | | | | 114 | 235 | [19] |
| Ca | Ar | | $^1S_0$-$^1P_1$ | 23652.3 | 23750 | 23590 | | | | | -62 | 155 | [19] |
| Ca | Ar | 5 | $^1S_0$-$^1P_1$ | 23652.3 | 23100 | | | | | | | | [16] |
| Ca+ | Ar | 5 | 4s-4p | 25191.5 | 25750 | 25100 | | | | | -92 | 300 | [16] |
| Cs | Ar | 10 | 6s-5d | 14552 | 15621 | | | | | 13120 | | | [20] |
| Cs | Ar | 10 | 6s-6p | 11591 | 11831 | 10306 | | | | | | | [20] |
| Cu | Ne | 5 | $^2S_{1/2}$-$^2P_{1/2}$ | 30535.3 | 31745 | 28632 | NO | | 13213 | 11186 | -1210 | | [15] |
| Cu | Kr | 5 | $^2S_{1/2}$-$^2P_{1/2}$ | 30535.3 | 31826 | NO | NO | | 13512 | 11291 | 1290 | | [15] |
| Cu | Xe | 5 | $^2S_{1/2}$-$^2P_{1/2}$ | 30535.3 | 30745 | NO | NO | | 13431 | 11404 | 210 | | [15] |
| Cu | Ar | 5 | $^2S_{1/2}$-$^2P_{1/2}$ | 30535.3 | 32568 | NO | NO | | 13504 | 11461 | 2032 | | [15] |
| Li | Ar | 4.2 | 2s-2p | 14903.7 | 15420 | 11000 | | | | | -3904 | 1500 | [21] |
| Li | Kr | 4.2 | 2s-2p | 14903.7 | 15400 | 10300 | | | | | -4604 | 1500 | [21] |
| Li | Xe | 4.2 | 2s-2p | 14903.7 | 14860 | 9300 | | | | | -5604 | 1500 | [21] |
| Li | Ar | 10 | 2s-2p | 14903.7 | 14899 | 11059 | | | | | -3845 | 1000 | [22] |
| Li | Kr | 10 | 2s-2p | 14903.7 | 14811 | 10446 | | | | | -4457 | 1000 | [22] |
| Na | Ar | | 3s-3p | 16956.2 | 17017 | 14201 | | | | | -2755 | | [13] |
| Na | Kr | | 3s-3p | 16956.2 | 16802 | 13695 | | | | | -3261 | | [13] |
| Na | Xe | | 3s-3p | 16956.2 | 16607 | 12559 | | | | | -4397 | | [13] |
| Rb | Ar | 10 | 5s-4d | 19356 | | | | | | 15869 | -3486 | 2267 | [20] |
| Rb | Ar | 10 | 5s-5p | 12579 | 12883 | 12045 | | | | | -534 | 580 | [20] |

## 4-3 $Ba^+$ spectra and efficiency of a single $Ba^+$ detection in liquid xenon

The energy levels of $Ba^+$ in vacuum are shown in Fig. 4-12. There are two strong absorption transitions from the ground state 6s to the excited state 6p with the blue and blue-green transition wavelengths of 455.4 nm and 493.4 nm respectively. The excited ion can decay back to the ground state by emitting photons of the same wavelengths with transition rates of $1.11\times10^8$ $s^{-1}$ (455.4 nm) and $0.95\times10^8$ $s^{-1}$ (493.4 nm). It can also decay to 5d state by emitting red photons with a branching ratio about 0.24. The 5d state in vacuum is metastable with a lifetime of about 32 sec ($^2D_{5/2}$) and 48 sec ($^2D_{3/2}$) for decaying to the 6s state [23].

The optical spectra of a $Ba^+$ are changed when it is in liquid xenon. According to the discussion in Chapter 3 and our mobility measurements of $Ba^+$ in liquid xenon, it is believed the $Ba^+$ ions form a snowball structure where one or more solid xenon layers are around the ion core. Therefore, the best analogous spectra for $Ba^+$ ions in liquid xenon are those for impurity ions in solid noble gas matrix.

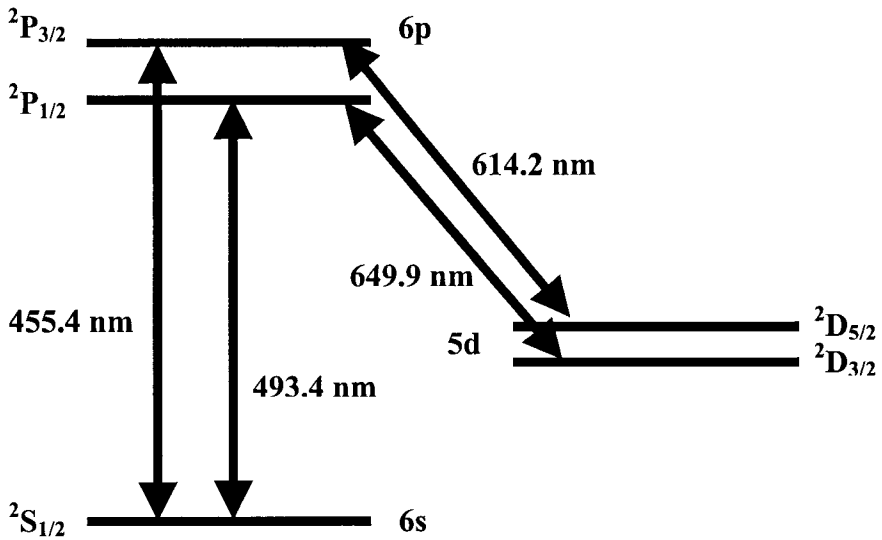


**Figure 4-12 Energy levels of a $Ba^+$ in vacuum.**

### 4-3-1 Educated guess of $Ba^+$ spectra in liquid xenon

For an ion in a solid or liquid matrix, the dominant interaction comes from the dipole induced potential in Eq. 4-2. A much higher bonding energy than for a neutral atom is expected. The only reported results of an atomic ion in liquid and solid noble gas matrix are $Ba^+$ [9,24] and $Yb^+$ in superfluid helium [12] and $Ca^+$ in solid argon matrix [15]. They all show narrow absorption and emission lines, and small shift with respect to vacuum transitions. The absorption peaks are known to be shifted from blue to red as the host atoms changed from argon to xenon due to the increased polarizability of the host atoms. Xenon has 20 times larger polarizability than helium as shown in Table 4-1. Therefore a larger red-shifted absorption band is expected for $Ba^+$ in liquid xenon than in liquid helium. In addition, the Jahn-Teller effect might also occur in our case, so three absorption peaks are expected from $^2S_{1/2} \rightarrow {}^2P_{1/2,3/2}$ transition. Although there is not enough information available to predict the shift and width of the emission for $Ba^+$ in LXe at present, a narrow and small red-shifted emission is expected. The overall educated guess of absorption and emission spectra of $Ba^+$ in liquid xenon is plotted roughly in Fig. 4-13. The absorption bands might be around 500 nm ($S_{1/2} \rightarrow P_{1/2}$), 465 and 450 nm ($S_{1/2} \rightarrow P_{3/2}$) with 15 nm in bandwidth, and the red-shifted emission bands might be around 520 nm ($P_{1/2} \rightarrow S_{1/2}$) and 475 nm ($P_{3/2} \rightarrow S_{1/2}$) with 30 nm in bandwidth. A wild guess for the absorption and emission spectra of the D$\leftrightarrow$P transitions are also illustrated in Fig 4-13. There is much less information for analogous transitions, so it is more difficult to predict these spectra.

The existence of non-radiative transitions or emission on forbidden transitions could impact the prospects for detecting $Ba^+$ in liquid xenon. If D-S state mixing exists

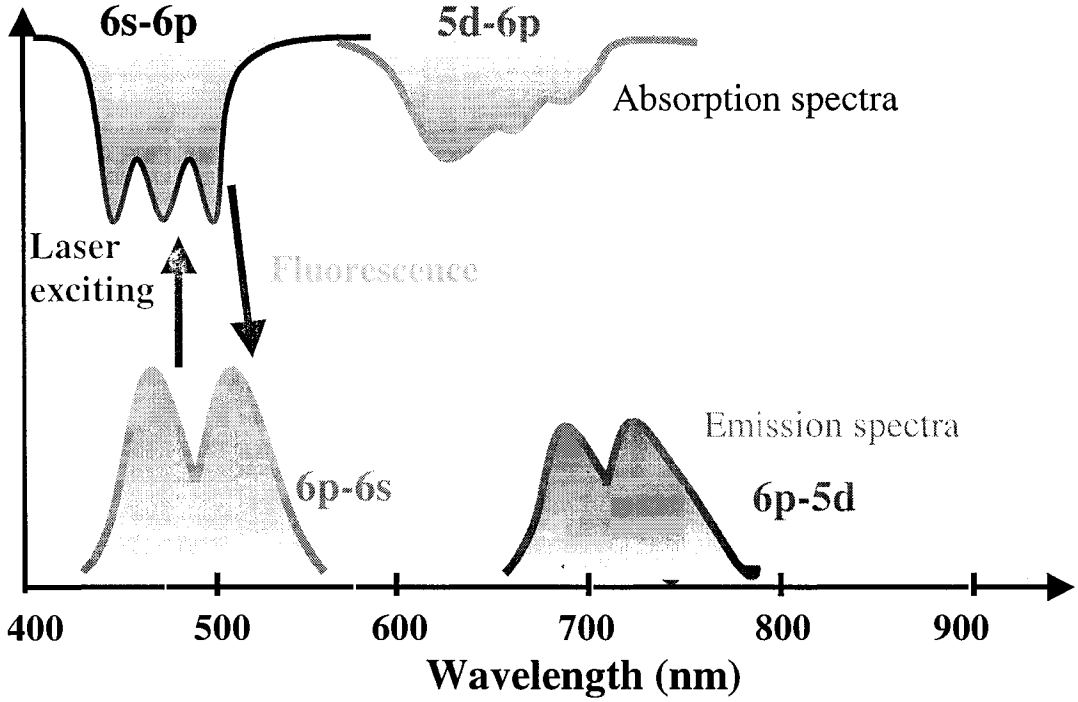


**Figure 4-13 Educated guess of absorption and emission spectra of $Ba^+$ in liquid xenon.**

for $Ba^+$ in liquid xenon, leading to fast relaxation or decay channels from D to S states, then the optical pumping effect would not exist. Thus a second laser would not be needed to pump the 5d population back to 6p state. This would be an advantage. On the other hand, quenching of $^2P_{1/2,3/2}$ to $^2S_{1/2}$ emission due to the possible crossing between $^2P_{1/2,3/2}$ and $^2D_{3/2,5/2}$ states would be disasters.

### 4-3-2 Efficiency of single $Ba^+$ ion detection in liquid xenon

The expected emission rate by laser excitation in a single ion detection experiment can be determined from the rate of absorption. The absorption cross section is a convenient parameter to express the apparent size of an atom interacting with the laser beam. For a Lorentzian line broadening, it is given as

$$\sigma_{12} = \frac{g_2}{g_1}\frac{A_{21}\lambda^2}{4\pi^2\Delta\nu}\left[\frac{1}{1+[2(\nu-\nu_c)/\Delta\nu]^2}\right], \qquad 4\text{-}3$$

where $g_1$, $g_2$ are the degeneracy of the lower and upper states, $A_{21}$ is the radiative decay rate for that transition, $\lambda$ is the excitation wavelength, $\Delta\nu$ is the absorption line width, $\nu$ is the laser frequency and $\nu_c$ is the center frequency of the absorption. Therefore, the absorption cross section of $Ba^+$ in liquid xenon can be estimated as

$$\sigma \approx \frac{\lambda^2}{4\pi^2}\frac{A_{21}}{\Delta\nu_{liquid}} \approx 4\times10^{-16} cm^2, \qquad 4\text{-}4$$

where we have assumed $g_2/g_1=1$, $\lambda$=502nm, $A_{21}=1.0\times10^8$ $s^{-1}$, and absorption bandwidth $\Delta\nu_{liquid}\sim18\times10^{12}$ Hz corresponding to $\Delta\lambda_{liquid}\sim$15nm. The expected excitation rate for a single $Ba^+$ ion is given as

$$W_{12} = \frac{\sigma}{A}\left(\frac{P}{h\nu}\right), \qquad 4\text{-}5$$

where $A$, $P$ and $h\nu$ are the area, power and photon energy of the excitation laser. The total fluorescence rate $R$ in real detection system, emitted by one $Ba^+$ ion is given as

$$R = \frac{\sigma}{A}\frac{P}{h\nu}\varepsilon_{QE}\varepsilon_C\varepsilon_{OP}, \qquad 4\text{-}6$$

where $\varepsilon_{QE}$, $\varepsilon_C$ and $\varepsilon_{OP}$ are the quantum efficiency of detector, collection efficiency and optics loss of detection system respectively. If one 502 nm laser with 2 W in power and 0.13 $cm^2$ in beam area is used for excitation, a single $Ba^+$ ion will then absorb and emit 15000 photons/sec according to Eq. 4-5. The efficiency parameters for a test size of 1 kg liquid xenon time projection chamber in dimension 200×50×42 $mm^3$ are summarized in Table 4-4. A total number of 440 counts and 8000 counts for 10 seconds tagging time are then detected by PMT and CCD, respectively.

The background noise will be mainly from light scattering in liquid xenon, dark counts of detectors and shot noise of the signal. The typical dark count rate for a PMT

**Table 4-4 Parameters of detection system and prediction for efficiency of single $Ba^+$ detection.**

| Parameter | Unit | 2" PMT(qty:8) | 2" CCD (qty:8) |
|---|---|---|---|
| Laser power | W | 2 | 2 |
| Wavelength | nm | 502 | 502 |
| Input photons | $sec^{-1}$ | $5\times10^{18}$ | $5\times10^{18}$ |
| Laser beam area (A) | $cm^2$ | 0.13 | 0.13 |
| Absorption cross section ($\sigma$) | $cm^2$ | $4\times10^{-16}$ | $4\times10^{-16}$ |
| Emission rate | photons/sec | 15000 | 15000 |
| Light collection efficiency ($\varepsilon_C$) | | 6% | 6% |
| Detector quantum efficiency ($\varepsilon_{QE}$) | | 5% | 90% |
| Filter transmission ($\varepsilon_{OP}$) | | 95% | 95% |
| Scattered light rate | counts/photon | $6\times10^{-20}$ | $10^{-18}$ |
| Tagging time | sec | 10 | 10 |
| Total detected photons ($N_t$) | counts | 440 | 8000 |
| Scattering light background: ($N_s$) | counts | 3 | 50 |
| Dark counts ($N_d$) | counts | 240 | ~0 |
| System noise ($N_r$) | counts | 0 | ~0 |
| Shot noise from the signal | counts | 21 | 90 |
| Total noise | counts | 37 | 126 |
| **S/N** | | **12** | **63** |

cooled to –30 °C is about 25 counts/second, and it is negligible for $LN_2$-cooled CCD camera. The system noise of CCD camera is the dominant noise, and it occurs only when the signal is read out. Therefore a longer tagging time is a benefit. A new technology called on-chip multiplication gain developed recently by Roper Scientific Inc. claimed the system noise of CCD camera can be reduced to at least one order smaller than the traditional one, and the reduction depends on the gain. Thus it is negligible if the gain is high enough in the order of 1000 [25]. The shot noise due to the random fluctuation of the detected photons is defined by the square root of the signal.

The Rayleigh and Brillouin scattering from density fluctuations in liquid xenon has been measured only at the scintillation wavelength (174 nm, dielectric constant

$\varepsilon \cong 2.85$). The scattering length is determined in range from 29 cm to 50 cm [26-28]. The scattering length ($\lambda_R$) as a function of dielectric constant and wavelength is given as [29]

$$\frac{1}{\lambda_R} = \frac{\omega^4}{6\pi c^4}\left\{k_B T \kappa_T \frac{[\varepsilon(\omega)-1]^2[\varepsilon(\omega)+2]^2}{9}\right\}, \qquad 4\text{-}7$$

where $c$ is the speed of light, $\omega$ is the frequency of radiation, $\kappa_T$ is the isothermal compressibility, $T$ is the liquid temperature, $k_B$ is the Boltzmann's constant and $\varepsilon(\omega)$ is the dielectric constant. According to Equation 4-7, the scattering length at 502 nm ($\varepsilon \cong 1.87$ [30]) is determined by scaling the wavelength and dielectric constant to 174 nm, and it is given as a range from 14300 cm to 24600 cm. Therefore, the amount scattered in a detection region of 4 mm diameter is estimated to be at a level of $2\times10^{-5}$. With the optical detection efficiency factors of 0.3% and 6%, this leads to stray light count rates of $6\times10^{-8}$ or $1\times10^{-6}$ of the laser input photon rate. In experiments to date, additional scattered light from reflection is small compared to this. Thanks to the advances of the thin-film technology, a Raman edge filter with an attenuation level of $10^{-6}$ and a high transmission level of 98% is available nowadays [31]. By using two Raman edges filters in the experiment, the background from scattering can be reduced to a very small and ignorable level $10^{-18}$ or less. The total noise in a signal–background measurement is then determined by

$$Noise = \sqrt{2N_t + N_s + 2N_d + 2N_r^2} \qquad 4\text{-}8$$

The simple estimation of signal and noise in Table 4-4 indicates that a single $Ba^+$ ion can be detected with 100 % efficiency with high signal-to-noise ratio. It should be noted that we have assumed in our calculation that the 5d population will relax to ground

state very rapidly so that the cycling transition of 6s-6p is maintained. If this does not occur naturally, another red laser is needed to pump the 5d population back to 6p state to eliminate the optical pumping effect. The large predicted signal-to-noise ratio for the CCD allows for substantial relaxation of the parameters in the final system. For example, the signal-to-noise ratio is still high enough for a single $Ba^+$ detection even the background is increased by two orders or the signal is reduced by two orders.

For a three level atom with a metastable state and no "repump" laser to prevent optical pumping, the atom will reach the metastable state after a few absorptions. There it will be no longer in resonance with the laser and of course, will no longer fluoresce. If the branching ratio is $\eta$ (the ratio of the p→d transition probability to the p→s transition probability), the maximum number of the emitted photons is given as [32]

$$N = \frac{1-\eta}{\eta}, \qquad 4\text{-}9$$

which is about 4 for $Ba^+$. This formula is useful for comparing our fluorescence results in Chapter 7.

# References


1. B. Tabbert et al., J. Low Temp. Phys. 109, 653 (1997).
2. C. Crepin-Gilbert and A. Tramer, Int. Rev. Phy. Chem. 18, 485 (1999).
3. Handbook of Chemistry and Physics, 67$^{th}$ edition, CRC press 1986.
4. S.H. Patil and K.T. Tank, J. Chem. Phys. 106, 2298 (1997).
5. C. Jouvet et al., J. Chem. Phys. 94, 1759 (1991).
6. F. S. Ham, J. Lumin. 85, 193 (2000).
7. H. Bauer et al., Physica B 165&166, 137 (1990)
8. B. Tabbert et al., Z. Phys. B 97, 425 (1995).
9. H.J. Reyher et al., Phys. Lett. A 115, 238 (1986).
10. Y. Takahashi et al., Phys. Rev. Lett. 71, 1035 (1993).
11. I. Baumann et al., J. Low Temp. Phys. 110, 213 (1998).
12. Y. Moriwaki and N. Morita, Eur. Phys. J. D 13, 11 (2001).
13. L.C. Balling et al., J. Chem. Phys. 69, 1670 (1978).
14. D.M. Gruen et al., J. Chem. Phys. 60, 89 (1974).
15. W. Schrittenlacher and D.M. Kolb, Ber. Bunsenges. Phys. Chem. 88, 492 (1984).
16. V.E. Bondybey and J.H. English, J. Chem. Phys. 75, 492 (1981).
17. L.C. Balling and J.J. Wright, J. Chem. Phys. 83, 2614 (1985).
18. S.I. Kanorsky et al., Phys. Rev. B 49, 3645 (1994).
19. V.E. Bondybey, J. Chem. Phys. 68, 1308 (1978).
20. L.C. Balling and J.J. Wright, J. Chem. Phys. 78, 592 (1983).
21. A.A. Belyaeva et al., OPT SPEKTROSK 34, 40 (1973).
22. J.J. Wright and L.C. Balling, J. Chem. Phys. 73, 3103 (1980).
23. W. Nagourney et al., Frequency Standards and Metrology, Editor: A. De Marchi, Springer-Verlag Berlin, Heidelberg (1989).
24. M. Himbert et al., J. Phys (Paris) 46, 2009 (1985).
25. Roper Scientific, Inc., Tucson, AZ 85706.
26. N. Ishida et al., Nucl. Instr. and Meth. A 384, 380 (1997).
27. A. Braem et al., Nucl. Instr. and Meth. A 320, 228 (1992).

28. V.Y. Chepel et al., Nucl. Instr. and Meth. A 349, 500 (1994).
29. G.M. Seidel et al., Nucl. Instr. and Meth. A 489, 189 (2002).
30. J. Marcoux, Can. J. Phys. 48, 244 (1970).
31. Raman Edge filters, Semrock, Inc., Rochester, NJ 14624.
http://www.semrock.com
32. C.Y. She et al., Opt. Lett. 2, 30 (1978).

# Chapter 5

## Experimental methods

This chapter will present the experimental apparatuses and methods for our mobility and spectroscopy measurements. Our first mobility research was done with the liquid xenon system in Prof. Miyajima's laboratory in Fukui University, Japan, and it will be described briefly in Section 5-1. Section 5-2 and Section 5-3 describe the details of cryogenic system and purification system at CSU, respectively. The methods of ion creation and identification will be discussed in Section 5-4 and Section 5-5. The electrode system for mobility measurements is described in Section 5-6, and the methods for mobility measurement and data analysis are discussed in Section 5-7. Three types of experiments for measurements of $Ba^+$ spectra in LXe are discussed and summarized in Section 5-8. The performance of various common filters for stray laser light attenuation is reviewed in the last section, Section 5-9.

### 5-1 Experimental system in Fukui

The experimental apparatus for mobility measurement in Fukui is shown in Fig. 5-1. The xenon cell was a commercial stainless steel cube with the 2-3/4 conflat flanges. It was cooled by transferring the cooling power from the $LN_2$ dewar with solid copper bars and plates joined to the xenon cell. The copper bar outside the vacuum chamber was retractable by using a feedthrough design, so it could make or break contact with the copper plate inside the vacuum chamber by manually adjusting the feedthrough. The cell was cooled at both top and bottom surfaces to reduce the thermal gradient across the cell. The temperature was regulated by 4 heaters and a Scientific Instruments 9650 temperature controller. The cell could be cooled down to the liquefaction temperature of

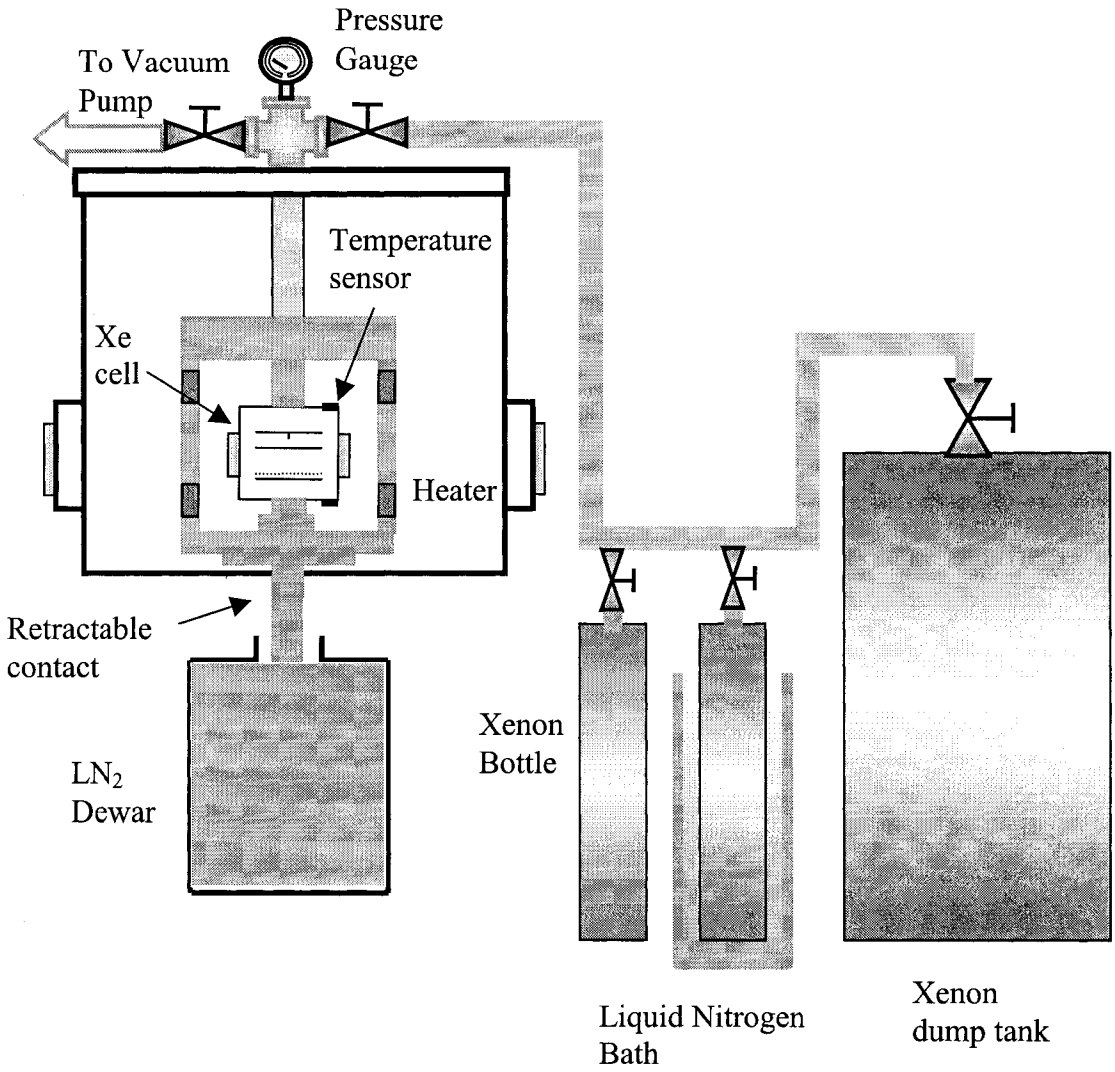


**Figure 5-1 Cryogenic and gas delivery systems in Fukui.**

xenon in 5 hours. The advantage of this cell was that it was made of ultrahigh vacuum stainless steel parts, and it could be baked out at a high temperature, and therefore the outgassing was reduced. Unfortunately, due to the poor thermal conductivity of stainless steel, bubbling around the electrode plates and the sharp edges of the conflat flange, and convection of LXe in cell were common after liquid xenon (LXe) production. Often visible bubbling was associated with severe noise in the collector plate signal, which

made mobility measurements difficult. In practice, measurements could be made only under certain transient condition in which there was no bubbling while the LXe was being produced or when the cell temperature was changed.

The xenon gas was previously purified by a high temperature Ti getter (~700K), and the purification system was not in use during the experiments. The liquid xenon was recovered using a stainless steel cylinder immersed in liquid nitrogen. A big tank of ~800 liters was installed for emergency use to dump the xenon in case the xenon cell reached an irregular high pressure due to an unexpected temperature increase.

Based on the experience of LXe production, gas purification and the bubbling problem in Japan, the apparatus as illustrated in Fig. 5-2 for mobility and fluorescence measurements in liquid xenon was designed and built at CSU. It includes a cryogenic system with two $LN_2$ cold traps in vacuum, a homemade copper xenon cell with indium seals, a xenon gas delivery and recovery system, and a gas purification system with a molecular sieve and a Zr-V-Fe getter. The details of each system and the detection methods for mobility and spectra measurements will be described in the following sections.

## 5-2 Cryogenic system and xenon cell

The design of the CSU cryogenic system was based on the following considerations. The pressure at triple point is about 0.8 atm. The triple and boiling points of LXe are 161.36 K and 165.03 K respectively, and that is only a 3.7 K range. Thus it is important to regulate the temperature of the xenon cell to better than 0.5 K. In addition, the xenon cell should be able to cool down to the required temperature for liquefying xenon. Furthermore, thermal gradient across the cell should be small for reducing

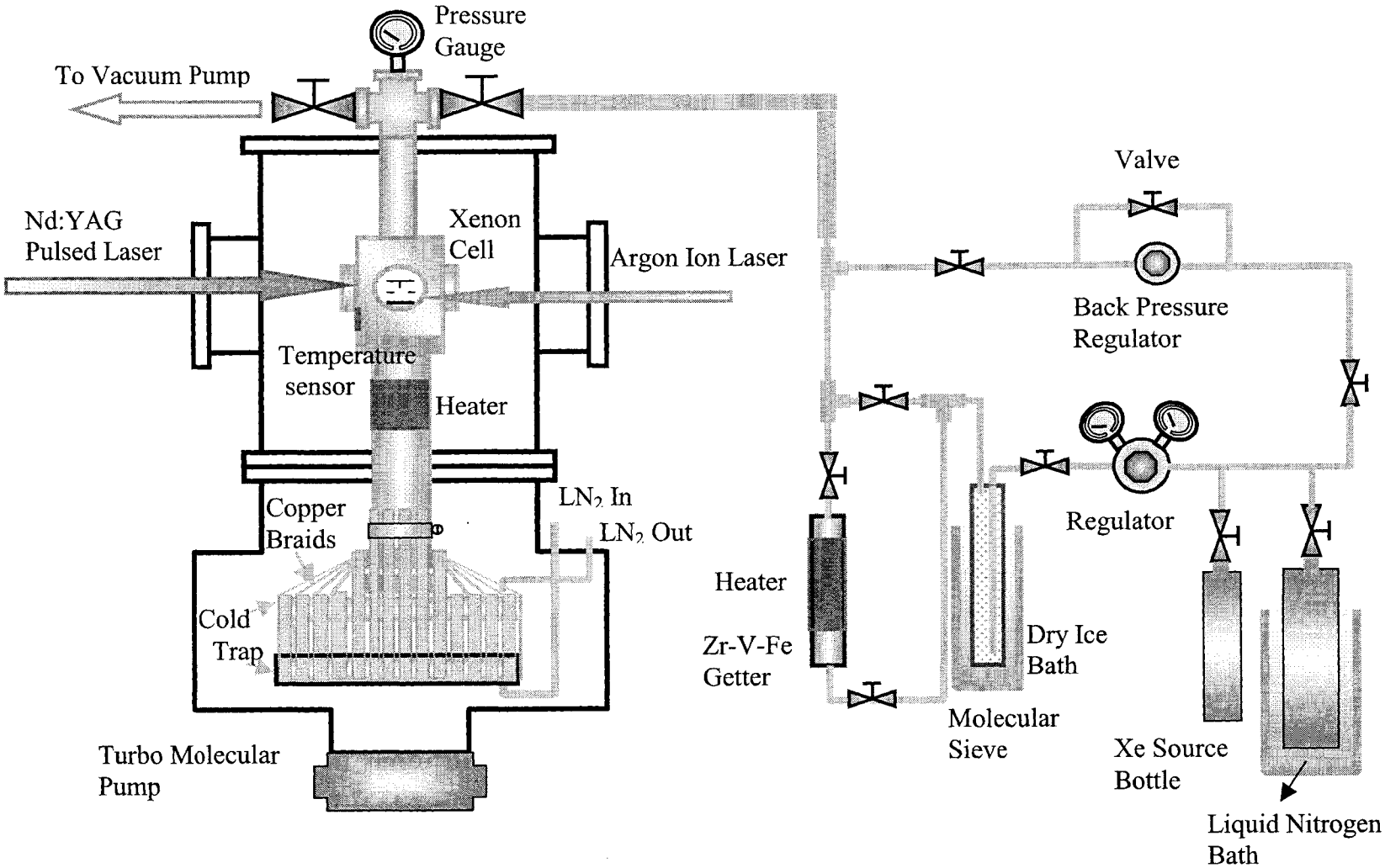


**Figure 5-2 A schematic of apparatus for condensing, purifying and delivering xenon gas at CSU.**

bubbling and convection in the liquid xenon.

In the cryogenic system, the xenon cell was cooled by connection with copper braids to two commercial cold traps filled with liquid nitrogen. Based on bubbling and convection problems in our earlier work in Japan, we decided to make our copper cell with indium-sealed quartz windows. This design reduced the temperature gradient across the cell due to the high thermal conductivity of copper and eliminated sharp edges at the windows.

A xenon cell with a size of 10cm×10cm×13cm was machined from a solid copper block. It is shown in Fig. 5-3. It has four quartz viewports and upper and lower surfaces sealed by indium wires. Indium is quite malleable, and it has been widely used for sealing cryogenic vacuum and high-pressure systems. The important factors to produce a reliable indium O-ring seal for use at low temperature (down to 2.0K) and moderate pressure (up to 82 bar) were discussed by Lim [1]. Our seals were based on his design. To ensure reliable leak-free performance for multiple temperature cycles, the copper flanges were checked and re-tightened from time to time to keep the torque on each bolt at 5 foot-pounds. The seals never broke in 3 years and over 50 times of usage.

The xenon cell was mounted inside a vacuum chamber evacuated by a turbo pump. The temperature of the cell was detected by a silicon diode and was temperature stabilized by feedback from a Lakeshore 331 temperature controller to a band heater around the copper tube attached below the cell. The temperature stability of the cell was better than 0.1 K, and the absolute temperature accuracy was about 1 K. Calibration of the temperature was done by measuring the boiling points of water and liquid nitrogen.

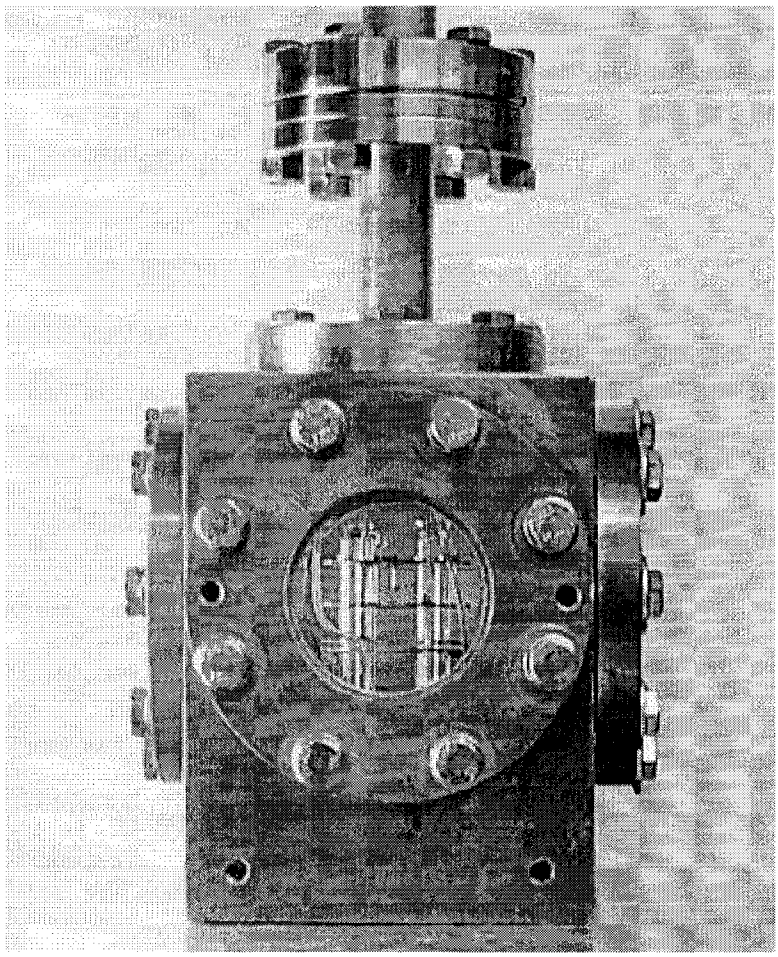

**Figure 5-3 A homemade copper xenon cell.**

The cooling system design was based on the following model. If there is temperature gradient, there are three ways heat energy can be transferred from one position to another: conduction, convection and radiation. The xenon cell was located inside a vacuum chamber, so we can ignore thermal convection. Although radiation is a significant factor, in our simplified model we also ignore it because it occurs from all parts of the system. For the consideration of thermal conduction, we can simplify our cryogenic system as shown in Fig. 5-4. The top of the xenon cell is exposed to the room temperature environment (Tr~300K), and the bottom is connected to the cold source with

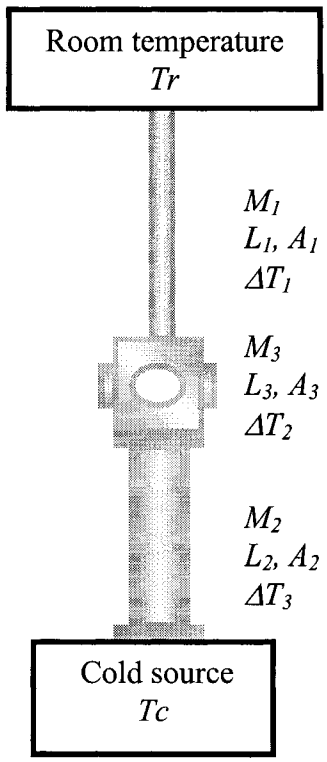


**Figure 5-4 A schematic diagram for analyzing thermal conduction.**

liquid nitrogen ($Tc$~77K). The rate of heat flow (heat current) across an element is given by

$$H = kA\left(\frac{\Delta T}{L}\right), \qquad 5\text{-}1$$

where $k$ is the thermal conductivity of the material, $A$ is the cross section, $L$ is distance and $\Delta T$ is the temperature difference across the element. Since the thermal elements are in series, $H$ is the same through each element. It is desired that $\Delta T$ is very small across the cell, large between the cell and room temperature, and moderately small between the cell and the cold source. It is also desired that $H$ is small in order to reduce the cooling requirements. In practice, H reduction is limited by the large $\Delta T_1$ (~130K) and by the property of element $M_1$. In order to reduce heat flow from $Tr$, we require that the material of $M_1$ should have poor thermal conductivity, a relatively long distance $L_1$ and small cross

section of area $A_1$. Stainless steel for high vacuum is a good choice for this purpose since it has low $k$ (0.3 J/sec/cm/K [2]). In practice, $A_1$ is limited by requirements of strength of vacuum pipe and pumping speed, and $L_1$ is limited by physical convenience. On the other hand, we require that the material of $M_2$ has the sufficient thermal conductivity, small distance $L_2$ and large cross section of area $A_2$ in order to transfer the cooling power from *Tc* more efficient. Hence, copper is a good material for $M_2$ ($k$ =7.1 J/sec/cm/K [2]). Thirty copper braids were also used in our system to achieve large enough $A_2$ in connecting the cold trap to the copper cylinder below the cell.

In the first test of the cryogenic system with only the upper cold trap connected with braids, the temperature of xenon cell did not get cold enough to liquefy xenon. Connecting both cold traps to the xenon cell by copper braids solved the problem. It also helped to purge the top of the cell with the excess of liquid nitrogen from filling the cold traps. This reduced *Tr* and helped to reduce the heat flow from the ambient environment. The CSU cryogenic system is quite successful. The xenon cell can be cooled down to 160 K in 14 hours, and there is no visible bubbling or intrinsic turbulence produced in the liquid xenon.

A timer with 12 setting programs and a solenoid valve installed in the $LN_2$ dewar were combined to work for an automatically $LN_2$-adding system. A security system was also used to keep the LXe at moderate temperature (~170 K) when unmonitored, and it was setup by a simple design. If the liquid xenon temperature became higher than the setting alarm level (~175 K), the temperature controller would trigger the solenoid valve, and $LN_2$ will be added to the cold traps. Simultaneously, an automatically dialer triggered by the alarm signal would telephone the people in charge.

## 5-3 Purification system

Impurities in the liquid xenon need to be reduced to a very low level to make sure that $Ba^+$ ions survive at lease several seconds during our measurements. Charge transfer reaction with impurities might neutralize $Ba^+$, or an Impurity-$Ba^+$ molecule could be formed in liquid xenon. In the final $0\nu\beta\beta$ decay experiment, an extremely high purity is required. The electron bunches must drift a distance of many tens of centimeters toward the x-y grids. For precise energy measurements, few electrons can be lost along the way. It is expected that the liquid xenon must have a high purity on the order of ppb or better [3-5]. The principal concern of purification for electrons survival is removal of electronegative impurities, such as $O_2$. For $Ba^+$ survival, the concern is removal of some impurities that will chemically react or charge transfer with $Ba^+$ ion. It has been demonstrated that liquid xenon purified by a combination of Oxisorb, molecular sieves and Zr-V-Fe alloy getter can reach an electron attenuation length longer than 2 m at an electric field between 0.5 kV/cm and 1.1 kV/cm [3-5].

Impurities in xenon can come from the production process, outgassing of vacuum materials and external leaks. The best grade of available xenon gas is about 99.999% pure. The total amount of electronegative impurities like $O_2$, $CO_2$, $H_2O$ is on the order of several ppm. Several hundred ppb of hydrocarbons also exist and must be removed. For our experiments, outgassing was reduced by baking the vacuum systems, except for the copper cell, for a few days. A vacuum better than $8\times10^{-7}$ torr was reached. The baking temperature of the xenon cell was kept at 312 K because of the low melting point of indium (~430 K), while the other vacuum systems were baked out around 370 K. Leaks were eliminated as best we can measure by careful sealing of every joint.

Many chemical and physical purification methods are available [6]. The purification system used in this experiment is illustrated in Fig 5-2. It was composed of molecular sieve 4A [7] (3.5 cm$\phi$×38 cm) and Zr-V-Fe getter [8] (3.5 cm$\phi$×8 cm) material installed in stainless steel pipes. The molecular sieve was operated at dry ice temperature to enhance the ability for absorbing water, hydrocarbons and polar molecules. Molecular sieve can be regenerated with baking, which mainly removes absorbed water. The Zr-V-Fe getter is a ternary alloy whose composition is 70% zirconium, 24.6% vanadium and 5.4% iron. Once the getter is activated at high temperature, gaseous impurities such as $H_2$, $H_2O$, CO, $CO_2$ and $N_2$ contacting with the surface are captured and chemisorbed onto the getter. After the impurities except hydrogen are absorbed, they cannot be released again even at very high temperature, due to the formation of strong chemical bonds with the alloy atoms. An impurity monitor, such as a residual gas analyzer, would be good to have on the system in the future to determine the effectiveness of the purification process and when to replace the Zr-V-Fe getter.

During the production of LXe, the xenon cell was filled with purified xenon gas flowing slowly through the molecular sieves 4A in dry ice bath and the high temperature (~100 °C) Zr-V-Fe alloy getter. The production of ~ 90 $cm^3$ LXe was normally finished in one hour. Liquid xenon was recovered through the backpressure regulator to the collecting cylinder by allowing the copper cell to slowly warm up and by immersing the collecting cylinder in liquid nitrogen.

## 5-4 Ion creation

In previously mobility studies, several methods have been used to create the ions. Evaporation and ionization of ions by a hot filament was widely used in the early work

[9]. Advances in the laser technology by the beginning of the 1980s provided a new way to generate the ions by laser ablation with a pulsed laser [10,11]. This method was also applied for our experiments. Barium ions were produced by laser ablation of a barium metal or Ba-Al alloy target at the focus of a pulsed Nd:YAG laser beam, operated at 1064 nm with a pulse duration of 10 ns. The typical ablating pulse energy was around 5 mJ and produced $10^7$-$10^9$ ions per shot (~ 1-50 pC). We have observed that barium ions can be generated efficiently in both gaseous and liquid xenon. It is interesting to note that $Yb^+$ ions production in liquid helium by laser ablation required two pulsed lasers with 0.1 ms delay time [11]. It was speculated that the first pulse produced neutral and/or ionic Yb clusters, and the second pulse efficiently dissociated and ionized the neutral clusters and/or dissociated the ionic clusters. In our experiments, no ionization enhancement was observed with two pulsed lasers. The difference might be that at the higher temperature in liquid xenon (170 K) there is less metal cluster formation than in liquid helium (1.4 K), or the different chemical nature of $Yb^+$ from $Ba^+$ could be important.

Laser ablation has been shown to be a powerful tool to generate many species of ions, but a downside is that the total number of ions created is not easy to control. Ion creation by a radioactive source is a better way to obtain ion yields that are smaller, down to the single ion level. Radiative methods used for mobility measurements include ionization of impurities in the gas or liquid by radiation [12] or depositions in the fluid by $\alpha$ decay [13,14]. Ion creation by $\alpha$ decay is a very convenient method to produce single ion in the fluid. The recoil momentum of an $\alpha$ particle is enough to knock the daughter ion from the surface of a radioactive sample. For example, the mobility of $^{208}Tl^+$ and $^{226}Th^+$ ions created by $\alpha$ decay of $^{212}Bi$ and $^{230}U$, respectively, were measured in LXe

recently [13,14]. The $^{208}Tl^{n+}$ ion production was accompanied by the release of a 6.39 MeV α-particles. The $^{208}Tl^{n+}$ ion gains a recoil energy of 116 keV, which is high enough for the $^{208}Tl$ to leave the surface of the sample plate and to enter the xenon gas or liquid. The $^{208}Tl$ may be initially in a multiply charged state after the recoil. It becomes $^{208}Tl^{+}$ by capturing electrons from xenon until the ionization potential of the next lower level, Tl, becomes less than that of Xe (Table 5-1 [2]). Although radioactive sources can provide a controllable number of ions, not any kind of ion can be obtained by a suitable radioactive source. For example, there is no method to produce $Ba^{+}$ by α decay.

**Table 5-1 Ionization potential of atoms**

| | Ionization potential (eV) | |
|---|---|---|
| Atom | I | II |
| Ba | 5.2 | 10.0 |
| Tl | 6.1 | 20.4 |
| Th | 6.0 | 11.4 |
| Xe | 12.1 | 21.2 |

## 5-5 Ion identification

Ions produced by laser ablation can be identified unambiguously by detecting the plasma emission spectrum, or by using a Time of Flight Mass Spectrometer (TOFMS). We have used a TOFMS with a total length of 230 mm to analyze the compositions of the plasma produced in laser ablation of a Ba-Al getter as shown in Fig. 5-5. The TOFMS was installed inside a vacuum chamber with the vacuum better than $10^{-6}$ torr. After the plasma was produced, the positive ions were extracted from the plasma to the flight tube by the electric field of the extractor. Then the ions were focused by the collimator and detected at the collector. A charge preamplifier and HP digital oscilloscope recorded the ion current. By measuring the drift time from the sample to the collector, the components

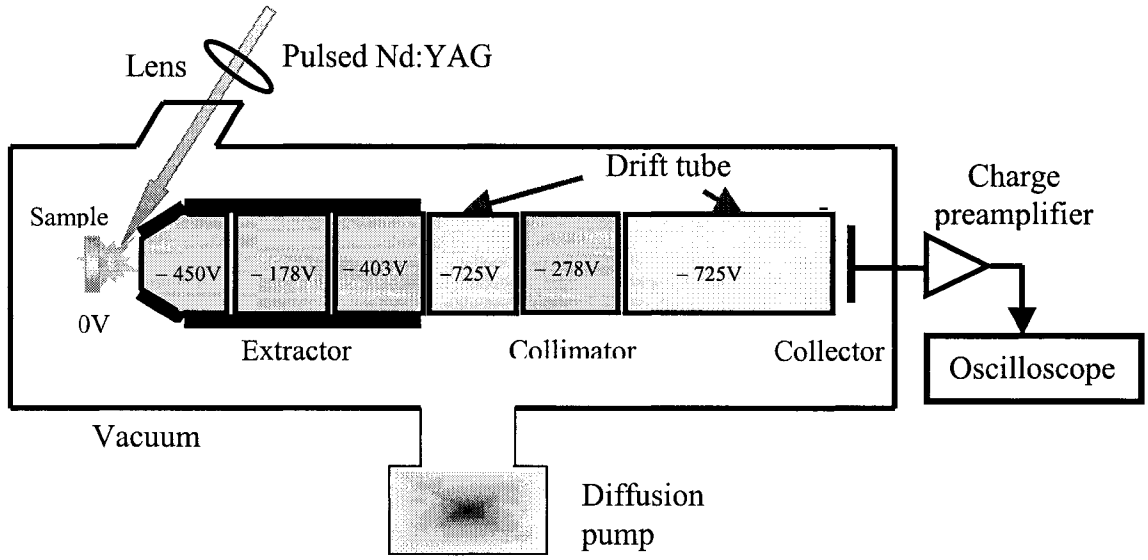


**Figure 5-5 A schematic diagram of Time of Flight Mass spectrometer.**

in the plasma can be determined. The time-of-flight signal from an ablated Ba-Al getter sample is shown in Fig. 5-6. The dominant peaks are $Al^+$ and $Ba^+$. There are also two small unknown peaks, $U1^+$ and $U2^+$, which could correspond to molecular or multiply charged species. The drift time ratio of $Al^+$ and $Ba^+$ agrees with the square root of their mass ratio very well. The size of individual ion signal versus the total ion signal for various amounts of laser ablation is shown in Fig. 5-7. The lines correspond to yield rates of 87%, 7%, 1% and 5% for $Ba^+$, $Al^+$, $U1^+$ and $U2^+$ respectively. Because the barium has smaller vaporization and ionization energy than the other atoms, it is expected and observed that the $Ba^+$ ion is the dominant component in the plasma. It is important to know this in order to have confidence that the mobility measured corresponds to that of $Ba^+$.

The identification of plasma compositions by emission means will be discussed in more detail in Chapter 7. As an example, the emission from laser ablation plasma in gaseous and liquid xenon recorded by a spectrometer with a CCD array detector is shown

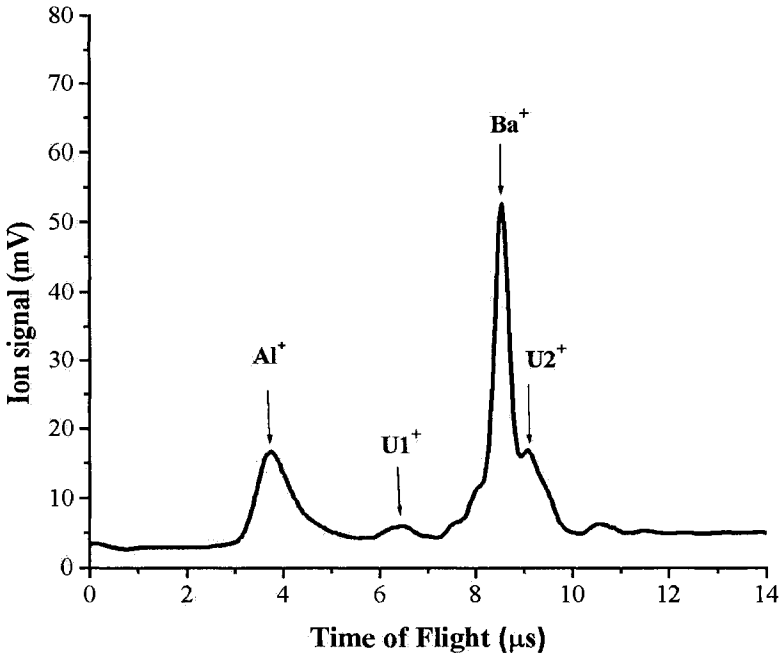


**Figure 5-6 Time of flight signal of laser ablation Ba-Al getter.**

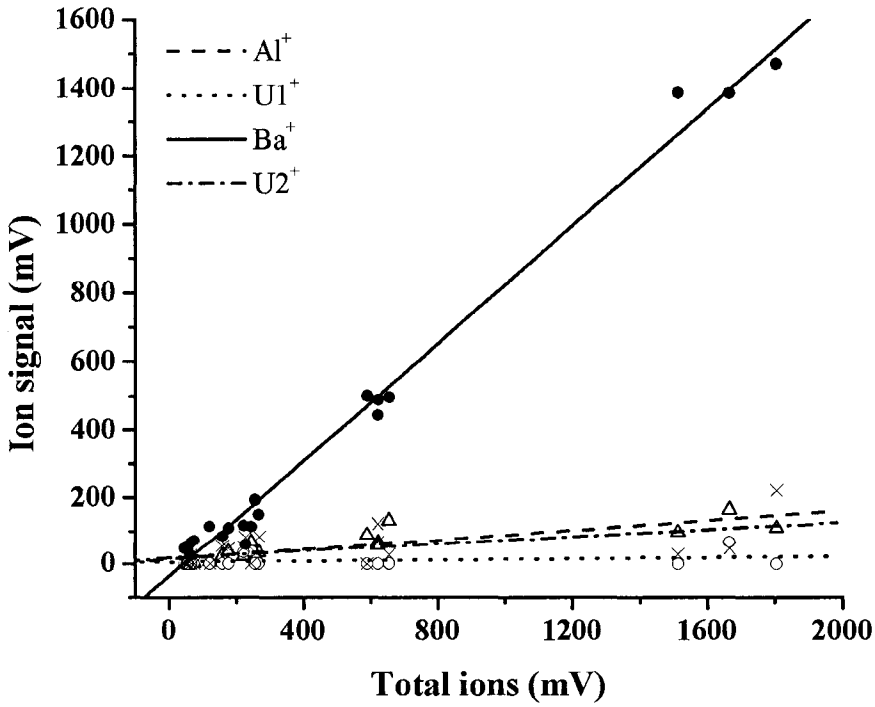


**Figure 5-7 Ions yield for each ion component in plasma.**

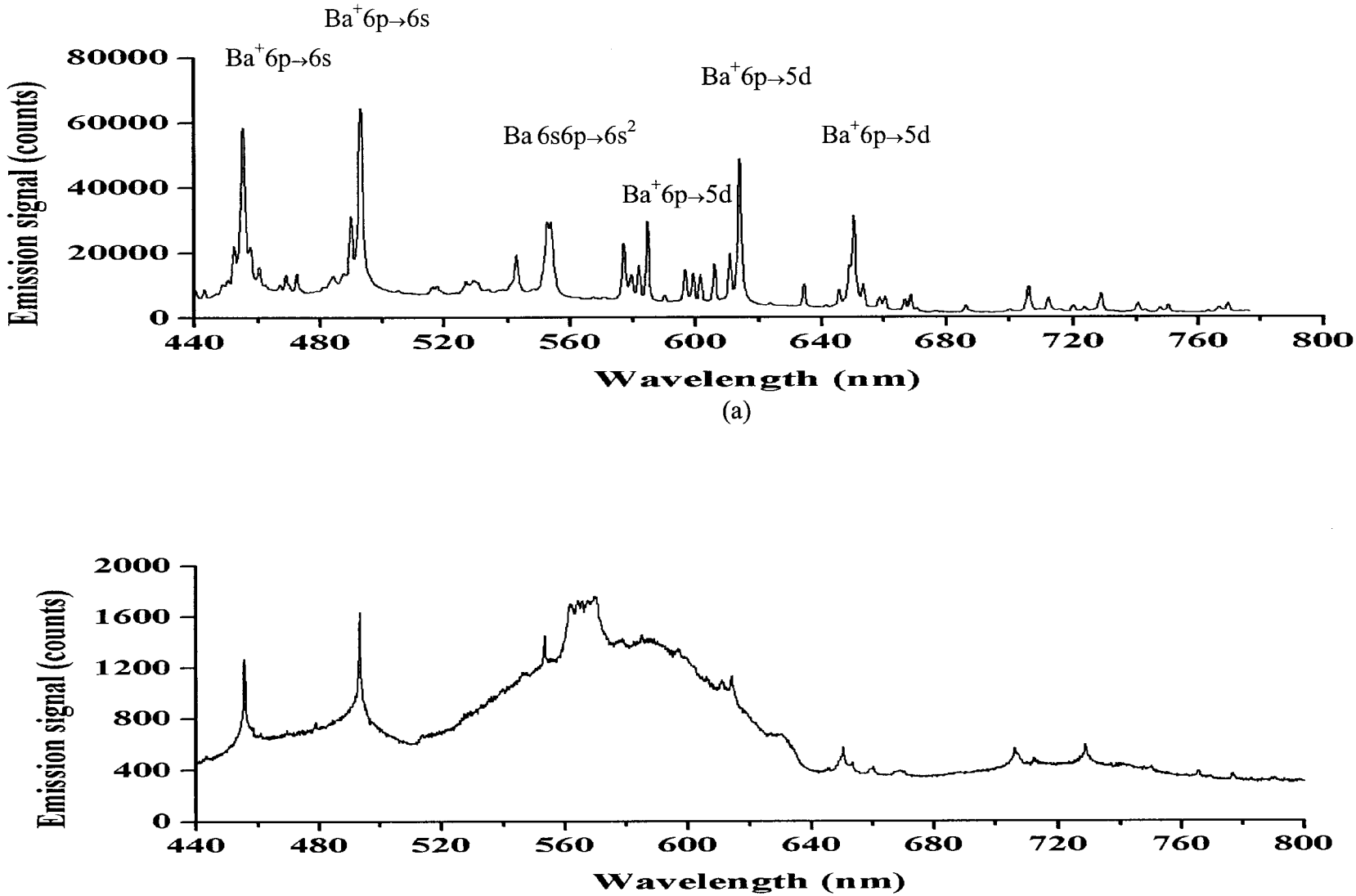


**Figure 5-8 Plasma emissions spectra of $Ba^+$ ions by laser ablation in (a) gaseous xenon and (b) liquid xenon**

in Fig. 5-8. Here, the ablation target is the barium metal rather than the Ba-Al getter. An important conclusion is that only the characteristic emission lines of Ba and $Ba^+$ are observed. Also we note that barium ions can be generated efficiently by laser ablation in both phases. The broadening of the spectrum observed in the liquid phase will be discussed in Chapter 7.

It should be mentioned that ions produced by α-decay can be identified by the characteristic decay mode and decay time. For example, $^{208}Tl^+$ production by α-decay of $^{212}Bi$ has been identified by its characteristic lifetime of 3.05 minutes [13]. This will be important in future for single ion measurement of $Ra^+$.

## 5-6 Electrode system

The electrode system mounted inside the cell was comprised of four circular plates made of stainless steel. It is illustrated in Fig. 5-9. The four plates were separated and insulated by quartz tubes. There were mesh wires with 90% transmission on both the acceleration plate and the Frisch grid in order to ensure more uniform electric field in the drift region. The spacing and the diameter of the mesh were 850 μm and 46 μm respectively.

Various electrode systems used for our mobility measurements are summarized in Table 5-2. A metal tip was mounted on the target plate where the highest positive potential was applied. Ions were produced at this tip by laser ablation. For our mobility measurements, we set the liquid xenon level at the acceleration plate, and ions were produced in the gaseous xenon at about 1-2 atm pressure. Although $Ba^+$ ions can be created efficiently in both gaseous and liquid xenon, laser ablation in liquid xenon produces small bubbles near the ablation spot. The resulting turbulence degrades the

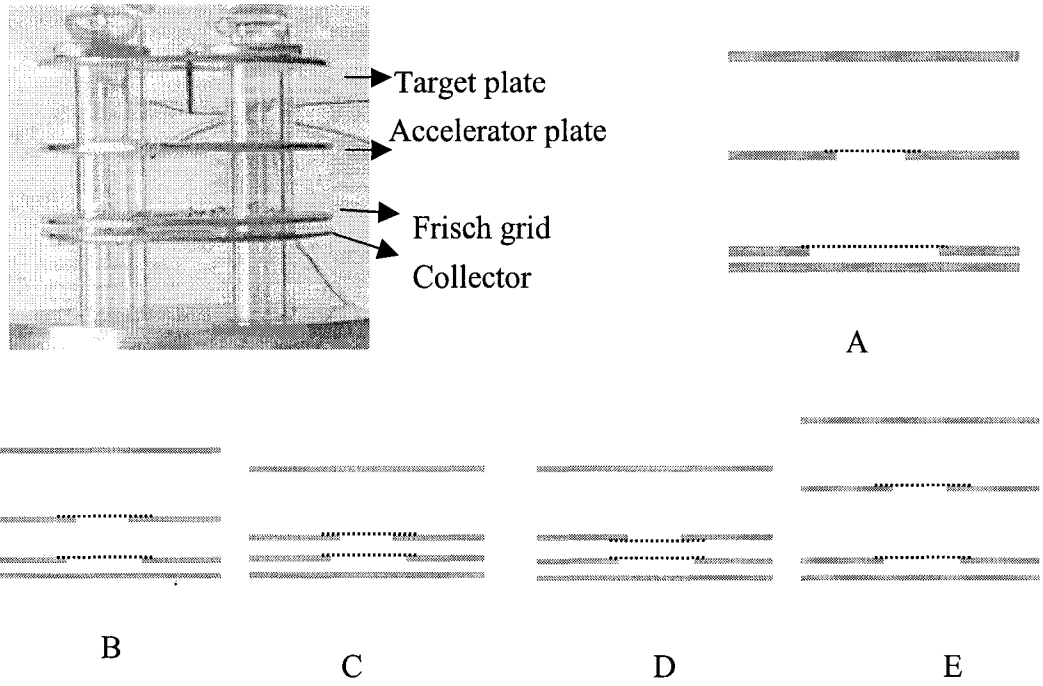


**Figure 5-9 Electrodes arrangements for mobility measurements.**

**Table 5-2 Parameters for each electrode system congiguration.**

| Electrodes system | A | B | C | D | E |
|---|---|---|---|---|---|
| plate thickness (mm) | 1 | 0.5 | 0.5 | 0.5 | 0.5 |
| distance: target plate to accelerator plate (mm) | 10 | 8 | 8 | 8 | 8 |
| distance: accelerator plate to grid plate (mm) | 8 | 5 | 2.3 | 2.3 | 9 |
| distance: grid plate to collector plate (mm) | 1 | 1 | 1 | 1 | 1 |
| diameter: aperture on accelerator (mm) | 9 | 7 | 7 | 7 | 7 |
| diameter: aperture on grid (mm) | 17 | 10 | 10 | 10 | 10 |
| $d_{eff}^2$ ($cm^2$) | 1.37 | 0.58 | 0.25 | 0.18 | 1.39 |
| d: liquid level to center of collecting region (mm) | 10 | 6.3 | 3.52 | 3 | 10.75 |

quality of the ion signal somewhat, and increases the uncertainty in the mobility measurement.

After the creation of ions by laser ablation, the positive ions move relatively quickly, in milliseconds, through the gas to the acceleration plate, where they enter the liquid through a grid. Then the ions drift at approximately constant velocity in a nearly uniform electric field. They are pulled through the Frisch grid to the collector plate by a

stronger electric field in the Frisch grid-collector region. The Frisch grid serves to shield the collector plate from induced current due to the motion of the ions in the drift region above it. Thus, no signal is seen on the collector until the ions begin to pass through the Frisch grid. The typical requirement for 100 % collection efficiency of ions through the Frisch grid is that the electric field in collection region is at least 2 times bigger than in the drift region [15].

The equipotential contours for one electrode configuration calculated by the program SIMION 6.0 [16] are shown in Fig. 5-10. It is seen that the electric field is not uniform near the target and the apertures of the plates due to the plate thickness. Therefore, the mobility is related to an integral of *ds/E* along the drift path of the ions. A convenient equation is

$$\mu = \frac{V\int\frac{ds}{E}}{Vt_d} = \frac{d_{eff}^2}{Vt_d}, \qquad 5\text{-}2$$

where $V$ is the applied voltage on the acceleration plate. The $d_{eff}^2$ depends only on the

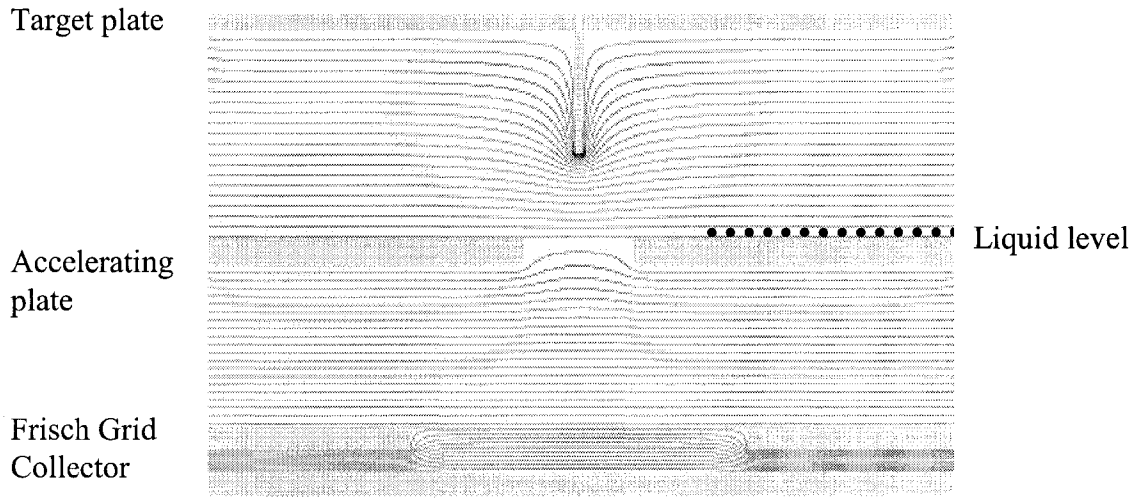


**Figure 5-10 Equal potential lines of electrodes simulated by SIMION 6.0**

geometric structure of the electrodes and not on the applied voltage as long as the voltages between the 4 circular plates are fixed in the same ratio. In practice, we use the program SIMION 6.0 to determine the direction of the drift path and the electric field $E$ along the path. The integral for $d_{eff}^2$ in Eq. 5-2 is performed manually and is expected to be reasonably.

## 5-7 Detection of ion current

The ion current signal was measured by a Keithley 610 electrometer and recorded by a HP 54501A digital oscilloscope with trigger signal from the pulsed laser. Due to the long time constant of the electrometer output on the order of a few seconds, the actual current must be determined by a correction procedure. It is derived by a calibrated sum of the recorded signal and its derivative. The appropriate fraction of each is determined by using a square wave test input through a large resistance R=$2\times10^9$ Ω as shown in Fig. 5-11. For our mobility measurements, the electrometer is typically set on the $0.1\times10^{-10}$ Amp scale, in which input resistance $R_1$ is $10^{10}$ Ω and input capacitance is 10 pF according to the manual. Note that because the input capacitance is very small, there may be significant additional capacitance in the actual circuit and cables.

The equivalent circuit of the electrometer in test mode is shown in Fig. 5-11. Kirchhoff's equations can be written down as

$$V(t) - RI - R_1 I_1 = 0 \qquad 5\text{-}3$$

$$I = I_1 + I_2 \qquad 5\text{-}4$$

$$V_1 = \frac{q_2}{C} = R_1 I_1 \qquad 5\text{-}5$$

$$V_{out} = MV_1 \qquad 5\text{-}6$$

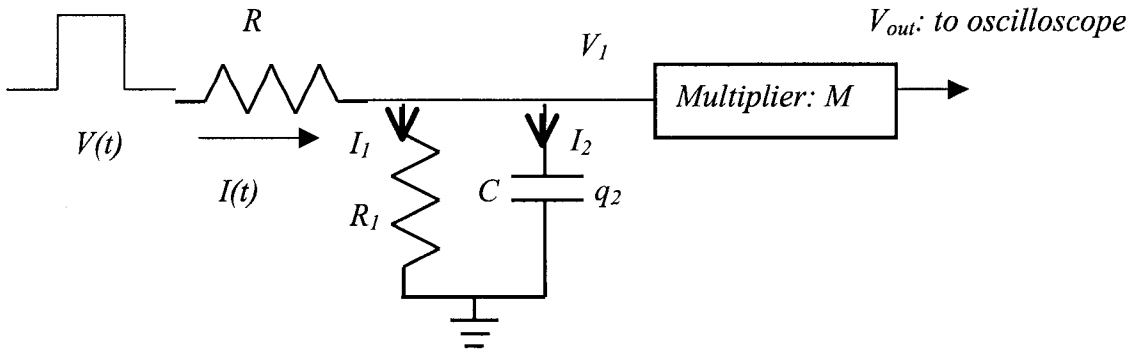


**Figure 5-11 Equivalent detection circuit of the electrometer: square wave input calibration mode.**

Substituting using Eq. 5-5 for $I_1$ and $I_2=dq_2/dt$ and using Eqs.5-4 and 5-6 in Eq. 5-3,

$$V(t) = \frac{R + R_1}{MR_1}(V_{out} + \tau_{eff}\frac{dV_{out}}{dt}), \qquad 5\text{-}7$$

where $\tau_{eff} = \frac{RR_1}{R + R_1}C$. The signals of a square wave input $V(t)$, the recorded signal $V_{out}$ from the oscilloscope and calculated input signal after a fit to Eq. 5-7 using the $V_{out}$ are compared in Fig. 5-12. One can see that the corrected signal is a good match to the input square wave. The best fit parameters are given as $\tau_{eff}$ = 0.70 sec and $M$ = –26. Thus the effective capacitance $C$ of the whole detection network is determined as 420 pF.

For the current detection circuit in Fig. 5-13, the true current signal in terms of the recorded voltage $V_{out}$ is given as

$$I(t) = I_1 + I_2 = \frac{V_1}{R_1} + C\frac{dV_{1t}}{dt} = \frac{1}{R_1 M}(V_{out} + R_1 C\frac{dV_{out}}{dt}), \qquad 5\text{-}8$$

where the effective time constant $R_1C$ is 4.2 sec for the detection circuit.

One raw data $V_{out}$ recorded by oscilloscope and the corrected signal $I(t)$ with some smoothing for a typical ion pulse of medium charge are shown in Fig. 5-14. It can be seen that the corrected signal pulse is quite different in shape from the raw output pulse $V_{out}$.

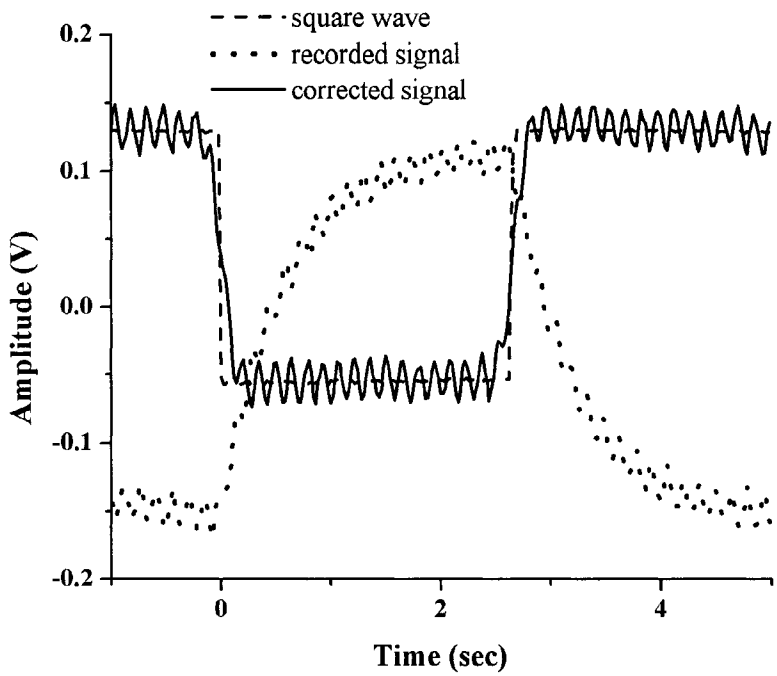


**Figure 5-12 Comparison of signals from a square wave test pulse, recorded trace on oscilloscope and time constant corrected pulse.**

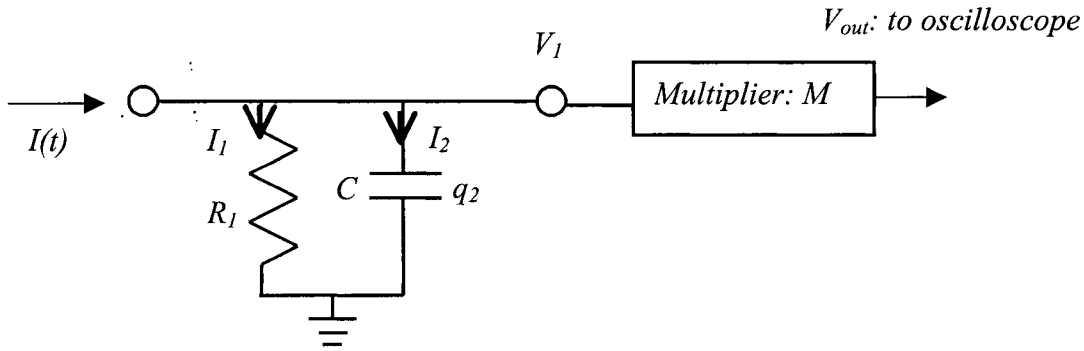


**Figure 5-13 Equivalent detection circuit of the electrometer: ion current detection mode.**

Each current pulse is fit to a Gaussian plus a constant DC offset, and the ion drift time is defined as the center of the Gaussian fit. The area of the Gaussian curve also determines the total charge of each ion pulse. The fitting curve and the fitting parameters for this pulse are shown also in Fig. 5-14. For a typical good signal with good Gaussian fit in

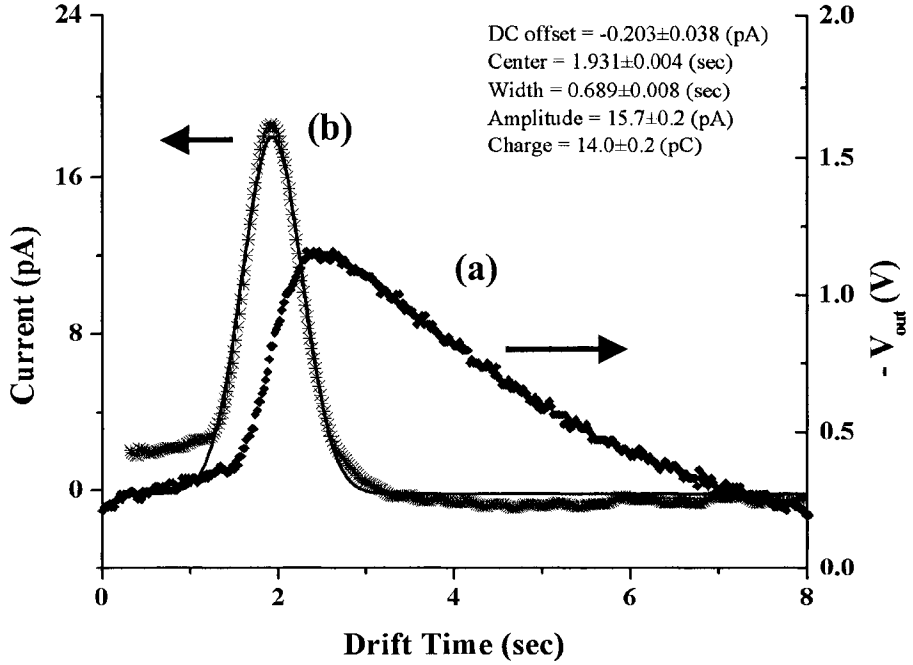


**Figure 5-14 Sample ion drift signal. (a) Raw signal recorded by an oscilloscope. (b) Corrected current signal by Eq. 5-8, and a Gaussian fit for determining the drift time and ion charge.**

Fig. 5-14, the fitting errors for drift time and charge are only ~0.2% and ~1 % respectively. In practice, a C++ program was written to analyze a data set with thousands of pulses. Each fit is displayed so that the program operator can reject pulses where the noise is high or the shape is anomalous, and the fit is poor. Such a typical poor signal with a bad Gaussian fit that was rejected is shown in Fig. 5-15. Overall about 10% of the pulses were rejected in the mobility runs.

## 5-8 Detection systems for laser spectroscopy

Three different detection systems were used for studying the excitation spectrum, fluorescence spectrum and cloud image of $Ba^+$ ions in liquid xenon. In the excitation spectrum configuration shown in Fig. 5-16 (simplified figure), the nine discrete argon ion laser wavelength, 454 nm (5 mW), 458 nm (50 mW), 465 nm (27 mW), 472 nm (52 mW),

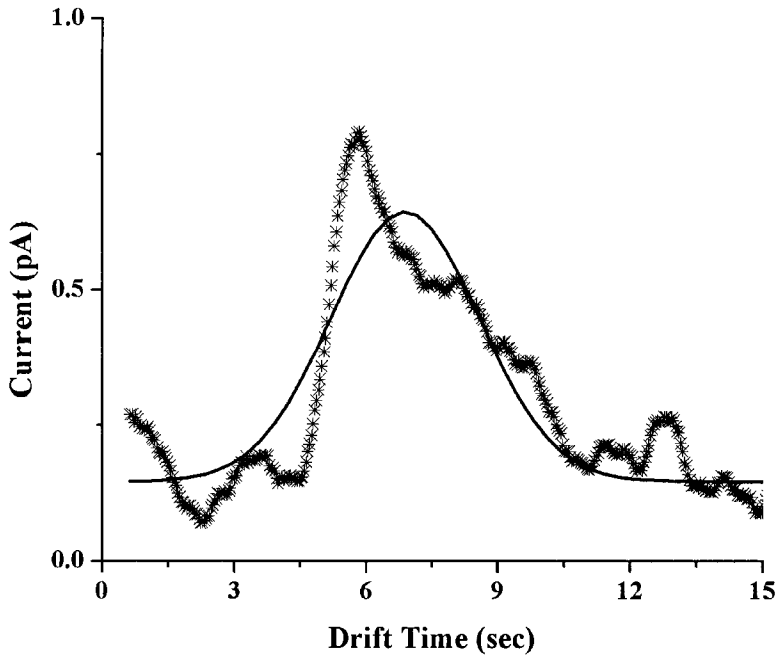


**Figure 5-15 A typical bad signal and a Gaussian fit rejected for data analysis.**

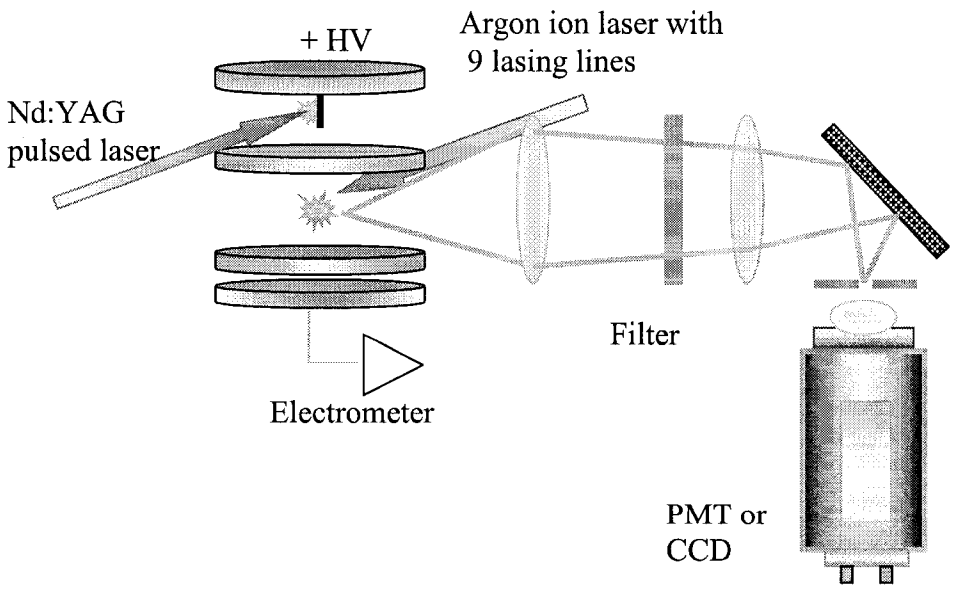


**Figure 5-16 A schematic diagram for measurement of the excitation spectrum.**

476 nm (190 mW), 488 nm (600 mW), 496 nm (230 mW), 502 nm (95 mW) and 514 nm (770 mW), were used separately to excite a single pulse of $10^7$-$10^8$ $Ba^+$ ions. A long pass color filter was used to reduce the stay light at the laser wavelength. The laser-induced fluorescence photons at all wavelengths greater than the cutoff wavelength of the filter were detected by a photomultiplier tube (PMT). The PMT was operated in the photon counting mode, and the signal was recorded by a multichannel analyzer. The PMT is a Burle 8852 tube, which has quantum efficiency (QE) of about 7% at 550 nm. The schematic diagram of the electronics for photon counting is shown in Fig. 5-17. The rate of detected photons versus the applied voltage on the PMT is plotted in Fig. 5-18. Since the dark count rate (signal with no light input) also increases with the applied voltage, a voltage of −1700 V to −1800 V gives the best signal-to-noise ratio. In our experiments,

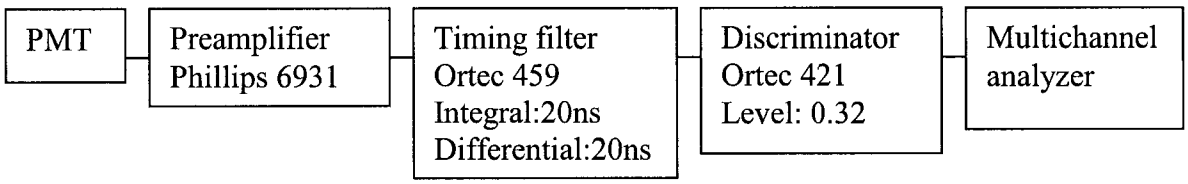


**Figure 5-17 Electronics used for photon counting system.**

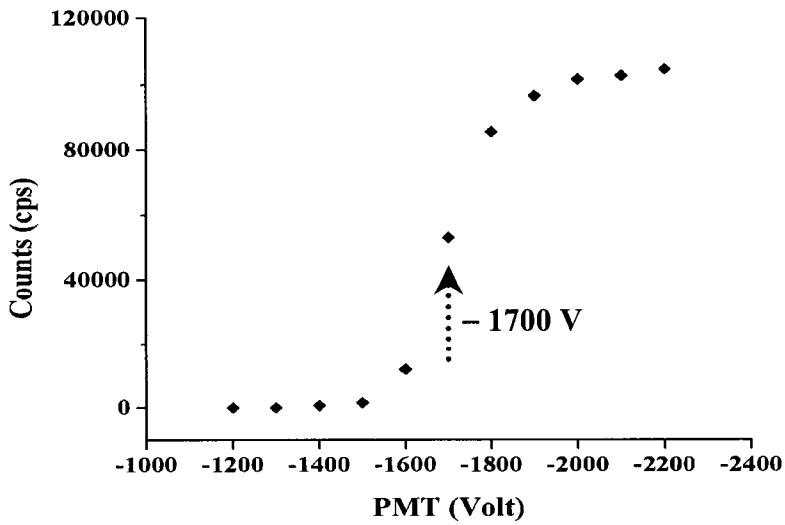


**Figure 5-18 Photon counts vs. PMT voltage. A sharp increase around – 1700 V is observed.**

−1700 V was usually used. The PMT was installed inside a $LN_2$-cooled housing purged with cold nitrogen gas. The temperature could go down to −30 °C, where there were only 25 counts per second of dark count background. A fluorescence signal of $Ba^+$ ions excited at 502 nm is shown in Fig. 5-19. In order to compare to the simultaneously recorded current signal, the time scale of emission signal was adjusted by a factor of 2 because $Ba^+$ ions were excited half way along the drift distance. A good correlation of the two signals was seen, indicating that the fluorescence was due to the moving $Ba^+$ ions. Background from plasma emission and residual particle scattering getting through the filter can be rejected by setting the proper time window. The excitation spectrum is then determined by measuring the number of emission photons as a function of the excitation wavelength.

In the fluorescence spectrum configuration shown in Fig. 5-20 (simplified figure), one argon ion lasing line was used, and the fluorescence spectrum was analyzed through a spectrometer. In the initial experiments, the detector on the spectrometer (Jarrell-Ash 82020) was a PMT, and narrow input and output slits of ~200 μm wide were used. The wavelength setting was scanned while the count rate was recorded in the multichannel analyzer. In our recent experiments, a $LN_2$-cooled CCD array detector (Roper scientific: Spec-10:400B) on a spectrometer (Acton: SpectroPro 300i) was used. The CCD detector consisted of an array of 1340×400 pixels, and each pixel was 20 μm ×20 μm. The dark count rate was down to 0.3 $e^-$/pixel/hour when it was cooled to −120 °C. The advantage of a CCD detector is that the whole emission spectrum can be obtained simultaneously for a single pulse of $Ba^+$ ions if the output slit is removed. The grating efficiency (GratingLab: 600/mm, 750nm blaze) for this spectrometer is shown in Fig. 5-21, where we have averaged the efficiency of S and P polarization [17]. The quantum efficiency of

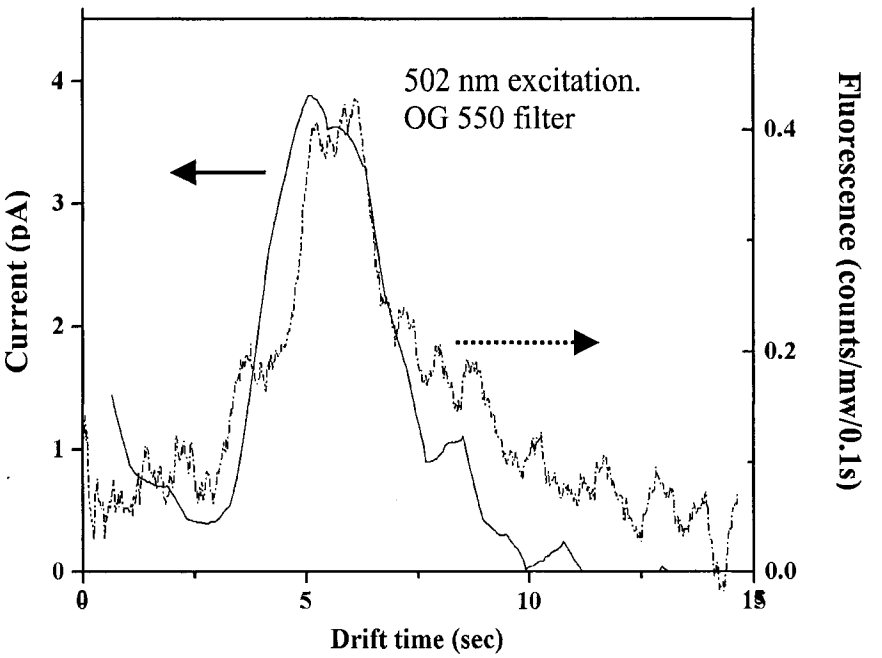


**Figure 5-19 Time correlation of the fluorescence (dot line) and ions drift (solid line) signals.**

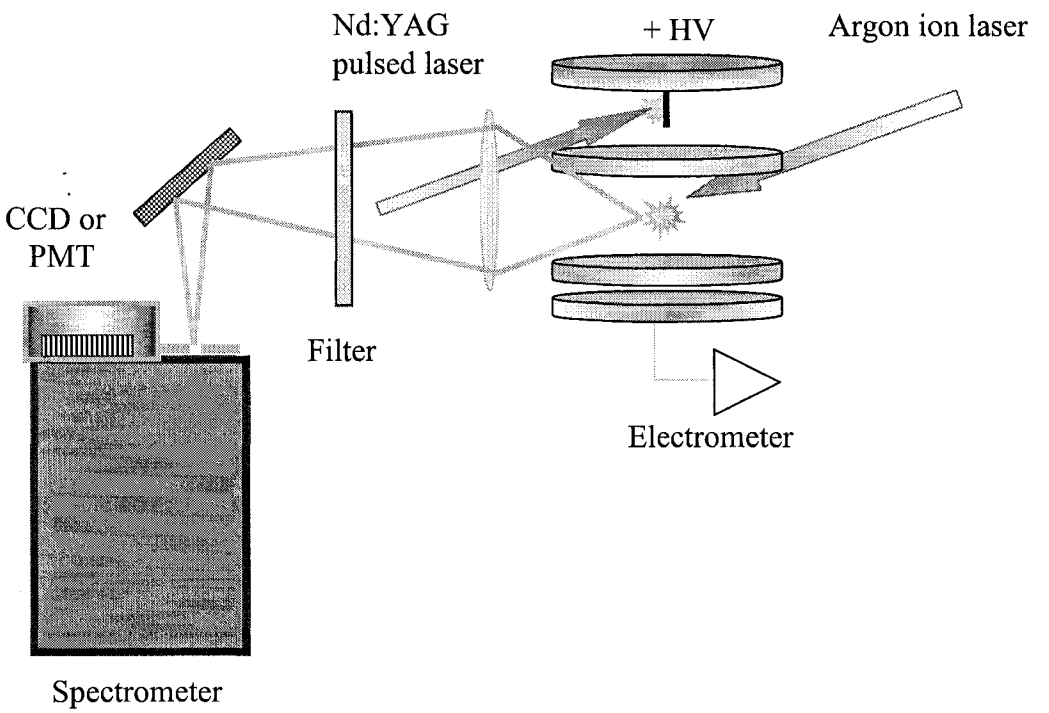


**Figure 5-20 Experimental setup for measuring the fluorescence spectrum.**

CCD detector as the function of wavelength is illustrated in Fig. 5-22 [18]. The final fluorescence spectra are normalized to these curves.

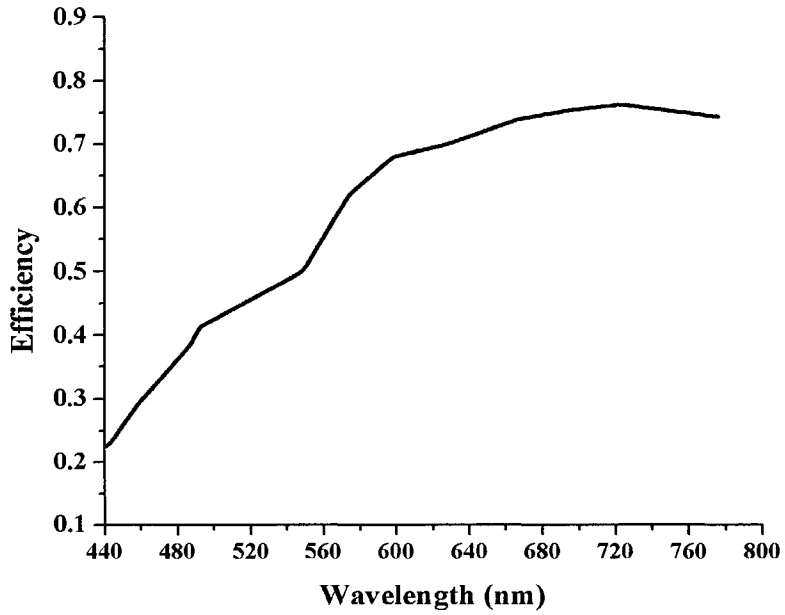


**Figure 5-21 Grating efficiency as a function of wavelength [17].**

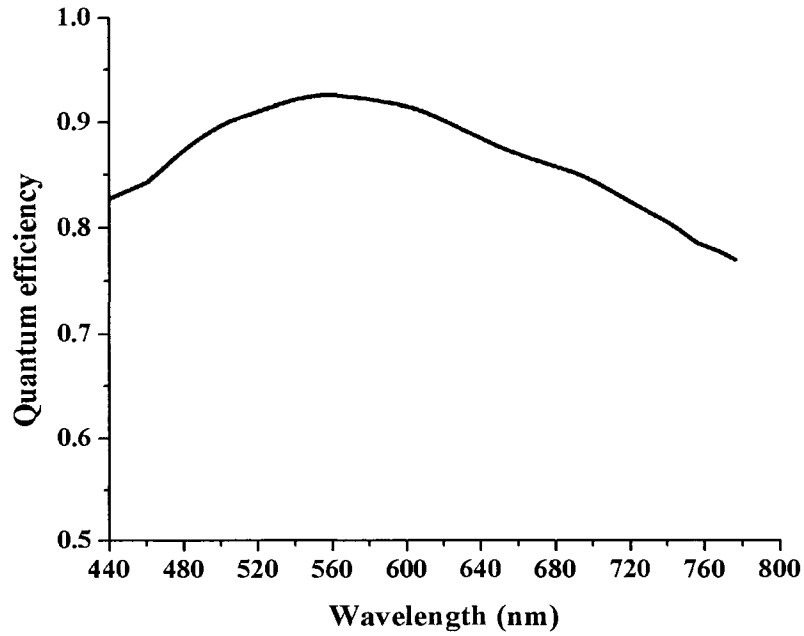


**Figure 5-22 Quantum efficiency of CCD detector as a function of wavelength [18].**

The experimental configuration for early work in taking $Ba^+$ cloud image is illustrated in Fig. 5-23. The electrode system has been magnified for purpose of illustration. In the initial experiment, two lenses were used inside and just outside the vacuum chamber in order to collect more fluorescence photons and to reduce the stray light by imaging on an aperture. Although a high collection efficiency was obtained, the image distortion and defocusing due to the limited depth of field were a concern in this configuration. When a blurred image was recorded on the CCD camera, it was not as easy to distinguish the possibility of residual particle scattering light from the fluorescence image of a $Ba^+$ cloud.

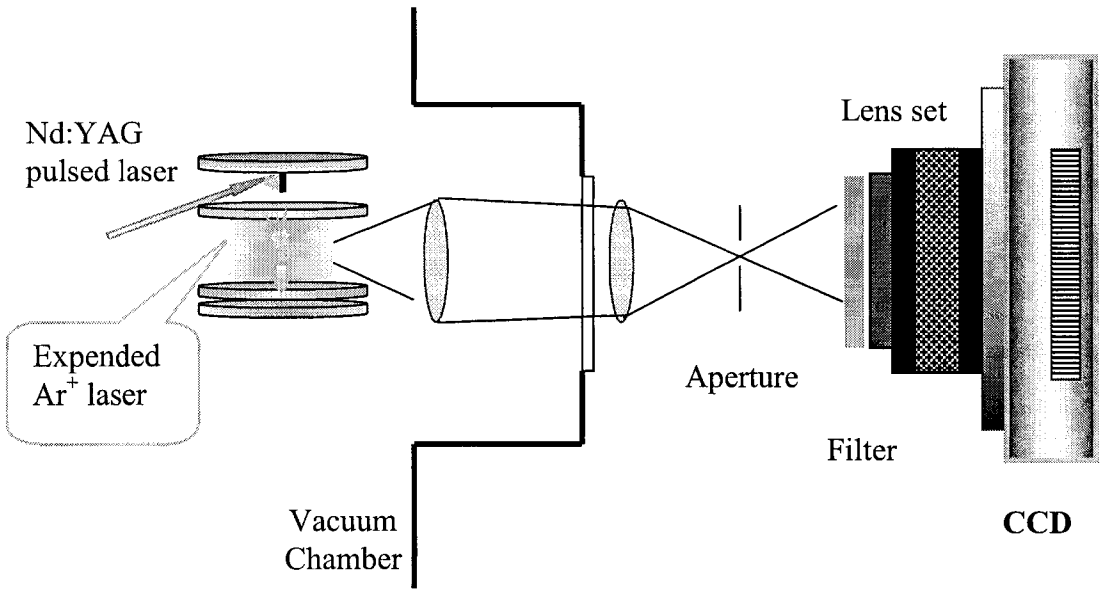


**Figure 5-23 Experimental setup for $Ba^+$ ion cloud image experiment. The lens in the vacuum chamber was used to obtain high collection efficiency.**

Therefore, a second configuration was used by sacrificing the collection efficiency as shown in Fig. 5-24. The CCD camera could look at the drift region of $Ba^+$ ions using one Nikon 50 mm lens and one Raman edge filter. We found that this

configuration had much superior imaging performance by using graph paper as a test source. The price paid was a loss of collection efficiency of a factor of 20 compared to the configuration of Fig. 5-23. The Raman edge filter can block the stay light by as high as $10^6$, and the CCD camera pixels can be chosen and binned at the region we are interested. Therefore, without the aperture, the scattering light could be reduced to an acceptable level. In this configuration, the residual scattering light from large ablated particles in LXe was observed and recorded as shown in Fig. 5-25. Each frame was taken with 400 ms exposure time, so the image was a line. The particle size was estimated as ≤200 μm. The expected $Ba^+$ ion fluorescence cloud is in the size of a few mm, so it can be distinguished from the residual particle scattering with the size ranging from tens of μm to hundreds of μm.

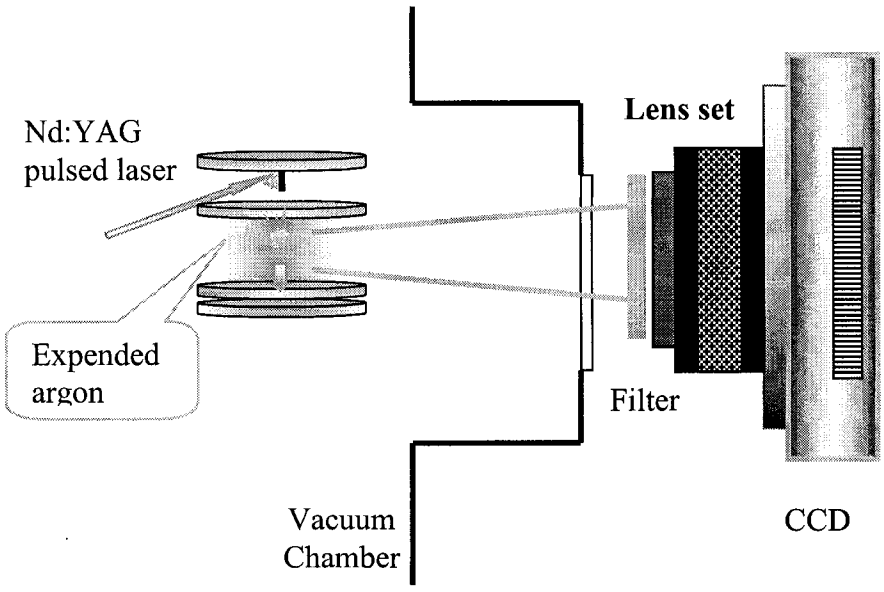


**Figure 5-24 Experimental setup for $Ba^+$ ions cloud image experiment by removing lens for better image quality.**

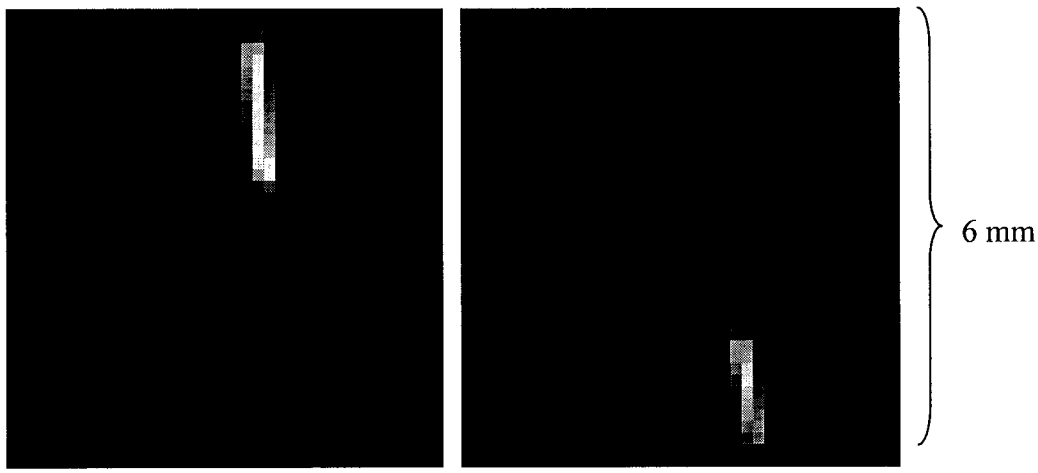


**Figure 5-25 Images of particles scattering in LXe. (a) 0.9 sec after laser ablation. (b) 1.8 sec after laser ablation. The particle size is about 200 μm.**

The three detection systems used for most of our measurements have different collection efficiency, optics loss and quantum efficiency of detector as summarized in Table 5-3. The collection efficiency of the configuration, Fig. 5-20, with an Acton SpectroPro 300i (f#/4) spectrometer, is given as

$$\varepsilon_{spec} \sim \frac{1}{256}\frac{sh}{A}, \qquad 5\text{-}9$$

where s is slit width (1 mm), h is the image height (~2 mm) on the slit and A is the area of laser excitation (~3 $mm^2$). The collection efficiency of the other two configurations, Fig. 5-16 and Fig. 5-23, is determined by the solid angle from the detection region to the first collecting lens. There is an extra light collection loss in the Fig. 5-23 because of the limited aperture size of the lens set (~3 cm in diameter). The fraction of ions in laser beam is estimated from the ratio of the laser beam diameter (~2 mm) and ion cloud diameter (~6 mm), so only about 11% of ions interact with the laser beam in Fig. 5-16 and Fig 5-20. It is assumed that each optics surface has about 4% reflection loss, and the

**Table 5-3 Detection efficiency for each fluorescence measurement system.**

| Configuration | Figure 5-16 Excitation | Figure 5-20 Fluorescence | Figure 5-23 Image |
|---|---|---|---|
| Collection eff. | 0.01 | 0.0026 | 0.005 |
| Fraction of ions in laser beam | 0.11 | 0.11 | 1 |
| Lens & window transmission | 0.61 | 0.61 | 0.66 |
| Quantum eff. | 0.035 (PMT) | 0.9 (CCD) | 0.9 (CCD) |
| Mirror reflection | | 0.8 | |
| Filter transmission | 0.65 (OG530) | 0.54 (notch filter) | 0.54 (notch filter) |
| Grating efficiency | | 0.5 | |
| Digitization factor (counts/$e^-$) | | 0.13 | 0.5 |
| **Total efficiency** | **$1.5\times10^{-5}$** | **$4.2\times10^{-6}$** | **$8.0\times10^{-4}$** |

reflection of mirror is 90 %, so the total transmission of lenses and windows are determined according to the numbers of optics used. The loss of the color filter for OG530 used in Fig. 5-16 is estimated as 35 % by comparing the transmission curve and the fluorescence spectrum shown in Fig. 7-9(d). The transmission of notch filter is estimated as 54 % according to its transmission (90%) and its clear size compared to the size of the collected light beam (60%). The quantum efficiency of PMT used in Fig. 5-15 is about 3.5% while operated at −1700V. The grating efficiency and CCD quantum efficiency used in Fig. 5-20 is about 50% and 90% respectively. Eight electrons are required to generate one count for the CCD detector operated in the low gain mode, and that is the source of the digitalization factor. The best choice for low signal detection is to set up the CCD in the high gain mode, where only two electrons are required to generate one count. The total detection efficiency is then determined as shown also in Table 5-3. The predicted fluorescence counts emitted by one $Ba^+$ ion per second in each detection system can be obtained according to Eq. 4-6 and will be compared to the experimental data in Chapter 7.

## 5-9 Optics for reducing stray light

For our goal to detect a single $Ba^+$ decay daughter in LXe, it is expected that the stray light count rate must be reduced to the $10^{-18}$ level compared to the input photon rate in the excitation laser. Stay light comes from Rayleigh-Brillouin scattering in liquid xenon, laser beam reflection on each optical surface, and any particle in the liquid. In each case, the wavelength of the scattered light is close to the laser wavelength. By using imaging optics with an aperture, it should be possible to reduce the stray light down to the $10^{-9}$ level or lower with careful arrangement. Additional reduction as much as $10^9$ may be needed from filters.

The traditional yellow, orange and red long pass color filters which absorb blue and green light and transmit the longer wavelength can attenuate stray laser light to the $10^{-5}$ level at wavelengths just below the cutoff [19]. More attenuation is possible if the laser wavelength is considerably below the cutoff wavelength. Unfortunately, we have found that a small amount of the absorbed light in color filters produces red-shifted fluorescence in the transmission band. Thus, without imaging, the effectiveness of a color filter is only $10^{-4}$, and multiple filters provide no advantage. The test results of some commercial color filters by using a CW Nd:YAG laser at 532 nm as the test laser is summarized in Table 5-4. The transmission with filter fluorescence or without filter fluorescence was measured by setting the detector close to or far from the filter. All other types of color filter tested had significantly higher fluorescence.

This level of filter fluorescence induced by laser stray light is probably too great for our experiment. Thus interference filters, which reflect rather than absorb, are attractive attenuators. Raman edge filters and notch filters (holographic or thin-film

coating) are sharp non-fluorescing attenuation filters, which have been used in our recent experiments. The typical transmission curves for a notch filter and Raman edge filter are illustrated in Fig. 5-26 [20].

**Table 5-4 Transmission of long pass color filter.**

| Color Filter | Transmission without Fluorescence | Transmission with fluorescence |
|---|---|---|
| OG 570 | $5\times10^{-8}$ | $7\times10^{-4}$ |
| OG 590 | $9\times10^{-7}$ | $2\times10^{-3}$ |
| RG 610 | ~0 | $3\times10^{-4}$ |
| RG 665 | ~0 | $2\times10^{-4}$ |

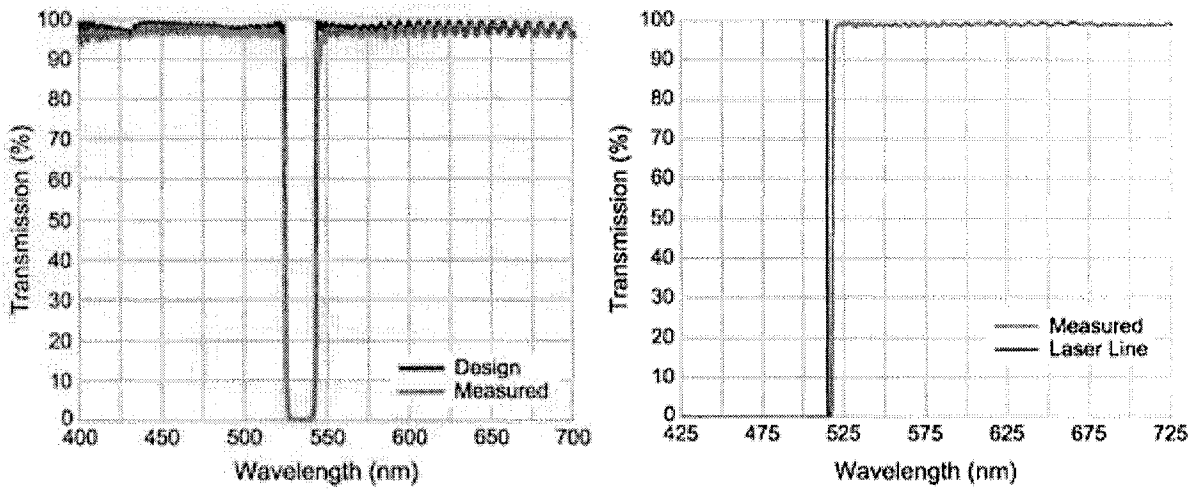


**Figure 5-26 The typical transmission curves for (a) notch filter and (b) Raman Edge filter [20].**

Holographic notch filters are manufactured by illuminating a dichromated gelatin film with two laser beams forming an interference pattern. They have been widely used for Raman spectroscopy [21-23]. The advantages of holographic notch filters are: high attenuation of Rayleigh line by > $10^6$ (>OD 6), narrow width (~10 nm) of the attenuation region, sharp spectral edges (<5nm), high transmission outside the band (>90%) and high

damage threshold (10 J/cm$^2$). With the recent advances in optical thin-films technologies driven by the challenging requirements of the telecom industry, a new type of filter has been developed in recent years. Based on the new technologies of ion-assisted ion-beam sputtering, non-quarter-wavelength-thick layers designs and optical monitoring algorithms and hardware, the new generation of thin-film filter, the Raman edge filter, has the features of steepest cutting edge, deep blocking in the attenuation region (OD >6), high transmission (> 98%) and highest reliability because of the hard dielectric coatings [20]. The wavelength of the rejection band for notch filter and cutoff wavelength for Raman edge filter can be tuned by adjusting the angle of the filter relative to the light according to the equation [20]

$$\lambda(\theta) = \lambda(\theta = 0°)\sqrt{1 - \frac{\sin^2\theta}{n_{eff}}}, \qquad 5\text{-}10$$

where $n_{eff}$ is the effective index of refraction in the filter. It has also been observed that the bandwidth and optical density decrease as the angle tuned away from normal incidence [20,21]. In summary, it might be possible to attenuate the stay light to the order of $10^{-18}$ by using two such filters without complicated imaging optics, and still have a very high fluorescence transmission rate >90%.

# References


1. C.C. Lim, Rev. Sci. Instrum. 57, 108 (1986).
2. Handbook of Chemistry and Physics, 67$^{th}$ edition, CRC press 1986.
3. E. Aprile et al., Nucl. Instr. and Meth. A 300, 343 (1991).
4. E. Buckley et al., Nucl. Instr. and Meth. A 275, 364 (1989).
5. M. Ichige et al., Nucl. Instr. and Meth. A 333, 255 (1993).
6. A.S. Barabash, I. Exp. Tech 31, 517 (1988).
7. Alfa Aesar, Ward Hill, MA 01835.
8. SAES Getters USA Inc., Colorado Spring, CO 80906.
9. W.I. Glaberson and W.W. Jonson, J. Low Temp. Phys. 20, 313 (1975).
10. H. Gunther, M. Foerste, M. Kunze, G. zu Putlitz and U. von Stein, Z. Phys. B. 101, 613 (1996).
11. Y. Moriwaki and N. Morita, Eur. Phys. J. D 13, 11 (2001).
12. O. Hilt and W.F. Schmidt, Chem. Phys. 183, 147 (1994).
13. A.J. Walters and L.W. Mitchell, J. Phys. D. 36, 1323 (2003).
14. K. Wamba, C. Hall and P. C. Rowson, SLAC, private communication.
15. O. Bunemann et al., Can. J. of Res. 27, 191 (1949).
16. Ion Source Software, Idaho Falls, ID 83403, U.S.A.
17. Grating Lab, now a part of Spectra-Physics, Mountain View, CA 94039.
18. Roper Scientific, Inc., Tucson, AZ 85706.
19. Long pass absorbing glass filter. Edmund Industrial Optics, Barrington, NJ 08007.
20. T. Erdogan and V. Mizrahi, Photonics Spectra, p 94, July 2003.
    Semrock Inc., www.semrock.com
21. J. Barbillat et al., J. Raman Spectrosc. 30, 745 (1999).
22. M.J. Pelletier and R.C. Reeder, Appl. Opt. 45, 765 (1991).
23. B. Yang et al., Appl. Spectrosc. 45, 1533 (1991).

# Chapter 6.

## Results and discussion
## Ionic mobility in liquid xenon

In this chapter we will present and discuss our mobility results for alkaline earth and $Tl^+$ ions in liquid xenon. Results for $Ba^+$ ion mobility in gaseous argon and xenon measured by the same technique will also be discussed. Since the theory of ion mobility in gas has been well known and verified experimentally, measuring ion mobility in gas is a good test for our measurement method. Early results of mobility measurements in the Fukui apparatus will be also given for comparison.

### 6-1 $Ba^+$ mobility in Ar and Xe gas

The transport properties of an ion in a gas are determined by the properties of collisions between the ion and the gas atom. Langevin suggested that the interaction is mainly dominated by an attractive force due to the polarization of the gas atom in the electric field of the ion. He obtained the following expression for the ionic mobility [1].

$$\mu_o = 0.5105\frac{Z}{n_g}\sqrt{\frac{\varepsilon_0(1+m_g/m_i)}{\alpha m_g}}, \qquad 6\text{-}1$$

where Z is the number of ionic charge, $m_i$ is the ion mass, $n_g$, $\alpha$ and $m_g$ are the number density, the dipole polarizability and the mass of the gas atom respectively. An excellent agreement of this theory with experimental results had been shown in previously work [2].

The sample ion current pulses for different applied voltages in xenon gas of 2 atm are shown in Fig. 6-1. The mobility is then determined by drift time, applied voltage on

target plate and $d_{eff}^2$ according to Eq. 5-2. The experimental results for $Ba^+$ mobility in xenon gas and argon gas are illustrated in Fig. 6-2 to Fig. 6-4. Note that no correction has been made for charge-induced motion of the gas and that the measured mobilities seem to be independent of voltage. The experimental results along with the theoretical predictions are summarized in Table 6-1. They agree with each other well even though only a statistical error is quoted in our results. The systematic error from the uncertainty of drift distance and ablation position is about 20% in this measurement.

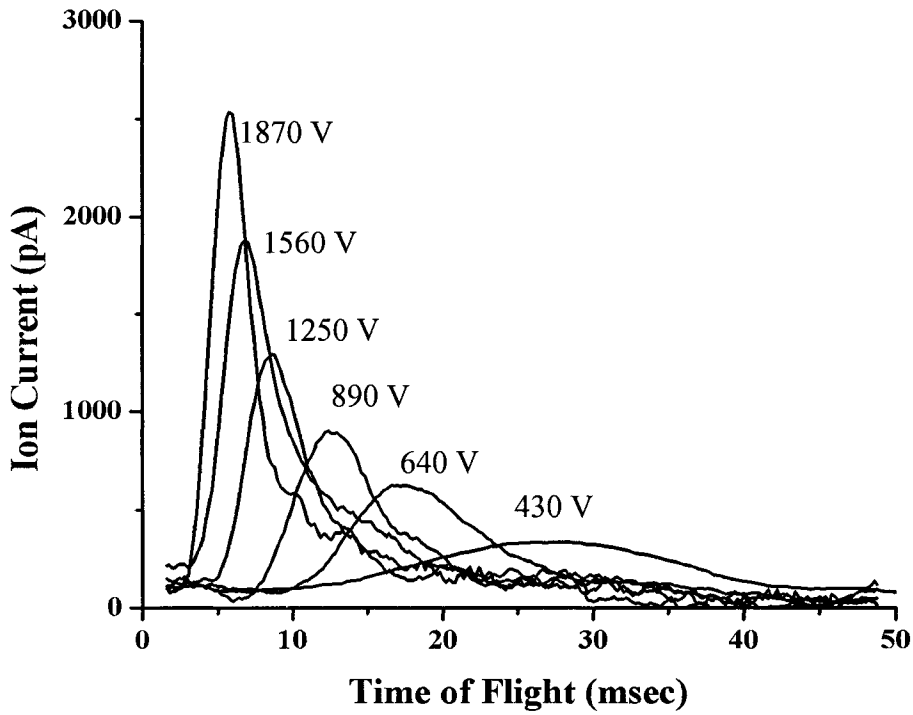


**Figure 6-1 Time of flight signal for $Ba^+$ in gaseous xenon at the pressure of 2 atm. The applied voltage is denoted as the target voltage.**

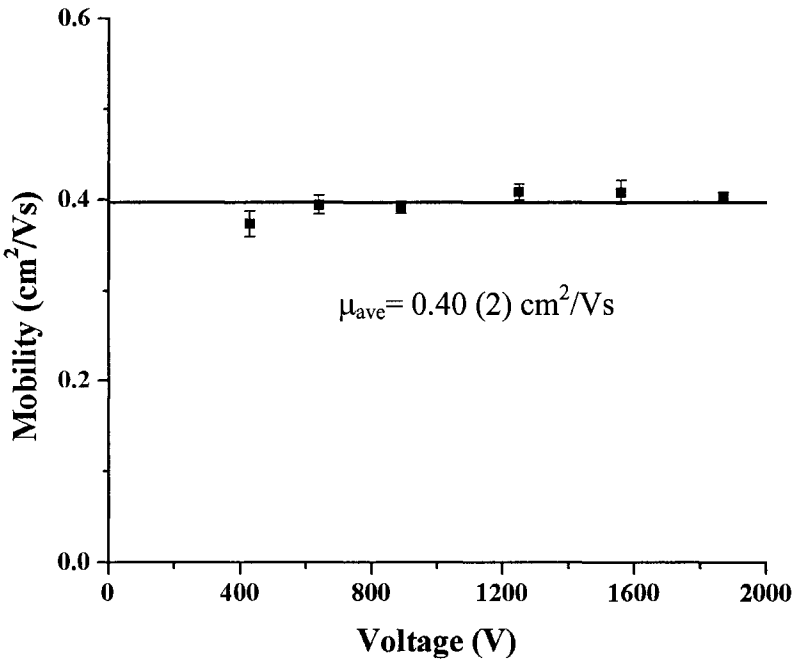


**Figure 6-2 Mobility of $Ba^+$ in gaseous xenon at the pressure of 2 atm. The E-field independent mobility is given as 0.40(2) $cm^2V^{-1}s^{-1}$.**

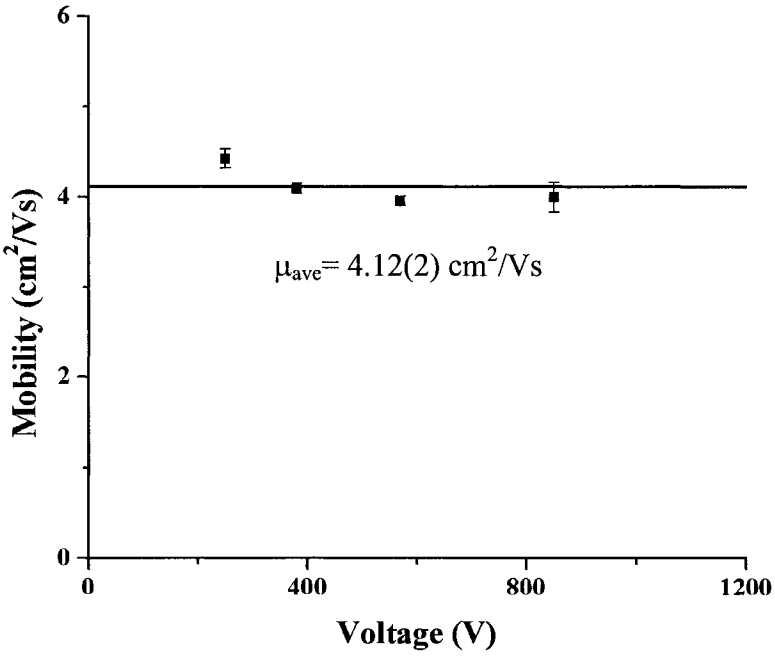


**Figure 6-3 Mobility of $Ba^+$ in gaseous xenon at the pressure of 0.27 atm. The E-field independent mobility is given as 4.12(2) $cm^2V^{-1}s^{-1}$.**

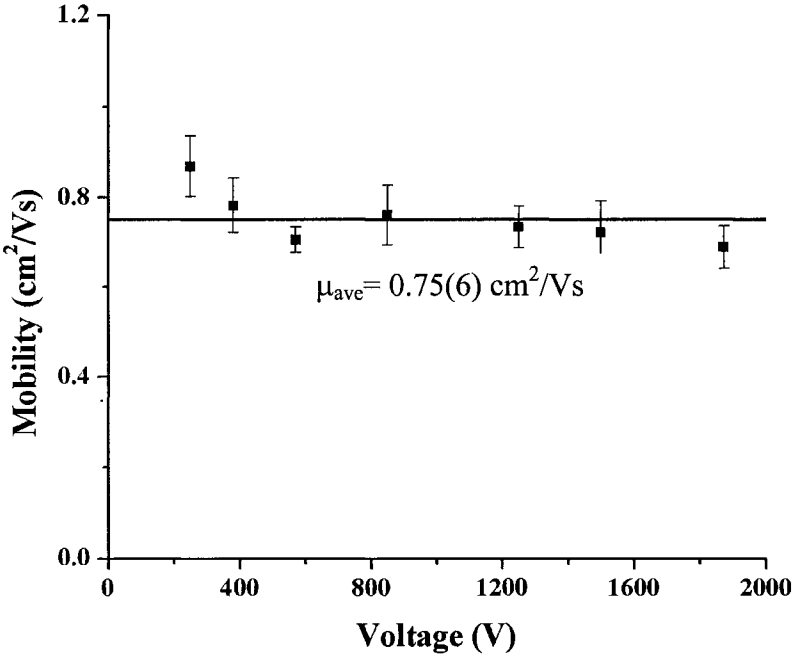


**Figure 6-4 Mobility of $Ba^+$ in gaseous argon at the pressure of 2 atm. The E-field independent mobility is given as 0.75(6) $cm^2V^{-1}s^{-1}$.**

**Table 6-1 Comparison of $Ba^+$ mobility in gas between this work and the theoretical predictions.**

| | Pressure (atm) | Mobility (this work) ($cm^2V^{-1}s^{-1}$) | Mobility (theory) ($cm^2V^{-1}s^{-1}$) |
|---|---|---|---|
| Xenon gas | 2 | 0.40(2) | 0.46 |
| | 0.27 | 4.12(2) | 3.37 |
| Argon gas | 2 | 0.75(6) | 1.05 |

## 6-2 $Ba^+$ mobility measurements in the Fukui system

Mobility measurements of $Ba^+$ were first made in the Fukui system filled with new xenon gas and detected by a fast response electrometer. The target was a Ba-Al getter, and the laser ablation was operated in liquid xenon. Much of the mobility data taken was noisy and not very useful due to the bubbling problem, and data was taken only for a small number of pulses. One of the typical pulses is shown in Fig. 6-5. Results

for mobility as a function of ion charge are shown in Fig. 6-6 for various applied voltages. As with the CSU data discussed below, some dependence on charge and electric field is seen in this data. There is not enough data to reach a firm conclusion, but a value of $Ba^+$ mobility in LXe around 0.00020 $cm^2V^{-1}s^{-1}$ is suggested. This is close to our CSU measurement result. Thus, although rough, this is an independent confirmation of the validity of the mobility measurement method.

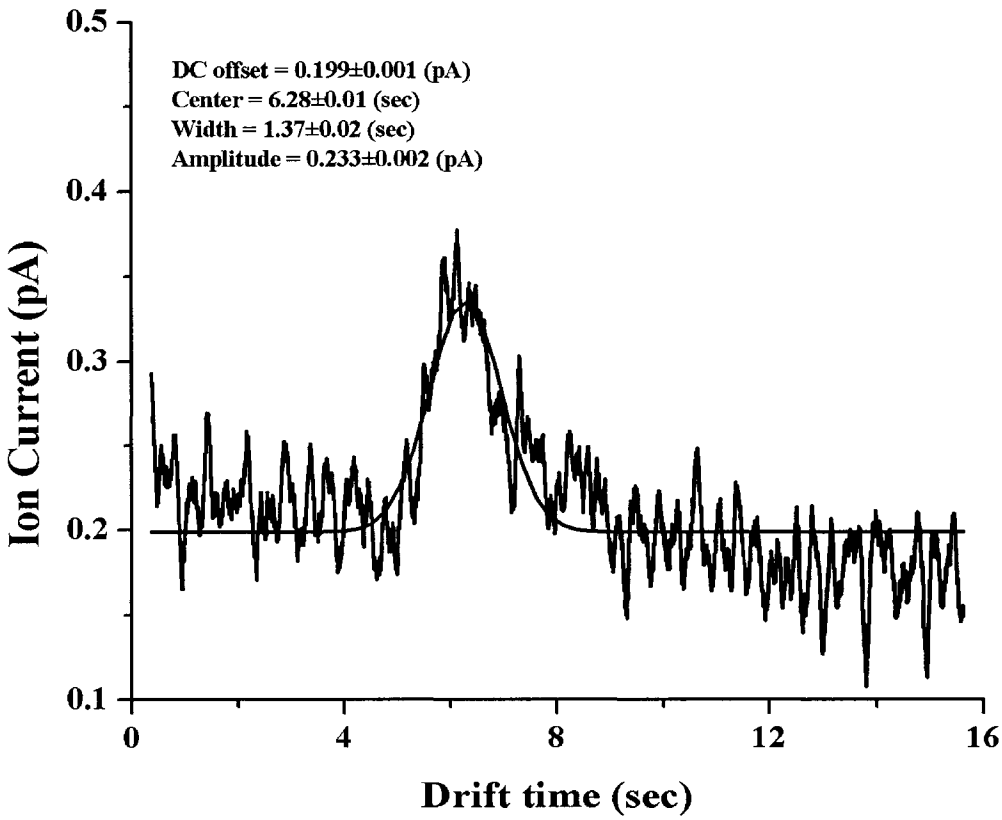


**Figure 6-5 Time of flight current signal for $Ba^+$ in liquid xenon, where E~ 900 V/cm and T ~ 170 K.**

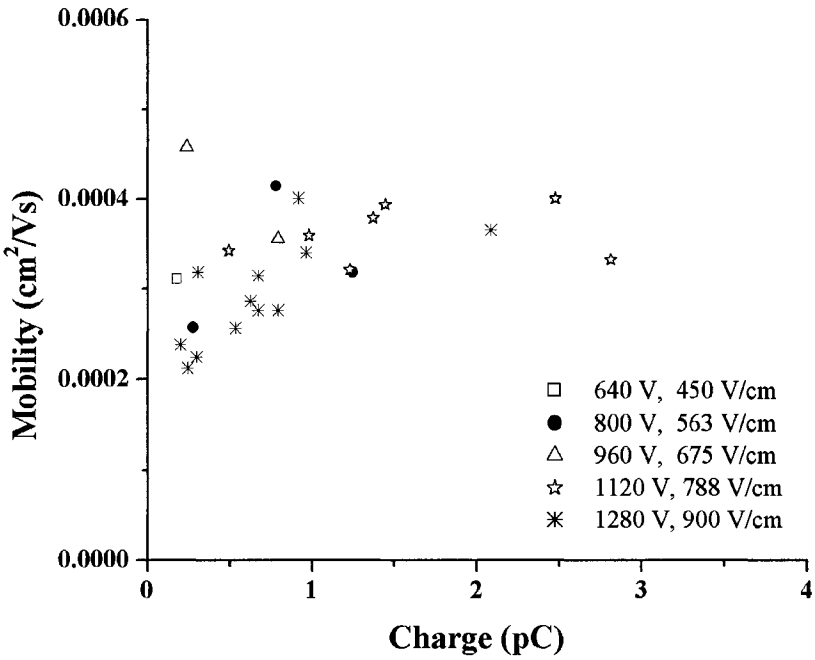


**Figure 6-6 Mobility of $Ba^+$ in liquid xenon at 170 K measured from Fukui's system.**

## 6-3 Ionic mobility results and corrections

The mobility of alkaline earth ions, $Ma^+$, $Ca^+$, $Sr^+$ and $Ba^+$, in liquid xenon was measured for the first time in this thesis. The mobility of $Tl^+$ was also measured in our system in order to compare our results to those obtained by a radioactive method.

As discussed in Chapter 5, every ion pulse was recorded by an electrometer and a digital oscilloscope. Thereafter, each current pulse was corrected by considering the time constant of the electrometer. A Gaussian function and a DC offset were used to fit the current signal. From this, the drift time $t_d$ and the total charge $Q$ were determined for each ion pulse. The apparent mobility can be calculated for each pulse by

$$\mu_{apparent} = \frac{V\int\frac{ds}{E}}{Vt_d} = \frac{d_{eff}^2}{Vt_d}, \qquad 6\text{-}2$$

where $V$ is the applied voltage on the acceleration plate. The $d_{eff}^2$ is calculated by using the SIMION 6.0 electric field simulation program, as discussed in Section 5-6.

Due to charge-induced fluid motion, the measured or "apparent" mobility is larger than the true mobility, and it depends on the total charge of the ion pulse. The mobility as a function of the ion charge $Q$ for one data set is plotted in Figure 6-7, where a linear fit is given for guiding the eyes. This graph shows that there is an increase in apparent mobility with increasing charge, and higher voltage gives smaller intercept and slope. These observations agree with our discussion in Section 3-3. Results for two more mobility data sets as a function of ion charge are shown in Fig. 6-8 and Fig. 6-9, and the same behavior is seen qualitatively.

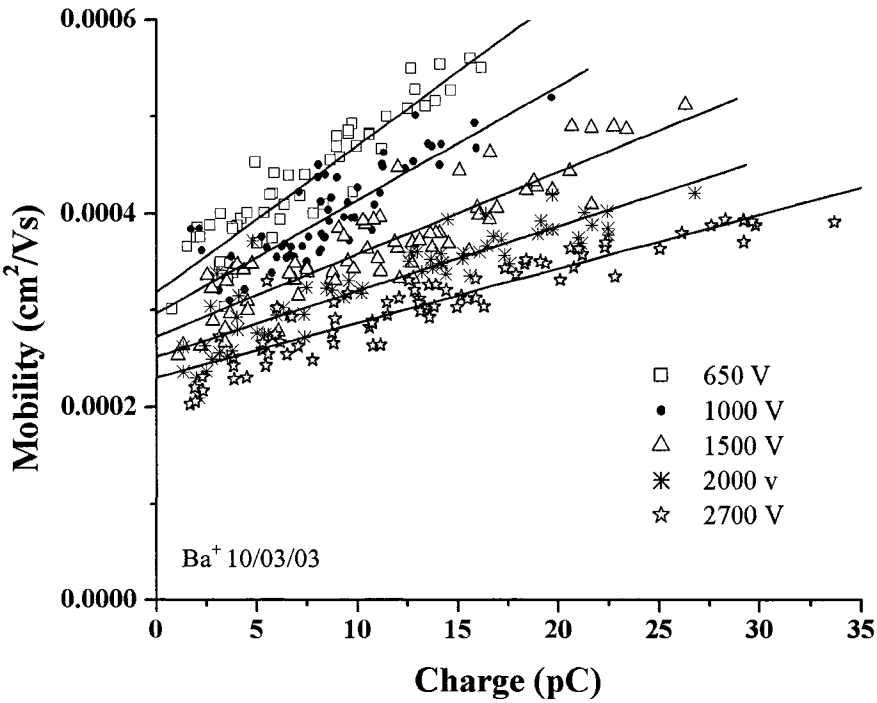


**Figure 6-7 $Ba^+$ mobility as a function of ion charge for various applied voltages. $d_{eff}^2$ =1.39 $cm^2$.**

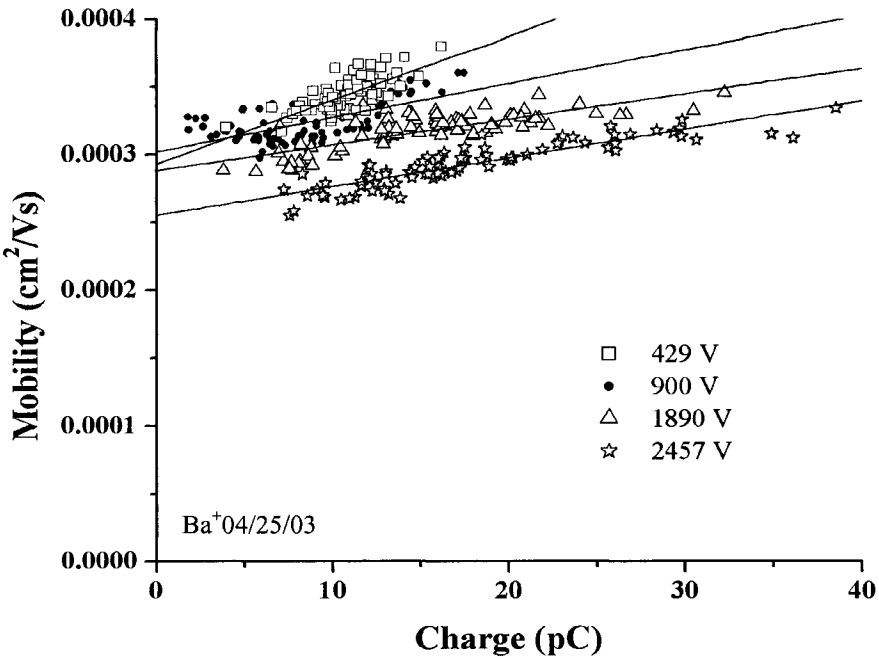


**Figure 6-8 $Ba^+$ mobility as a function of ion charge for various applied voltages. $d_{eff}^2$=0.58 $cm^2$.**

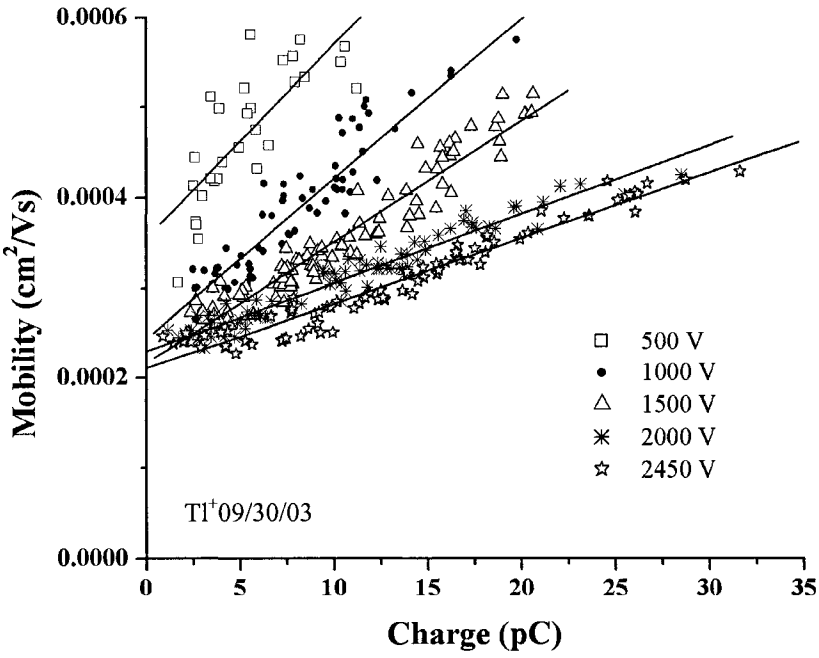


**Figure 6-9 $Tl^+$ mobility as a function of ion charge for various applied voltages. $d_{eff}^2$=1.39 $cm^2$.**

Clearly, it is necessary to determine the true mobility by some corrections, which take into account both the charge and the applied electric field. The required correction is thought to be due to fluid motion. A discussion of charge-induced fluid motion is given in section 3-3. From a simple energy conservation argument, the dependence of the apparent mobility on ion charge $Q$ is predicted to be

$$\mu_{appa.} = \mu_{true} + c\sqrt{Q}, \qquad 6\text{-}3$$

However, this simple notion is not quite correct because the ions partially lead the induced fluid flow, and there is also another force from the internal field of the ion cloud, which is proportional to $Q$. The latter effect does not average to zero because of the asymmetry of the liquid-gas interface. Thus another possible relationship is

$$\mu_{appa.} = \mu_{true} + cQ. \qquad 6\text{-}4$$

The constant $c$ in both equations is expected to be related to the drift field $E$. Since there is no clear theoretical model suggesting the proper correction procedure for $Q$ and $E$ effects, we have determined the best form by taking a large amount of data for various $Q$ and $E$ in each of the experimental configurations. More studies for $Q$ dependence were done by fitting all individual data with power of $Q$ dependence $n$, $Q^n$, and searching for the best $n$. The results are shown in Table 6-2, and the fitting results with $\Delta n/n<1$ are highlighted. The power of $Q$ dependence $n$ as a function of electric field $E$ at various drift distances is shown in Fig. 6-10, where only the data with $\Delta n/n<1$ are used. The linear fit gives

$$n=0.945(48)-0.0000889(235)E. \qquad 6\text{-}5$$

This n value will be used for the final correction. The results show no clear difference between $d_{eff}^2$ values. It is observed that the upper and lower limits for n could be set at 1

**Table 6-2 Complete experimental results for ionic mobility in LXe with Q dependence $Q^n$ fit. Errors are statistical only.**

| Date | Ion | $d_{eff}^2$ | $V_{accelerator}$ | E | μ | Δμ | n | Δn | Δμ/μ | Δn/n |
|---|---|---|---|---|---|---|---|---|---|---|
| | | ($cm^2$) | V | (cm/V) | ($cm^2V^{-1}s^{-1}$) | ($cm^2V^{-1}s^{-1}$) | | | | |
| **9/10/03** | **$Ba^+$** | **0.184** | **2600** | **3432** | **0.000198** | **1.00E-06** | **1.34** | **0.1** | **5.05E-03** | **0.0746** |
| **9/10/03** | **$Tl^+$** | **0.184** | **2000** | **2640** | **0.000221** | **1.00E-06** | **1.06** | **0.08** | **4.52E-03** | **0.0755** |
| **9/10/03** | **$Tl^+$** | **0.184** | **250** | **330** | **0.000252** | **2.00E-06** | **0.95** | **0.1** | **7.94E-03** | **0.1053** |
| **9/10/03** | **$Ba^+$** | **0.184** | **250** | **330** | **0.000271** | **2.00E-06** | **2.32** | **0.64** | **7.38E-03** | **0.2759** |
| **9/10/03** | **$Tl^+$** | **0.184** | **1000** | **1320** | **0.000167** | **2.80E-05** | **0.34** | **0.1** | **1.68E-01** | **0.2941** |
| **9/10/03** | **$Ba^+$** | **0.184** | **1000** | **1320** | **0.000239** | **1.10E-05** | **1.08** | **0.4** | **4.60E-02** | **0.3704** |
| **9/10/03** | **$Ba^+$** | **0.184** | **2000** | **2640** | **0.000186** | **2.20E-05** | **0.43** | **0.19** | **1.18E-01** | **0.4419** |
| 9/10/03 | $Tl^+$ | 0.184 | 2600 | 3432 | 0.029000 | 17.3 | -3E-04 | 0.2 | 5.97E+02 | 666.67 |
| **6/3/03** | **$Mg^+$** | **0.544** | **1350** | **1480** | **0.000280** | **1.10E-05** | **0.55** | **0.24** | **3.93E-02** | **0.4364** |
| **11/25/03** | **$Mg^+$** | **0.57** | **2400** | **2630** | **0.000229** | **1.10E-05** | **0.38** | **0.05** | **4.80E-02** | **0.1316** |
| **11/25/03** | **$Mg^+$** | **0.57** | **1040** | **1140** | **0.000305** | **1.10E-05** | **0.93** | **0.19** | **3.61E-02** | **0.2043** |
| **11/25/03** | **$Mg^+$** | **0.57** | **520** | **570** | **0.000318** | **8.00E-06** | **1.27** | **0.33** | **2.52E-02** | **0.2598** |
| **11/10/03** | **$Ca^+$** | **0.57** | **520** | **570** | **0.000301** | **2.50E-05** | **0.59** | **0.3** | **8.31E-02** | **0.5085** |
| **11/25/03** | **$Mg^+$** | **0.57** | **1500** | **1644** | **0.000259** | **5.20E-05** | **0.27** | **0.14** | **2.01E-01** | **0.5185** |
| 11/25/03 | $Mg^+$ | 0.57 | 2000 | 2192 | -0.000100 | 4.00E-04 | 0.07 | 0.07 | 4.00E+00 | 1 |
| 11/10/03 | $Ca^+$ | 0.57 | 2600 | 2850 | -0.000100 | 4.00E-04 | 0.079 | 0.083 | 4.00E+00 | 1.0506 |
| 11/10/03 | $Ca^+$ | 0.57 | 2400 | 2630 | -0.005700 | 0.07 | 0.0054 | 0.064 | 1.23E+01 | 11.852 |
| 11/10/03 | $Ca^+$ | 0.57 | 1040 | 1140 | -0.025000 | 2.3 | 0.0017 | 0.15 | 9.20E+01 | 88.235 |
| 11/10/03 | $Ca^+$ | 0.57 | 1500 | 1644 | -0.030000 | 3.3 | 0.0014 | 0.15 | 1.10E+02 | 107.14 |
| 11/10/03 | $Ca^+$ | 0.57 | 2000 | 2192 | -0.046000 | 5.7 | 0.0006 | 0.08 | 1.24E+02 | 133.33 |
| **8/20/03** | **$Tl^+$** | **0.575** | **2300** | **2498** | **0.000217** | **3.00E-06** | **0.699** | **0.053** | **1.38E-02** | **0.0758** |
| **4/11/03** | **$Ca^+$** | **0.575** | **429** | **470** | **0.000345** | **1.00E-06** | **3.01** | **0.25** | **2.90E-03** | **0.0831** |
| **5/6/03** | **$Ba^+$** | **0.575** | **1350** | **1480** | **0.000262** | **4.00E-06** | **0.98** | **0.13** | **1.53E-02** | **0.1327** |
| **4/25/03** | **$Ba^+$** | **0.575** | **900** | **986** | **0.000297** | **2.00E-06** | **3.52** | **0.65** | **6.73E-03** | **0.1847** |
| **8/20/03** | **$Tl^+$** | **0.575** | **450** | **489** | **0.000298** | **6.00E-06** | **2.3** | **0.47** | **2.01E-02** | **0.2043** |
| **4/11/03** | **$Ca^+$** | **0.575** | **600** | **658** | **0.000295** | **1.30E-05** | **0.5** | **0.12** | **4.41E-02** | **0.24** |
| **5/5/03** | **$Ba^+$** | **0.575** | **1950** | **2137** | **0.000248** | **1.30E-05** | **0.82** | **0.26** | **5.24E-02** | **0.3171** |
| **5/6/03** | **$Ba^+$** | **0.575** | **900** | **986** | **0.000278** | **9.00E-06** | **1.63** | **0.57** | **3.24E-02** | **0.3497** |
| **4/25/03** | **$Ba^+$** | **0.575** | **429** | **470** | **0.000300** | **9.00E-06** | **2.09** | **0.74** | **3.00E-02** | **0.3541** |
| 4/11/03 | $Ca^+$ | 0.575 | 2457 | 2693 | 0.000275 | 4.40E-05 | 0.33 | 0.34 | 1.60E-01 | 1.0303 |
| 4/25/03 | $Ba^+$ | 0.575 | 2457 | 2693 | 0.000070 | 0.00026 | 0.18 | 0.22 | 3.71E+00 | 1.2222 |
| 8/20/03 | $Tl^+$ | 0.575 | 2000 | 2192 | -0.000860 | 3304 | 0.033 | 0.094 | 3.84E+06 | 2.8485 |
| 4/25/03 | $Ba^+$ | 0.575 | 1890 | 2071 | -0.001400 | 0.033 | 0.015 | 0.29 | 2.36E+01 | 19.333 |
| 5/5/03 | $Ba^+$ | 0.575 | 429 | 470 | -0.015000 | 0.95 | 0.006 | 0.36 | 6.33E+01 | 60 |
| 4/11/03 | $Ca^+$ | 0.575 | 1350 | 1480 | -0.004300 | 0.33 | 0.006 | 0.4 | 7.67E+01 | 66.667 |
| 4/11/03 | $Ca^+$ | 0.575 | 1890 | 2071 | -0.000800 | 0.13 | 0.007 | 0.8 | 1.63E+02 | 114.29 |
| 5/6/03 | $Ba^+$ | 0.575 | 429 | 470 | -0.010000 | 1.59 | 0.006 | 0.866 | 1.59E+02 | 144.33 |
| 4/11/03 | $Ca^+$ | 0.575 | 900 | 986 | -0.004600 | 1.3 | 0.002 | 0.6 | 2.83E+02 | 300 |
| 5/5/03 | $Ba^+$ | 0.575 | 1350 | 1480 | 0.000312 | 0.00629 | -0.07 | 40 | 2.02E+01 | 571.43 |
| 8/20/03 | $Tl^+$ | 0.575 | 1350 | 1480 | -0.038000 | 3.98 | 0.0009 | 96675 | 1.05E+02 | 1E+08 |
| **4/11/03** | **$Ca^+$** | **0.61** | **1350** | **1480** | **0.000325** | **6.00E-06** | **1.93** | **1.3** | **1.85E-02** | **0.6736** |
| **9/30/03** | **$Tl^+$** | **1.39** | **2450** | **1811** | **0.000228** | **5.00E-06** | **1.29** | **0.08** | **2.19E-02** | **0.062** |
| **9/30/03** | **$Tl^+$** | **1.39** | **1500** | **1108** | **0.000255** | **8.00E-06** | **1.46** | **0.12** | **3.14E-02** | **0.0822** |

**Table 6-2 Complete experimental results for ionic mobility in LXe with Q dependence $Q^n$ fit. Errors are statistical only. (continued from last page)**

| Date | Ion | $d^2_{eff}$ | $V_{accelerator}$ | E | μ | Δμ | n | Δn | Δμ/μ | Δn/n |
|---|---|---|---|---|---|---|---|---|---|---|
| | | ($cm^2$) | V | (cm/V) | ($cm^2$/Vs) | ($cm^2$/Vs | | | | |
| 9/30/03 | $Tl^+$ | 1.39 | 2000 | 1478 | 0.000228 | 7.00E-06 | 0.97 | 0.09 | 3.07E-02 | 0.0928 |
| 9/30/03 | $Tl^+$ | 1.39 | 1000 | 739 | 0.000207 | 3.30E-05 | 0.8 | 0.14 | 1.59E-01 | 0.175 |
| 10/3/03 | $Ba^+$ | 1.39 | 1500 | 1108 | 0.000281 | 1.40E-05 | 1.12 | 0.2 | 4.98E-02 | 0.1786 |
| 10/3/03 | $Ba^+$ | 1.39 | 650 | 480 | 0.000312 | 2.00E-05 | 0.94 | 0.17 | 6.41E-02 | 0.1809 |
| 10/3/03 | $Ba^+$ | 1.39 | 2700 | 1995 | 0.000176 | 2.50E-05 | 0.55 | 0.11 | 1.42E-01 | 0.2 |
| 10/3/03 | $Ba^+$ | 1.39 | 1000 | 739 | 0.000321 | 1.60E-05 | 1.37 | 0.29 | 4.98E-02 | 0.2117 |
| 10/3/03 | $Ba^+$ | 1.39 | 2000 | 1478 | 0.000193 | 4.30E-05 | 0.5 | 0.18 | 2.23E-01 | 0.36 |
| 9/30/03 | $Tl^+$ | 1.39 | 500 | 370 | -0.070000 | 21 | 0.002 | 0.49 | 3.00E+02 | 245 |
| 5/9/02 | $Ba^+$ | 1.46 | 1350 | 791 | 0.000143 | 1.90E-05 | 0.56 | 0.09 | 0.132867 | 0.1607 |
| 8/29/02 | $Ba^+$ | 1.5 | 1600 | 1120 | 0.000121 | 7.50E-05 | 0.56 | 0.17 | 0.619835 | 0.3036 |
| 8/18/02 | $Ba^+$ | 1.5 | 1600 | 1120 | 0.000160 | 5.00E-05 | 0.57 | 0.19 | 0.3125 | 0.3333 |
| 9/1/02 | $Ba^+$ | 1.5 | 1600 | 1120 | 0.000132 | 9.30E-04 | 0.48 | 0.18 | 7.045455 | 0.375 |
| 9/30/03 | $Tl^+$ | 1.39 | 1000 | 739 | 0.000207 | 3.30E-05 | 0.8 | 0.14 | 1.59E-01 | 0.175 |

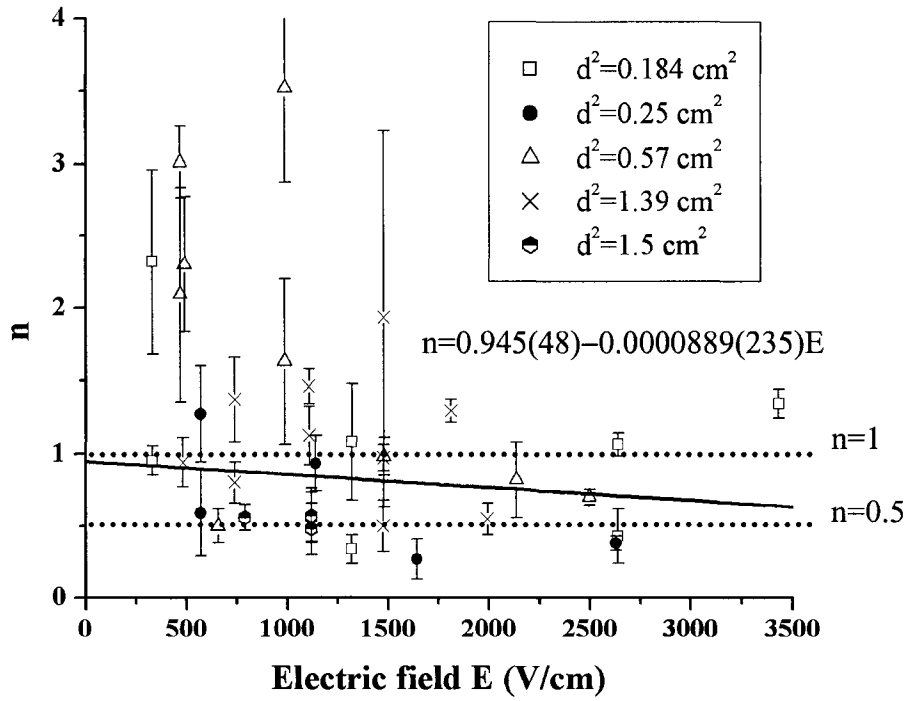


**Figure 6-10 Power of *Q* dependence n as a function of electric field *E* for 5 different $d^2_{eff}$.**

and 0.5, respectively. Although there is a lot of scatter in the results, the data are probably consistent in the range of $0.5 \leq n \leq 1$. It might be good to set n=1 for the first trial to correct our measured data and to analyze the properties of fluid motion.

Since from Fig. 6-7 to Fig. 6-9 suggest an inverse relationship between $\mu_{appa}$ and $E$, a more convenient expression is to divide up the two contributions to ion velocity, the true mobility part $\mu E$, and the induced fluid motion part $v_{fluid}$

$$v = \mu_{appa.} E + v_{fluid} \quad . \qquad 6\text{-}6$$

A typical example of a v vs. $E$ plot for various charge groups is shown in Fig. 6-11(a). In this case the plots of v vs. $E$ appear to be linear. The slope, which should be $\mu$ according to Eq. 6-6, is still $Q$-dependent. The nonzero intercept shows the existence of a small residual fluid flow in the absence of $E$ and $Q$. The true mobility is then determined by plotting the slope versus ion charge and extrapolating to zero charge as shown in Fig 6-11(b). A linear fit gives $\mu(Q=0)$=0.000186(2) $cm^2V^{-1}s^{-1}$, and a slope of 0.00000281(12) $cm^2$/Vs/pC. In Fig. 6-11(c), the residual fluid flow is plotted as a function of charge, yielding an intercept of 0.0333(6) cm/s and a slope of –0.000357(71) cm/s/pC. The same analysis has been applied to most of our data. One more example is shown in Fig. 6-12. In this case, the residual fluid flow increases with the ion charge $Q$. Other runs show essentially no $Q$ dependence on the $E$-independent part of the residual fluid flow.

In order to accomplish the separate fits like Fig. 6-11 and Fig. 6-12 more conveniently and reliably, the following global function discussed in Section 3-3 was used to do a least-squares fit to each complete data set,

$$v = a_0 + \frac{dIntercept}{dQ} Q + (\mu_{true} + \frac{d\mu}{dQ} Q)E \equiv a_0 + a_1 Q + (b_0 + b_1 Q)E \qquad 6\text{-}7$$

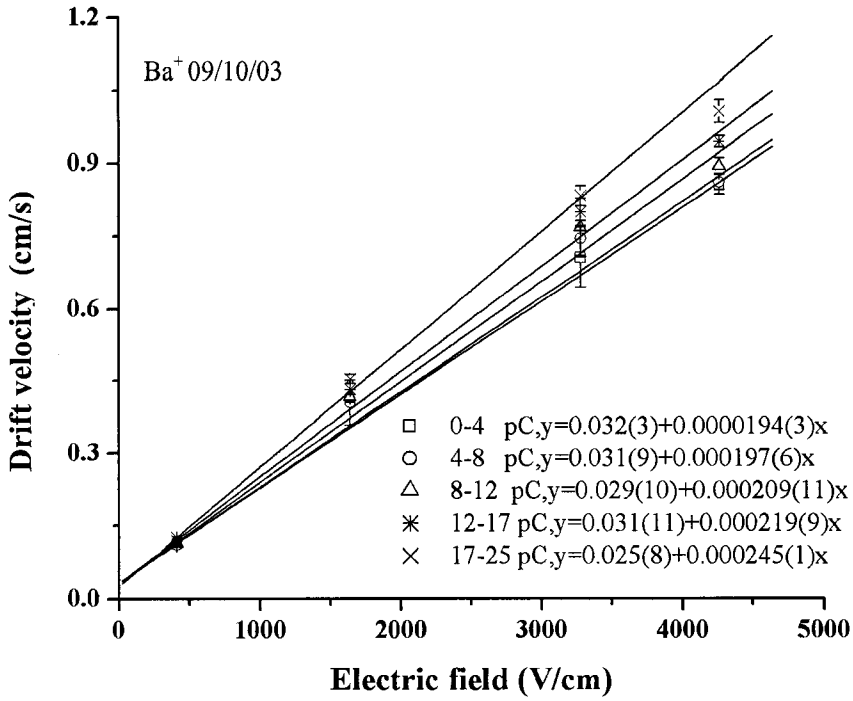


**Figure 6-11(a) v vs. *E* for various charge group. The slope defines the mobility, and the nonzero intercept gives the residual fluid flow.**

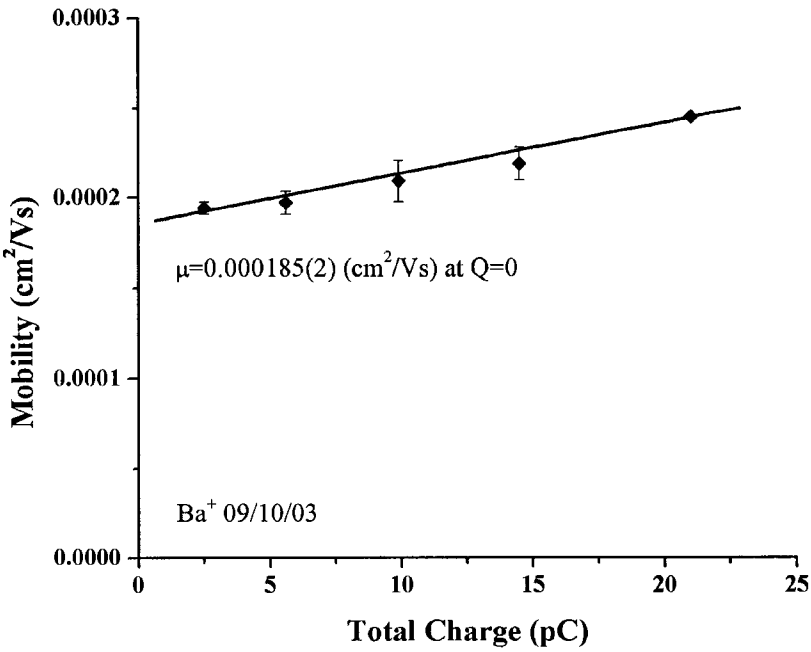


**Figure 6-11(b) $Ba^+$ mobility as a function of ion charge. The intercept with zero charge is the true mobility.**

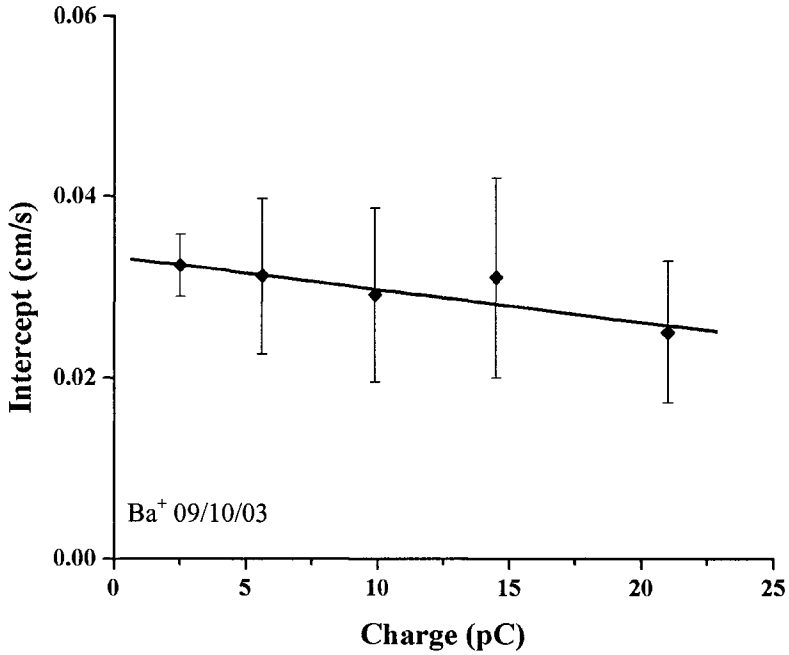


**Figure 6-11(c) Residual fluid flow as a function of charge.**

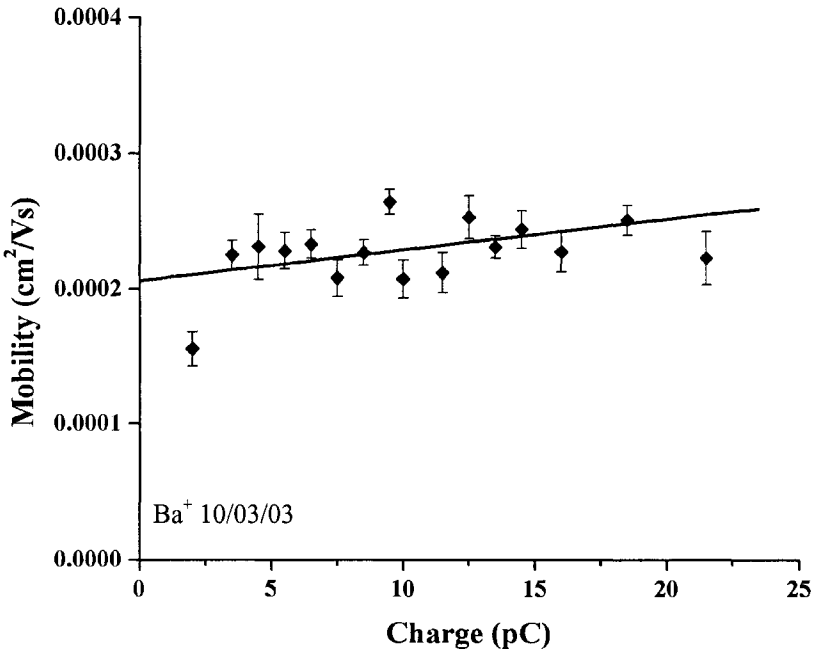


**Figure 6-12(a) $Ba^+$ mobility as a function of ions charge. The intercept is 0.000206(7) $cm^2V^{-1}s^{-1}$, and the slope is 0.00000288(63) $cm^2/Vs/pC$.**

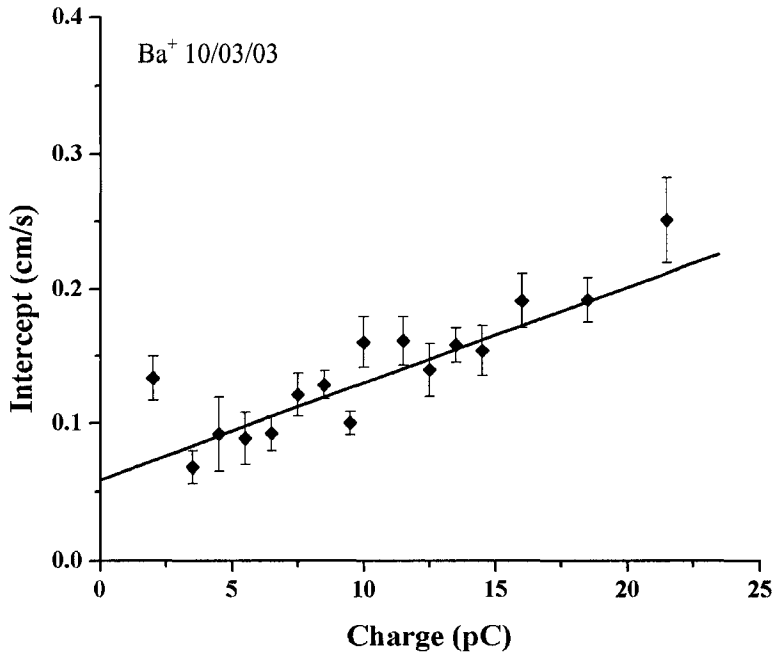


**Figure 6-12(b) Residual fluid flow as a function of charge. The intercept is 0.0581(89) cm/s, and the slope is 0.00719(86) cm/s/pC.**

Here v $= \mu_{appa.} E$ is the drift velocity, $a_0+a_1Q$ represents the residual fluid flow and $(b_0+b_1Q)E$ is the charged-induced fluid motion. The coefficient $b_0$ gives the true ion mobility. $E$ is the time-averaged electric field along the path at low $Q$. Since $dt = \frac{dx}{\mu E}$

$$E = \frac{\int E dt}{\int dt} = \frac{\int dx}{\int \frac{dx}{E}} = \frac{V_{accelerator}}{d_{eff}^2} d_{drift}, \qquad 6\text{-}8$$

where the drift distance $d_{drift}$ is defined from the liquid level (accelerator plate) to the center of the Frisch grid-collector region. Table 6-3 gives the comparison between the results from the former analysis (call it separate fit) and the global fit for four runs. The results agree with each other very well especially for the parameter of interest, $b_0$.

**Table 6-3 Comparison between the individual fitting and the global fitting.**

| | $Ba^+$ | | $Ba^+$ | |
|---|---|---|---|---|
| Date | 9/10/03 | | 10/3/03 | |
| Fitting | Global | Separate | Global | Separate |
| $a_0$ | 0.0281(19) | 0.0333(6) | 0.0542(17) | 0.0581(89) |
| $a_1$ | 0.00116(14) | –0.000357(71) | 0.00835(13) | 0.00719(86) |
| **$b_0$** | **0.000191(8)** | **0.000185(2)** | **0.000211(13)** | **0.000206(7)** |
| $b_1$ | 0.00000159(6) | 0.00000281(12) | 0.00000121(9) | 0.00000228(63) |
| | | | | |
| | $Tl^+$ | | $Tl^+$ | |
| Date | 9/10/03 | | 9/30/03 | |
| Fitting | Global | Separate | Global | Separate |
| $a_0$ | 0.0253(13) | 0.0211(40) | 0.0311(12) | 0.0361(55) |
| $a_1$ | 0.000877(106) | 0.000752(258) | 0.0143(1) | 0.0141(7) |
| **$b_0$** | **0.000198(1)** | **0.000197(1)** | **0.000198(1)** | **0.000204(4)** |
| $b_1$ | 0.00000161(5) | 0.00000158(13) | –0.000000966(68) | –0.00000174(52) |

The last trial for fluid motion correction is using $Q^n$ as the charge dependence. The experimental results for the mobility of $Ca^+$, $Mg^+$, $Sr^+$, $Ba^+$ and $Tl^+$ by global fit,

$$v=a_0+a_1Q^n+(b_0+b_1Q^n)E, \qquad 6\text{-}9$$

are summarized in Table 6-4, where the power of $Q$ dependence n is applied by three values, 1, 0.5 and from Eq. 6-5 (call it fit-n). Mobility results for those ions with 3 different fits are also plotted in Fig. 6-13. It shows that most of the mobility has the biggest and smallest values by fit with n=1 and n=0.5 respectively, and the $Q^n$ fit with n given by Eq. 6-5 gives the best result with minimum statistical error. These ions also have the similar mobility within a factor of 2. The plots of $a_0$, $a_1$, $b_0$, and $b_1$ versus $d_{drift}$ for all ions with n=1 are also shown in Fig. 6-14. Only the parameter $a_1$ (Fig. 6-14(b)) has a clear dependence on drift distance. It indicates that the *d(residual fluid flow)/dQ* increases with drift distance. It is observed that the measured mobility at various

**Table 6-4 Summary of parameters of alkaline earth ions and $Tl^+$ in LXe by global fit with Q, $Q^n$, and $Q^{0.5}$ dependence.**

| Fit | Date | $d_{eff}^2$ ($cm^2$) | d (mm) | Q $a_0$ | $Q^n$ $a_0$ | $Q^{0.5}$ $a_0$ | Q $a_1$ | $Q^n$ $a_1$ | $Q^{0.5}$ $a_1$ |
|---|---|---|---|---|---|---|---|---|---|
| $Mg^+$ | 4/3/03 | 0.58 | 6.3 | 0.00720(198) | 0.0139(20) | 0.0086(20) | −0.00217(17) | −0.00563(26) | −0.00743(61) |
| | 11/25/03 | 0.57 | 6.3 | 0.0497(19) | 0.0788(16) | 0.0406(17) | 0.00275(11) | −0.00275(19) | 0.0118(5) |
| $Ca^+$ | 4/11/03 | 0.58 | 6.3 | 0.0190(8) | 0.0288(8) | 0.0063(8) | 0.00164(6) | −0.00013(10) | 0.00945(24) |
| | 11/14/03 | 0.57 | 6.3 | 0.0369(25) | 0.0693(22) | 0.0109(22) | 0.00663(15) | 0.00140(29) | 0.0305(6) |
| $Sr^+$ | 11/26/03 | 0.57 | 6.3 | 0.0420(29) | 0.0759(27) | 0.0421(27) | 0.00176(18) | −0.00467(32) | −0.00577(77) |
| $Ba^+$ | 4/25/03 | 0.58 | 6.3 | 0.0123(13) | 0.0814(11) | 0.0230(14) | 0.00333(9) | −0.00589(15) | −0.00786(37) |
| | 5/5-6/2003 | 0.58 | 6.3 | 0.0290(6) | 0.0309(6) | 0.0143(6) | 0.00262(4) | 0.00228(7) | 0.0132(2) |
| | 9/10/03 | 0.184 | 3 | 0.0281(19) | 0.0490(17) | 0.0114(20) | 0.00116(14) | −0.00367(23) | 0.00909(61) |
| | 10/3/03 | 1.39 | 10.8 | 0.0542(17) | 0.0719(16) | 0.0218(17) | 0.00835(13) | 0.00502(21) | 0.0365(5) |
| Tl+ | 8/20/03 | 0.58 | 6.3 | 0.0495(17) | 0.0860(15) | 0.0368(15) | 0.000412(131) | −0.00740(21) | 0.00440(47) |
| | 9/2/03 | 0.25 | 3.5 | 0.0443(10) | 0.050200 | 0.0324(11) | 0.00141(10) | −0.00228(13) | 0.00898(37) |
| | 9/10/03 | 0.184 | 3 | 0.0253(13) | 0.0355(12) | 0.0077(15) | 0.000877(106) | −0.00244(17) | 0.00915(48) |
| | 9/30/03 | 1.39 | 10.8 | 0.0311(12) | 0.0354(13) | −0.0559(15) | 0.0143(1) | −0.0142(2) | 0.0721(5) |
| | | | | **$b_0$=mobility** | **$b_0$=mobility** | **$b_0$=mobility** | $b_1$ | $b_1$ | $b_1$ |
| $Mg^+$ | 4/3/03 | 0.58 | 6.3 | 0.000251(2) | 0.000240(2) | 0.000222(2) | 0.00000476(14) | 0.0000101(2) | 0.0000247(5) |
| | 11/25/03 | 0.57 | 6.3 | 0.000270(1) | 0.000245(1) | 0.000243(1) | 0.000000946(55) | 0.00000778(11) | 0.0000131(2) |
| $Ca^+$ | 4/11/03 | 0.58 | 6.3 | 0.000303(1) | 0.000292(1) | 0.000294(1) | 0.0000000318(38) | 0.00000319(7) | 0.00000388(15) |
| | 11/14/03 | 0.57 | 6.3 | 0.000280(1) | 0.000251(1) | 0.000255(1) | −0.000000747(64) | 0.00000629(15) | 0.00000602(29) |
| $Sr^+$ | 11/26/03 | 0.57 | 6.3 | 0.000300(2) | 0.000273(2) | 0.000273(2) | 0.00000119(10) | 0.00000823(18) | 0.0000137(4) |
| $Ba^+$ | 4/25/03 | 0.58 | 6.3 | 0.000253(1) | 0.000202(1) | 0.000222(1) | 0.000000240(42) | 0.000000879(8) | 0.00000998(19) |
| | 5/5-6/2003 | 0.58 | 6.3 | 0.000244(1) | 0.000235(1) | 0.000227(1) | 0.000000283(23) | 0.00000294(5) | 0.00000634(4) |
| | 9/10/03 | 0.184 | 3 | 0.000191(8) | 0.000176(1) | 0.000179(1) | 0.00000159(6) | 0.00000767(13) | 0.0000101(3) |
| | 10/3/03 | 1.39 | 10.8 | 0.000211(13) | 0.000181(1) | 0.000167(1) | 0.00000121(9) | 0.0000105(2) | 0.0000201(4) |
| $Tl^+$ | 8/20/03 | 0.58 | 6.3 | 0.000204(1) | 0.000176(1) | 0.000177(1) | 0.00000297(7) | 0.0000117(1) | 0.0000203(3) |
| | 9/2/03 | 0.25 | 3.5 | 0.000153(1) | 0.000142(5) | 0.000128(1) | 0.00000344(6) | 0.0000106(1) | 0.0000196(2) |
| | 9/10/03 | 0.184 | 3 | 0.000198(1) | 0.000188(1) | 0.000188(1) | 0.00000161(5) | 0.00000663(10) | 0.00000907(23) |
| | 9/30/03 | 1.39 | 10.8 | 0.000198(1) | 0.000177(1) | 0.000181(1) | −0.000000966(68) | 0.00000720(13) | 0.00000535(34) |

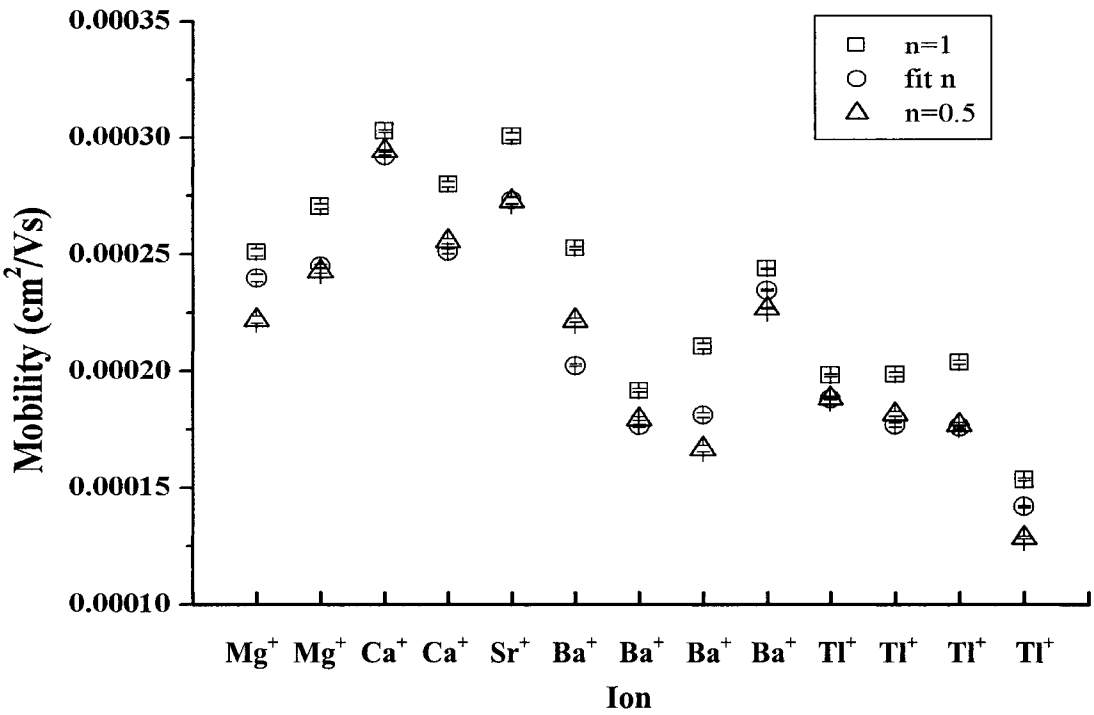


**Figure 6-13 Ionic mobility determined by a global fit with three different power of charge dependence n.**

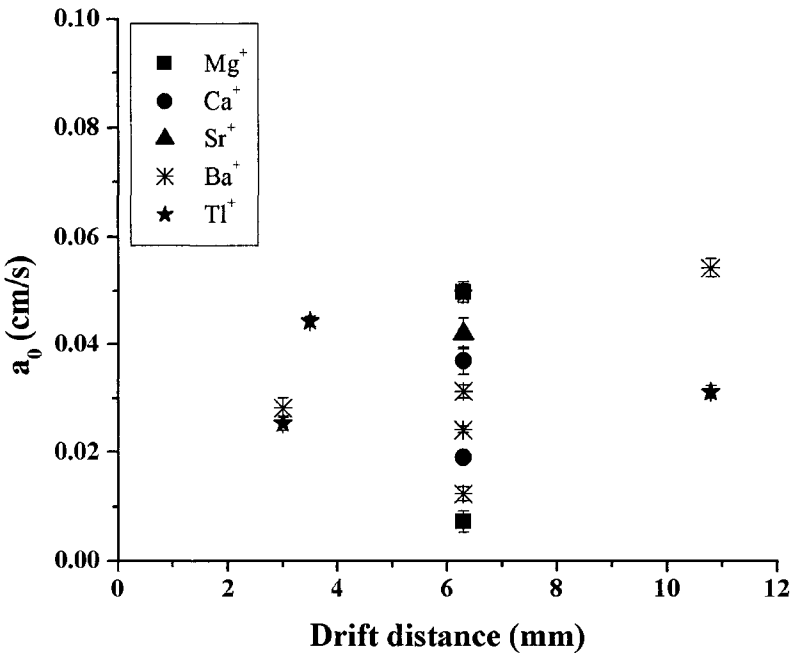


**Figure 6-14(a) Residual fluid flow $a_0$ as a function of drift distance. n=1.**

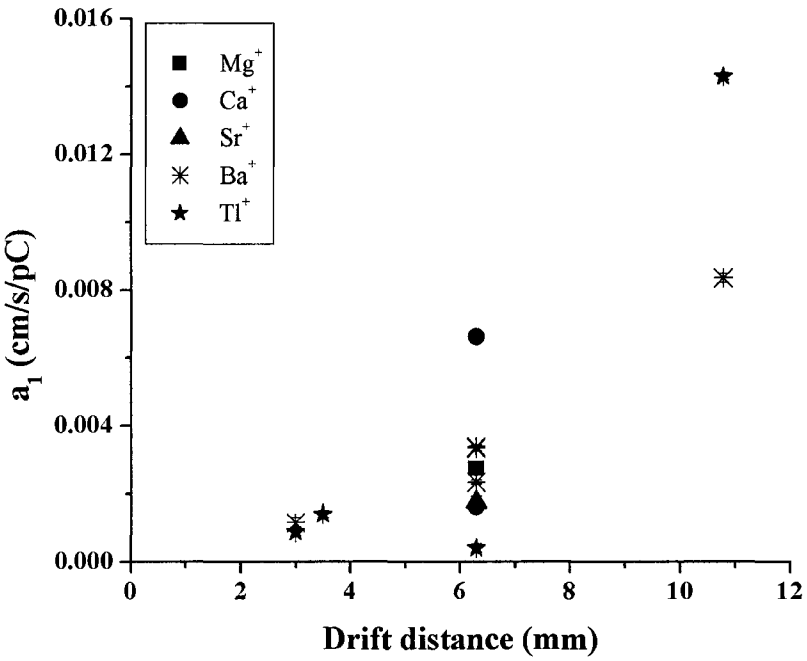


**Figure 6-14(b) $a_1$ as a function of drift distance. n=1.**

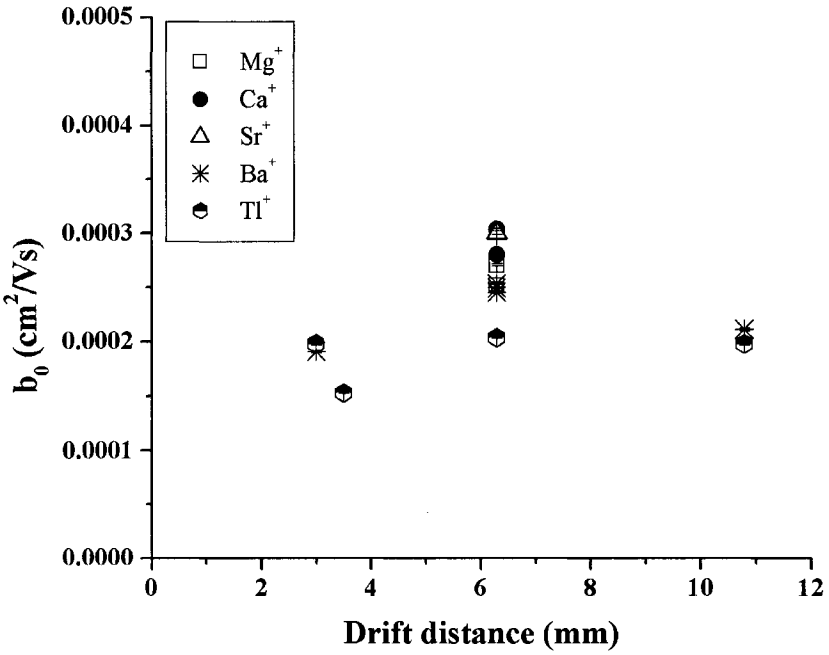


**Figure 6-14(c) Mobility $b_0$ as a function of drift distance. n=1.**

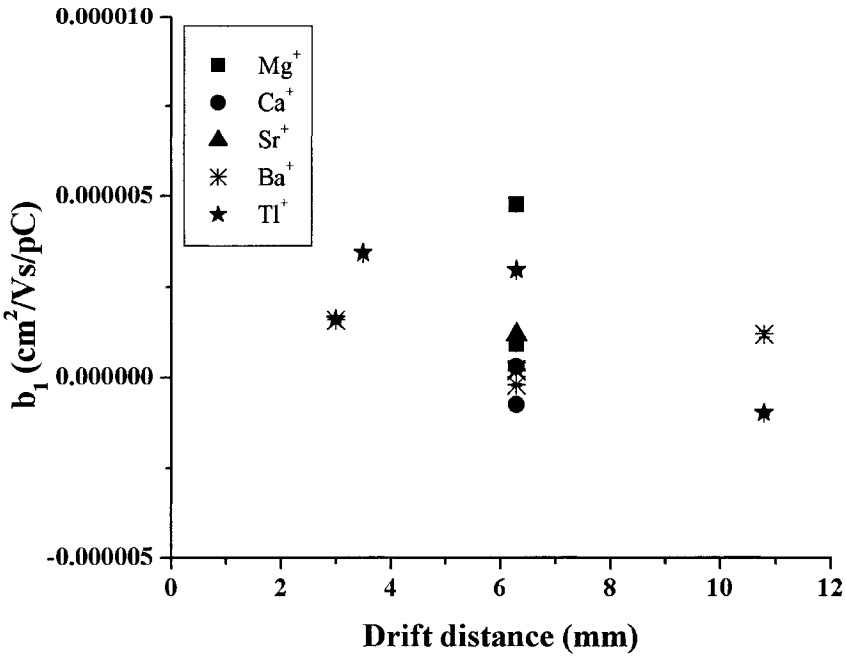


**Figure 6-14(d) $b_1$ as a function of drift distance. n=1.**

distances does not show any clear dependence on drift distance (Fig. 6-14(c)). Thus it is believed that the charged-induced fluid motion is well corrected.

The main uncertainty for the mobility results is from the systematic error because the statistical error is less than 1% and is ignorable. The systematic errors are mainly from the uncertainty in the exact nature of the $Q$ and $E$ dependence of the correction factors, and from a ± 0.5 mm error in determination of drift distance. The error limit shown in Table 6-5 from the correction factor, $\Delta\mu(n)$, is determined from the maximum value of the absolute value of difference $\mu(n=1)-\mu(\text{fit } n)$ and $\mu(\text{fit } n)-\mu(n=0.5)$. The percentage error from the drift distance, $\Delta\mu(d)$, is calculated as $2\Delta d/d$. It can be seen from Table 6-5 and Fig. 6-13 that the error limit from $\Delta\mu(d)$ is random, and it should be reduced by multiple measurements. On the other hand, the error limit from $\Delta\mu(n)$ has

**Table 6-5 Summary of ionic mobility at 170 K by global fit and error consideration.**

| Date | Ion | μ (n=1) $cm^2/Vs$ | Δμ $cm^2/Vs$ | **μ (fit n) $cm^2/Vs$** | **Δμ $cm^2/Vs$** | μ (n=0.5) $cm^2/Vs$ | Δμ $cm^2/Vs$ | d (mm) | Δμ (n) $cm^2/Vs$ | Δμ (d) $cm^2/Vs$ | Δμ(total) $cm^2/Vs$ | Δμ(random) $cm^2/Vs$ |
|---|---|---|---|---|---|---|---|---|---|---|---|---|
| 4/3/03 | $Mg^+$ | 0.0002508 | 0.0000016 | **0.0002397** | **0.0000016** | 0.0002218 | 0.0000016 | 6.3 | 0.0000179 | 0.0000380 | 4.2078E-05 | 3.8081E-05 |
| 11/25/03 | $Mg^+$ | 0.0002703 | 0.0000010 | **0.0002451** | **0.0000009** | 0.0002428 | 0.0000009 | 6.3 | 0.0000252 | 0.0000389 | 4.6362E-05 | 3.8915E-05 |
| 11/03 | $Ca^+$ | 0.0003027 | 0.0000005 | **0.0002918** | **0.0000005** | 0.0002940 | 0.0000005 | 6.3 | 0.0000109 | 0.0000463 | 4.7585E-05 | 4.632E-05 |
| 11/14/03 | $Ca^+$ | 0.0002797 | 0.0000013 | **0.0002511** | **0.0000011** | 0.0002554 | 0.0000011 | 6.3 | 0.0000286 | 0.0000399 | 4.9069E-05 | 3.9872E-05 |
| 11/26/03 | $Sr^+$ | 0.0003005 | 0.0000016 | **0.0002730** | **0.0000015** | 0.0002726 | 0.0000015 | 6.3 | 0.0000275 | 0.0000433 | 5.1345E-05 | 4.3359E-05 |
| 4/25/03 | $Ba^+$ | 0.0002525 | 0.0000007 | **0.0002023** | **0.0000006** | 0.0002217 | 0.0000008 | 6.3 | 0.0000502 | 0.0000321 | 5.9595E-05 | 3.2117E-05 |
| 9/10/03 | $Ba^+$ | 0.0001914 | 0.0000008 | **0.0001763** | **0.0000007** | 0.0001793 | 0.0000008 | 3 | 0.0000151 | 0.0000588 | 6.068E-05 | 5.8771E-05 |
| 10/3/03 | $Ba^+$ | 0.0002106 | 0.0000013 | **0.0001810** | **0.0000012** | 0.0001665 | 0.0000013 | 10.8 | 0.0000296 | 0.0000168 | 3.4036E-05 | 1.6802E-05 |
| 5/5-6/03 | $Ba^+$ | 0.0002437 | 0.0000004 | **0.0002347** | **0.0000004** | 0.0002268 | 0.0000004 | 6.3 | 0.0000090 | 0.0000373 | 3.8328E-05 | 3.7256E-05 |
| 9/10/03 | $Tl^+$ | 0.0001980 | 0.0000006 | **0.0001879** | **0.0000005** | 0.0001882 | 0.0000006 | 3 | 0.0000101 | 0.0000626 | 6.3444E-05 | 6.2635E-05 |
| 9/30/03 | $Tl^+$ | 0.0001984 | 0.0000009 | **0.0001767** | **0.0000010** | 0.0001814 | 0.0000011 | 10.8 | 0.0000217 | 0.0000164 | 2.7195E-05 | 1.6392E-05 |
| 8/20-21/03 | $Tl^+$ | 0.0002037 | 0.0000009 | **0.0001759** | **0.0000008** | 0.0001768 | 0.0000008 | 6.3 | 0.0000278 | 0.0000279 | 3.9409E-05 | 2.7932E-05 |
| 9/2-3/03 | $Tl^+$ | 0.0001533 | 0.0000006 | **0.0001420** | **0.0000005** | 0.0001284 | 0.0000006 | 3.5 | 0.0000136 | 0.0000406 | 4.2793E-05 | 4.0575E-05 |

| Wt. Average | | | syst. error | | random | | syst. error | N | +error | -error |
|---|---|---|---|---|---|---|---|---|---|---|
| | | | $\Delta\mu_+(n=1)$ | | error | | $\Delta\mu_+(n=0.5)$ | | $\Delta\mu_+$ | $\Delta\mu_-$ |
| Wt. Average | Mg+ | 0.0002596 | 0.0000175 | **0.0002421** | **0.0000285** | 0.0002313 | -0.0000109 | 1.82 | 0.0000334 | 0.0000305 |
| | Ca+ | 0.0002916 | 0.0000195 | **0.0002721** | **0.0000310** | 0.0002753 | 0.0000032 | 1.94 | 0.0000366 | 0.0000312 |
| | Sr+ | 0.0003005 | 0.0000275 | **0.0002730** | **0.0000434** | 0.0002726 | -0.0000004 | 1.00 | 0.0000513 | 0.0000434 |
| | Ba+ | 0.0002245 | 0.0000238 | **0.0002007** | **0.0000198** | 0.0001951 | -0.0000055 | 2.43 | 0.0000310 | 0.0000206 |
| | Tl+ | 0.0001908 | 0.0000200 | **0.0001707** | **0.0000194** | 0.0001706 | -0.0000001 | 2.06 | 0.0000279 | 0.0000194 |

correlation with the n value; n=0.5 and n=1 provide the lower and upper limits respectively, and it cannot be treated as a random error.

The best values of mobility will be quoted by the global fit results with the power of Q dependence of fit-n. The final determination of the error budget and the average mobility is calculated by the following procedure.

(a) Determine the weighting factor $W_i$ from the total error on each run.

$$W_i = 1/\Delta\mu_i^2 \qquad 6\text{-}10$$

(b) Determine the ionic mobility for each n value by using the weighting factor $W_i$

$$\mu = \sum_i W_i u_i(n) / \sum_i W_i \,. \qquad 6\text{-}11$$

(c) Determine the systematic errors $\Delta\mu_+(n=1)$ and $\Delta\mu_-(n=0.5)$ by calculating the mobility differences of the n=1 and n=0.5 fits relative to n= fit-n.

(d) Determine the final random error for fit-n with weighted sum over $\Delta\mu_i$ (d) values.

$$\Delta\mu_{random} = \frac{\sum_i W_i \Delta\mu_i(d)}{(\sum_i W_i)\sqrt{N}}, \qquad 6\text{-}12$$

where $N$ is statistically the effective number of runs, given as

$$N = \frac{\sum_i W_i}{Max\{W_i\}}. \qquad 6\text{-}13$$

The $\frac{1}{\sqrt{N}}$ factor converts a standard derivation to a standard derivation of the mean.

(e) Add $\Delta\mu_{random}$ to $\Delta\mu_+(n=1)$ and $\Delta\mu_-(n=0.5)$ in quadrature to get $\Delta\mu_+$ and $\Delta\mu_-$ for the final error limits.

The final results are also summarized in Table 6-5, and the ionic mobility as a

function of atomic number is plotted in Fig. 6-15. It indicates that the mobility is different for different ion core, and $Ca^+$ has the biggest mobility.

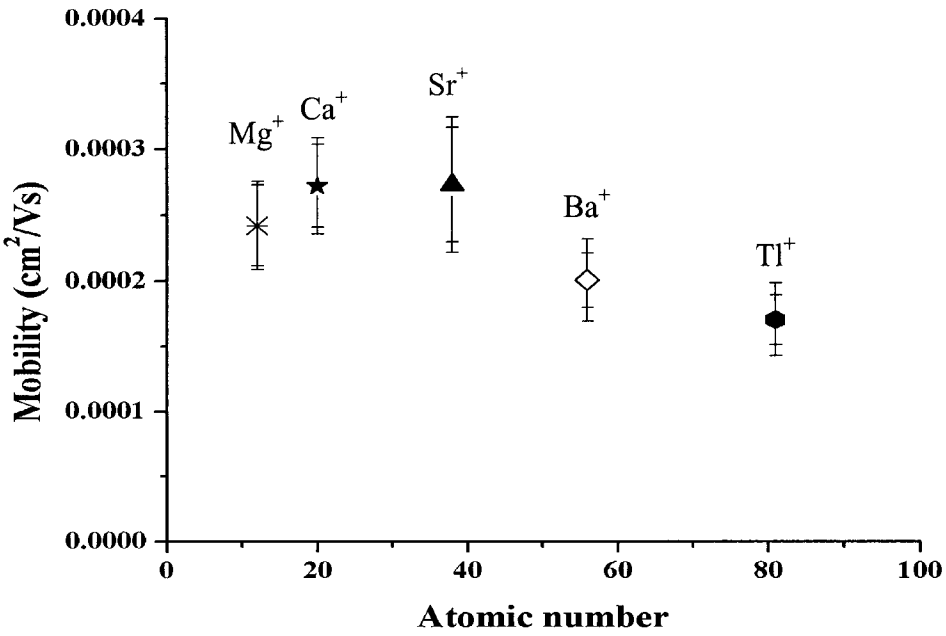


**Figure 6-15 Ionic mobility as a function of atomic number.**

In addition, the mobility of alkaline earth ions, $Ma^+$, $Ca^+$, $Sr^+$ and $Ba^+$, as a function of temperature was studied in a temperature range from 162 K to 182 K. Results for one run of $Ba^+$ mobility in which about 100 pulses were analyzed at each of 8 different temperatures is shown in Fig. 6-16. The parameters of the global fit from the same day were used to correct residual fluid flow and $Q$ and $E$-dependent effects. The mobility is almost constant with only a slight increase as the temperature increases. Data for the other alkaline earth ions and another $Ba^+$ run are shown in Fig. 6-17(a)-(d). The data were taken at a fixed E-field (1466V/cm) and a constant drift distance $d_{drift}$ (6.3cm), and only one data point was recorded at each temperature as the liquid xenon was heating

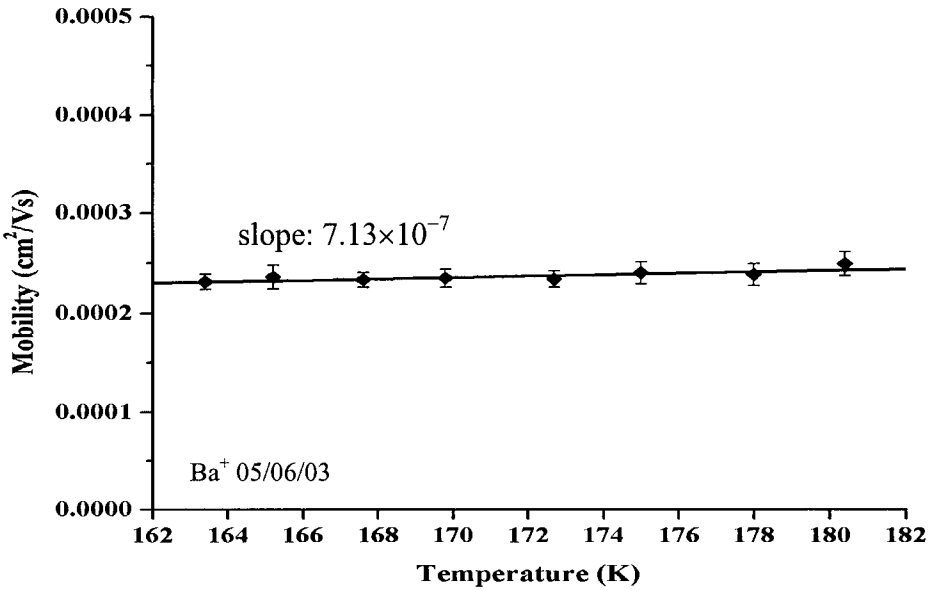


**Figure 6-16 Mobility of $Ba^+$ as a function of temperature in LXe.**

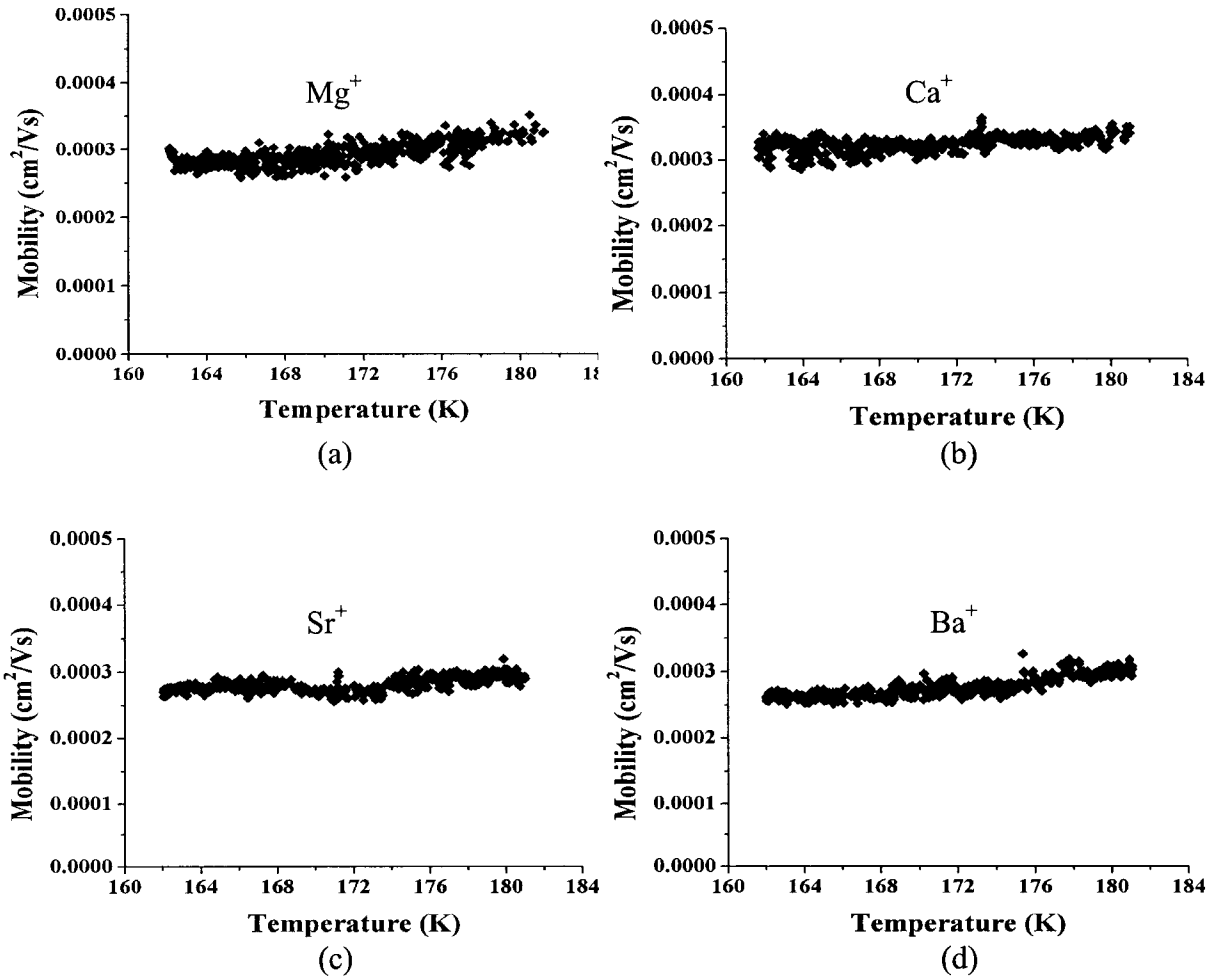


**Figure 6-17 Mobility of (a) $Mg^+$, (b) $Ca^+$, (c) $Sr^+$, and (d) $Ba^+$ as a function of temperature in LXe.**

up. There was not enough data at different voltages to do a global fit and to get absolute corrections for these measurements. Thus only a $Q^{0.814}$ correction was applied to obtain the true mobility. Nevertheless the results for these ions show the very similar temperature dependence. The mobility slightly increases with temperature.

One final concern for the charge-induced fluid motion is whether it is in the streamlined or the turbulent region. It is found that the onset of turbulence in a tube is determined by a dimensionless factor called the Reynolds number, given as [3]

$$R = \frac{\rho v d}{\eta}, \qquad 6\text{-}14$$

where $\rho$ is the density of the fluid, v is the average velocity of the fluid along the direction of flow, $d$ is the diameter of the tube, and $\eta$ is the viscosity of the fluid. The flow of fluid through a tube is streamlined if $R$ is below about 2000, and turbulent if $R$ is above 3000. The flow is unstable in the region between 2000 and 3000. For our measurement system, the flow of fluid depended on the charge and electric field, and the average velocity of fluid ranged from 0.1 to 1.8 cm/s. The density $\rho$ and viscosity $\eta$ of liquid xenon are 2953 kg/m$^3$ and 0.0005 Ns/m$^2$. The parameter $d$ was estimated by the size of the charge cloud, and it was about 5 mm in our system. The Reynolds number can then be determined to be in the range 30 to 550. The Reynolds number was well below 2000, so no turbulence by the charge-induced fluid motion was expected in our measurements.

## 6-4 Discussion of the mobility results

Mobility of alkaline earth and $Tl^+$ ions as a function of atomic number has been shown in Fig. 6-15. Looking first at the differences in mobility, there is a significantly

higher mobility for the lighter alkaline earth ions than for $Ba^+$ and $Tl^+$. One should look at the smaller statistical error bars in evaluating the significance of these differences. A more detailed theoretical model is needed for understanding this difference in the future.

The mobility of $^{208}Tl^+$ and $^{226}Th^+$ ions created by a radioactive α-source in liquid xenon was studied recently [4,5]. Because of the small number of ions created in the mobility measurements, fluid motion is ignorable in their experiments. Therefore, it is interesting to compare their results to those obtained in our system. Walters and Mitchell reported a field independent mobility of $^{208}Tl^+$ in liquid xenon as 0.000133(4) $cm^2V^{-1}s^{-1}$ [4,6]. Their data were taken at two short drift distances of 3.1 mm and 6mm and at a long drift distance of 50 mm. They also measured the mobility at two different temperatures, 163 K and 166 K, and no significant temperature dependence was observed. Unfortunately, our result ($0.000171^{+30}_{-19}$ $cm^2V^{-1}s^{-1}$) and theirs (0.000133(4) $cm^2V^{-1}s^{-1}$) do not agree within the quoted error limits. We note that systematic errors were not mentioned in the paper of Walter and Mitchell. For example, they gave the uncertainty of drift distance as 0.25 mm in their system, but apparently did not include it in the final error. The resulting systematic errors for 3.1 mm and 6 mm drift distance were 16.2% and 8.4 % ($2\Delta d/d$) respectively. An increase in the error limit in the result of Walters and Mitchell might bring our results into agreement.

Ionic mobility measurements in LXe from our results, Ref. 4, Ref. 6 and Ref. 7 as a function of the ionic radius are shown in Fig. 6-18. They do not show a clear dependence of mobility on the ionic radius. Walters and Mitchell suggested that the positive ion mobility in liquid xenon is proportional to the hard-core radius on the basis of the mobility data for $Tl^+$ and $TMSi^+$ only [4]. Our additional results do not support this

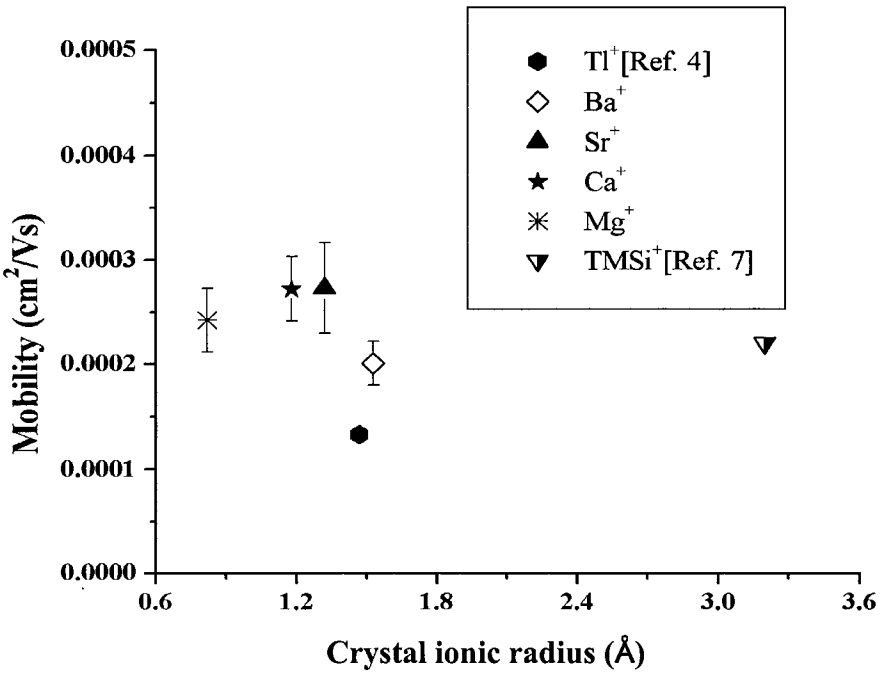


**Fig. 6-18 Ionic mobility as a function of ion core radius in LXe**

conclusion, and might favor a constant or reverse trend. Walters and Mitchell argue that the smaller the radius *r*, the stronger the electric field ($E \sim q/r^2$). The ion with the stronger field will have more neutral polarizable Xe atoms clustering around it, making it slower through the liquid. It is not clear that this argument makes any sense because at a given radius outside all ions, the electric field should be the same. A uniform model of condensed "snowball" size is discussed below and in Chapter 3.

Studies of ionic mobility in liquid helium yield the results shown in Fig. 6-19 when normalized to the mobility of $He^+$ [9-11]. It is interesting that the small difference between alkaline earth and alkali ion mobility is interpreted as a difference between bubble and snowball structure, respectively [12]. The ionic mobility in liquid helium might show a slight dependence on the ionic radius or atomic number. The mobility slight increases with ionic radius for ions with a bubble structure. The reverse trend is seen for the ions with a snowball structure. Our results for alkaline earth ions in liquid

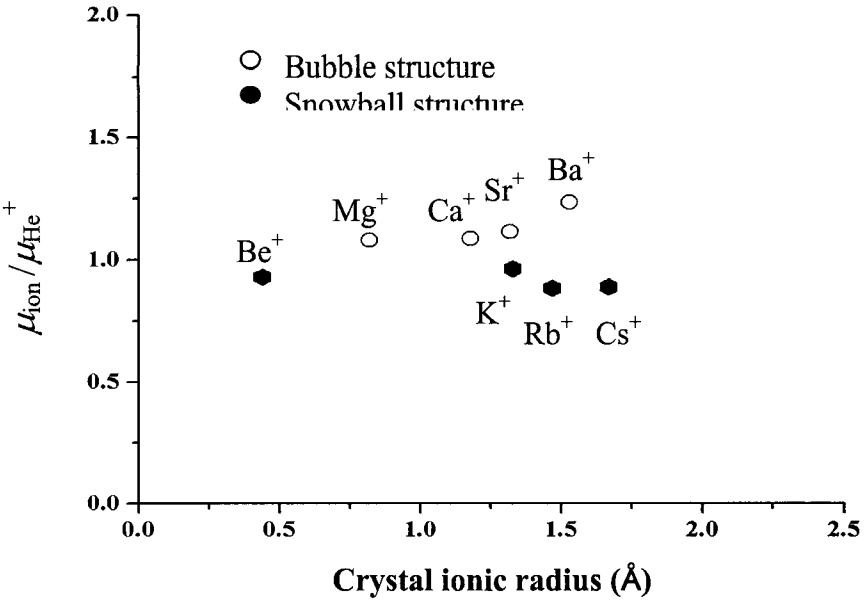


**Figure 6-19 Ionic mobility as a function of ionic radius in superfluid helium.**

xenon shown in Fig. 6-18 are more consistent with the snowball structure trend in liquid helium, but this is a weak argument for discriminating between structures.

The previous measurements of the mobility of $O_2^-$, $SF_6^-$, n-pentane$^+$ and TMSi$^+$ in liquid xenon by Hilt *et al.* [7,8]], $Tl^+$ by Walters and Mitchell [4], $Th^+$ by Wamba et al. [5] and our work for alkaline earth ions have shown that positive ions have significantly smaller mobility than negative ions in liquid xenon, on the order of 0.0002 $cm^2V^{-1}s^{-1}$ and 0.0007 $cm^2V^{-1}s^{-1}$, respectively. Khrapak and Volykhin speculate that this difference is due to the formation of a different structure, a "bubble" in the liquid, around the negative ion [13]. A firm conclusion on the structure surrounding the alkaline earth ions from our work cannot be reached yet.

The temperature dependence of the mobility might provide one way for probing the structure of the fluid surrounding the ion. Our positive ion mobility data taken at various temperatures, along with the theoretical predictions of the Akins and Hilt *et al.*

electrostriction model presented in Chapter 3, are shown in Fig. 6-20. Because the temperature-dependence data runs did not have enough data at different voltages for an absolute fluid motion correction, we have adjusted the μ(T) of Fig. 6-17 for each ion with a factor of the ratio of μ(170K) in each run to the absolute ionic mobility at 170 K given in Table 6-5. This adjustment provides an approximate absolute determination of μ(T). It is interesting that the simple electrostriction model can predict the magnitude of ionic mobility within a factor of 2. However, neither our data in Fig. 6-20 nor the data of Hilt *et al.* in Fig. 3-3 shows any evidence of the predicted dramatic change in mobility near the triple point. Clearly the model is incomplete or the parameters used in the model are incorrect.

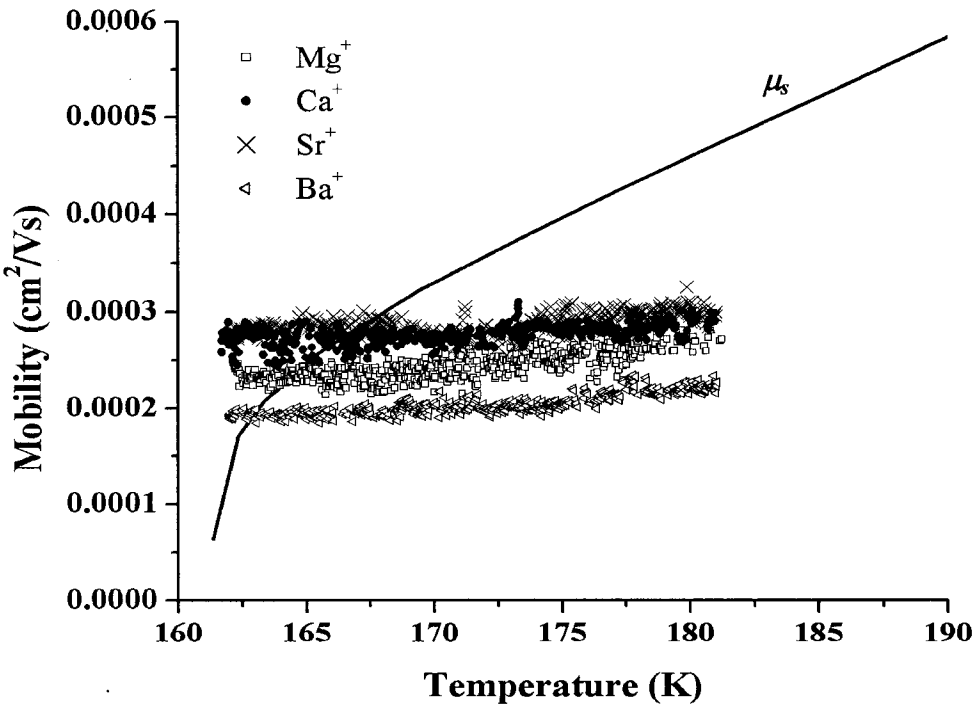


**Figure 6-20 Theoretical and measured ionic mobility in LXe as a function of temperature.**

One of the uncertain parameters in the model is the surface tension at the liquid-solid interface. It has not been measured, but was only extrapolated from the liquid-gas interface value according to the suggestion of Bachinsky [14,15], given as

$$\sigma_{sl} \cong \sigma_{\lg}(\frac{n_s - n_l}{n_l})^4. \qquad 6\text{-}15$$

An increase in the surface tension $\sigma_{sl}$ by an order of magnitude can nearly eliminate the predicted sharp decrease in mobility near the triple point. In Fig. 6-21, predictions using a surface tension $\sigma_{sl}$ scaled by 10 and 40 times are shown by the dashed and dotted lines, respectively. Helium is the only noble gas whose surface tension has been measured along both the liquid-gas $\sigma_{lg}$ and solid-liquid $\sigma_{sl}$ interfaces. The measured $\sigma_{lg}$ is about 0.32 at 1.7 K [16]. According to Eq. 6-15, the expected $\sigma_{sl}$ is estimated as 0.00297 erg/cm$^2$, in which $n_s$=0.19 g/cm$^3$ and $n_l$=0.145 g/cm$^3$ are used [16,17]. However, the measured $\sigma_{sl}$ was reported as 0.098 erg/cm$^2$ [18], i.e., a factor of 33 higher than prediction. Therefore, it is highly possible that the theoretical prediction of a sharp decrease in mobility near the triple point is incorrect because the surface tension along the solid-liquid interface was underestimated in the original Hilt *et al.* model.

Nevertheless, the model remains an imperfect fit to experiment because the predicted slope of $\mu$ vs. $T$ is not right. The viscosity in the vicinity of the ion increases due to the electrostriction effect. Hilt *et al.* and Ostermeier and Schwarz have suggested two different methods to treat the modified viscosity around the ion as discussed in Chapter 3. The theoretical mobility with surface tension of $40\times\sigma_{sl}$ and viscosity of $\eta_s$, $\eta_m$, and $\eta_F$ along with measured $\mu$ (T) are illustrated in Fig. 6-22. It can been seen that $\mu_m$(T) agrees with the measured mobility well. Although the ion mobity in normal liquid helium

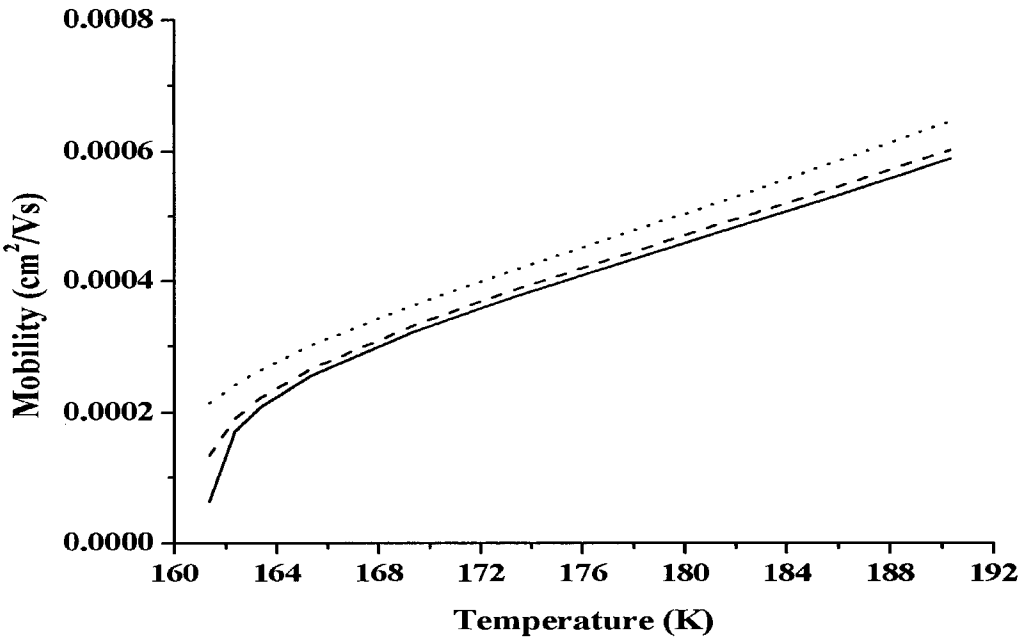


**Figure 6-21 Theoretical mobility $\mu_s$ as a function of temperature at various surface tension $\sigma_{sl}$ . Solid line: $\sigma_{sl}$. Dash line: $10\times\sigma_{sl}$. Dot line: $40\times\sigma_{sl}$. The $\mu_s$ here is calculated by using the viscosity along the gas-liquid interface.**

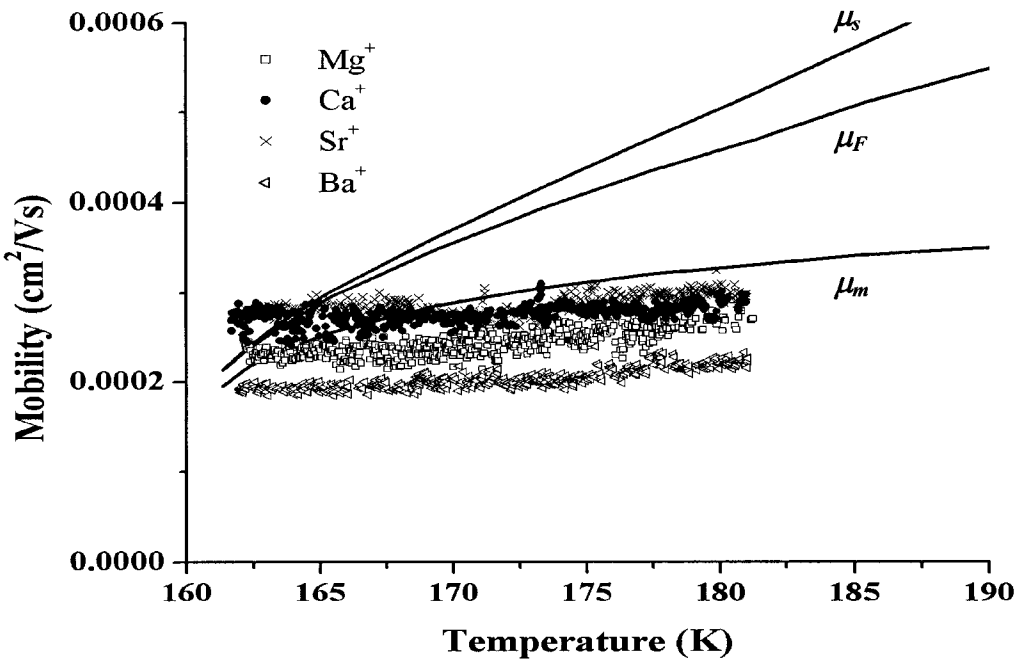


**Figure 6-22 Theoretical and measured ionic mobility in LXe as a function of temperature, where $40\times\sigma_{sl}$ was used. The meaning of $\mu_s$, $\mu_F$ and $\mu_m$ can be found in Ch. 3.**

was well interpreted in the temperature range from 2.17 K to 4.2 K based on the model of Ostermeier and Schwarz ($\mu_F$ model) [19], this model predicts too great an increase in mobility with temperature in liquid xenon. The observed slight increase of ionic mobility in liquid xenon with temperature agrees better with the suggestion of Hilt *et al.*, i.e. that the viscosity along the liquid-solid interface (melting line) should be used.

# References


1. P. Langevin, Ann. Chim. Phys. 28, 289 (1903).
2. E.P.T. Mitchell, The mobility of positive ions in gases, Cambridge University Press, London 1938.
3. R.A. Serway and J.S. Faughn, College Physics, 3rd Edition, A Harcourt Brace Jovanovich Publisher, 1992.
4. A.J. Walters and L.W. Mitchell, J. Phys. D. 36, 1323 (2003).
5. K. Wamba, C. Hall and P. C. Rowson, SLAC, private communication.
6. A.J. Walters, Ph. D. dissertation, Flinders University of South Australia, 2002.
7. O. Hilt, W.F. Schmidt and A.G. Khrapak, IEEE Trans. Electr. Ins. 1, 648 (1994).
8. W.F. Schmidt, Liquid state electronics of insulating liquids, CRC press, 1997.
9. W.I. Glaberson and W.W. Jonson, J. Low Temp. Phys. 20, 313 (1975).
10. H. Gunther, M. Foerste, M. Kunze, G. zu Putlitz and U. von Stein, Z. Phys. B. 101, 613 (1996).
11. M. Foerste, H. Guenther, O. Riediger, J. Wiebe, G. zu Putlitz, J. Low Temp. Phys. 110, 231 (1998).
12. M.W. Cole and R.A. Bachman, Phys. Rev. B. 15, 1388 (1977).
13. A.G. Khrapak and K.F. Volykhin, JETP 88, 320 (1999).
14. J.O. Hirschfelder et al., Molecular Theory of Gases and liquids, John Wiley&Sons, New York, 1964.
15. A.G. Khrapak et al., IEEE Trans. Electr. Ins. 26, 582 (1991).
16. R.J. Donnelly and C.F. Barenghi, J. Phys. Chem. Ref. Data 27, 1217 (1998).
17. E.R. Grilly, J. Low Tem. Phys. 11, 33 (1973).
18. S. Balibar et al., Phys. Rev. Lett. 42, 782 (1979).
19. R.M. Ostermeier and K.W. Schwarz, Phys. Rev. A 5, 2510 (1972).

# Chapter 7

## Results and Discussion
## Laser spectroscopy of $Ba^+$ in liquid xenon

Results for excitation, fluorescence, and plasma emission spectra and cloud images of $Ba^+$ in liquid xenon by using the method of laser-induced fluorescence will be presented in this chapter.

### 7-1 Plasma emission spectrum of laser ablated barium

Plasma emission spectroscopy is a useful method to identify the predominant species in the laser ablation plasma. The plasma spectrum for laser ablation of a metal sample in liquid xenon might also show the properties of the broadening and shift of fluorescence peaks of excited atoms and ions as they are pulled into the adjacent liquid.

Plasma emission spectra of Nd:YAG laser ablated barium metal in gaseous and liquid xenon are shown in Fig. 7-1 (a) and (b), respectively. The emission spectra were detected by a spectrometer with a $LN_2$-cooled CCD array detector. A room temperature CCD array detector was also used to record the plasma emission in xenon gas, and the same results were obtained. As shown in Fig. 7-1(a), the emission lines of the spectrum in gas are mainly from $Ba^+$ and Ba. In fact, nearly every peak can be identified as transitions from $Ba^+$ and Ba. The dominant emissions of $Ba^+$ are the resonant blue and blue-green lines, $6p \rightarrow 6s$, and the transitions from the 6p to the metastable 5d states. The dominant emission of Ba is the 553 nm resonant line, $6s6p \rightarrow 6s^2$. We should mention here that the whole spectrum was obtained by joining several frames, so the relative emission strengths might be not correct. Also some transitions show a self-absorption dip, for example Ba $6s6p \rightarrow 6s^2$ in Fig. 7-1(a). Due to the resolution of spectrometer (2 nm for

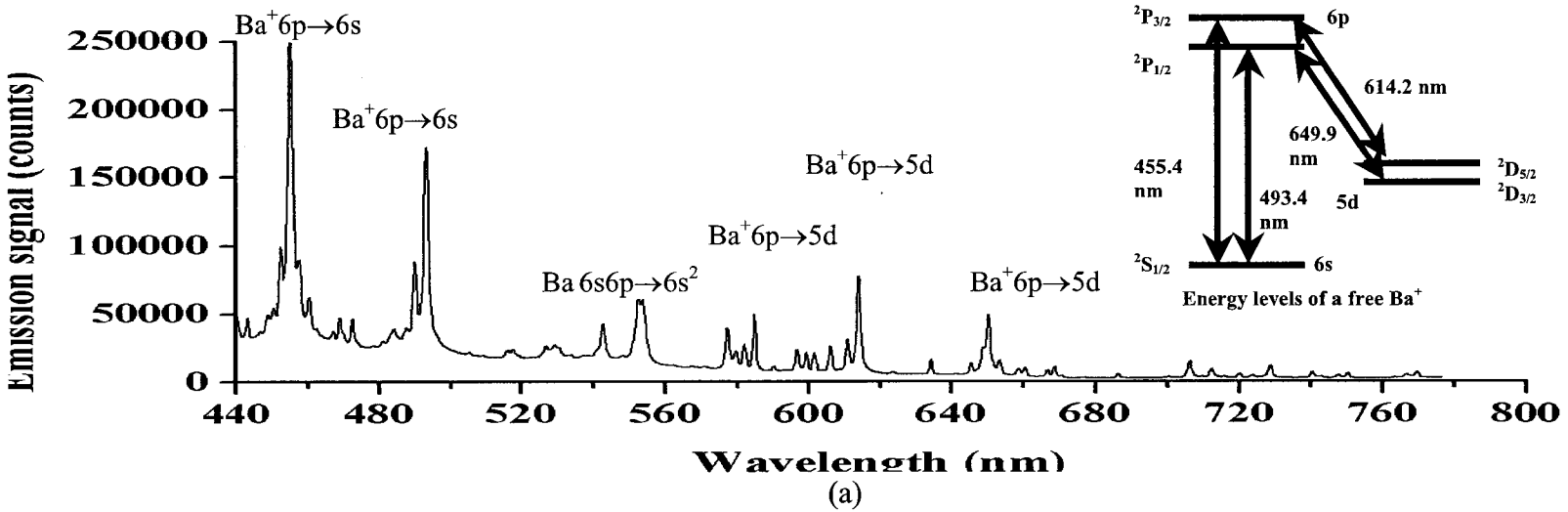


(a)

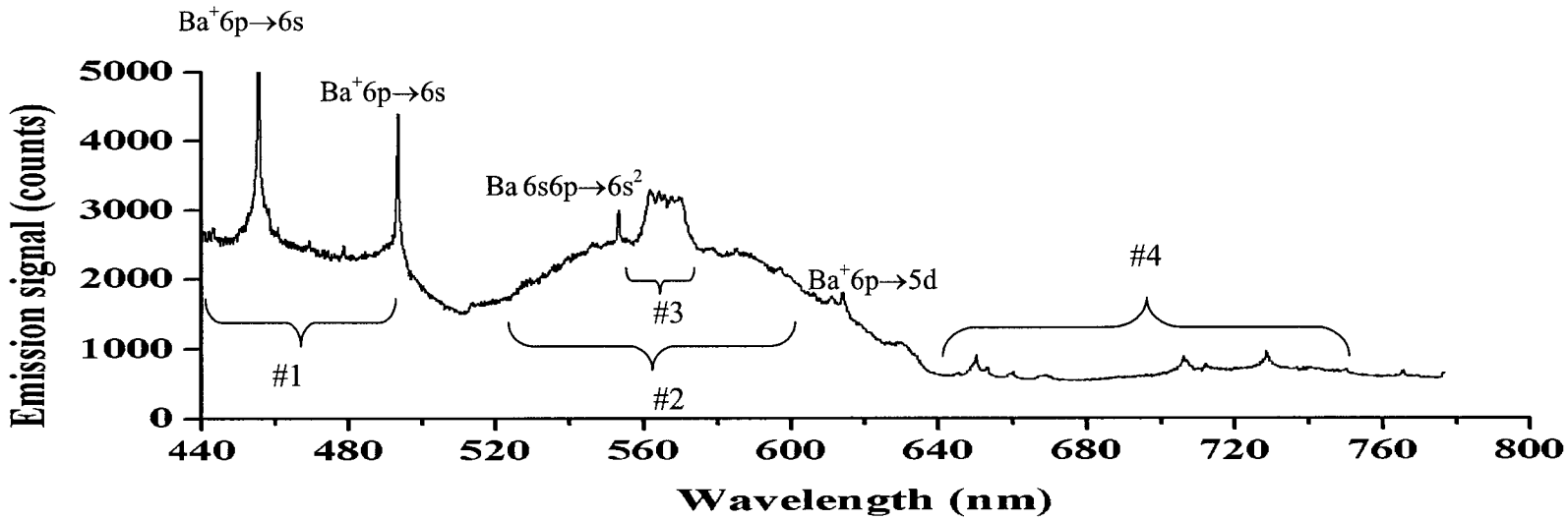


(b)

**Figure 7-1 Plasma emission spectra of laser ablation Ba metal in (a) gaseous xenon and (b) liquid xenon.**

Fig. 7-1(a) and 1 nm for Fig. 7-1(b)), the frequency shift and line broadening of these resonance lines in gaseous xenon cannot be determined.

The sharp emission lines of $Ba^+$ and Ba are seen in both gaseous and liquid xenon plasma spectra. The sharp emission features in liquid might be from the plasma forming a small gas bubble in the liquid xenon. In addition to those sharp lines, the plasma emission spectrum in liquid shows at least two or four possibly broad bumps labeled #1 to #4 in Fig. 7-1(b). According to the transitions of a free $Ba^+$ and Ba, we might assign that the broad bumps #1 to #4 are corresponding to emissions of $P_{3/2} \rightarrow S_{1/2}$ and $P_{1/2} \rightarrow S_{1/2}$ of $Ba^+$, $^1P_1 \rightarrow {}^1S_0$ of Ba, and $P_{1/2,3/2} \rightarrow D_{3/2,5/2}$ of $Ba^+$, respectively. The absorption and emission spectra of Ba atoms in solid noble gas matrices have been studied by Balling and Wright [1]. A 15 nm wide emission peak around 568 nm was observed in solid Ar and Kr matrix. Thus bump #3 with 20 nm in width at 570 nm center wavelength is quite likely the Ba emission ($^1P_1 \rightarrow {}^1S_0$) in LXe matrix. Since $Ba^+$ has stronger interaction with Xe atoms than Ba, a broader and more red-shifted emission is possible for $Ba^+$ in Xe. The broad structures #1, #2, and #4 are therefore assigned as $Ba^+$ emission lines. These broad emission peaks might provide valuable information in searching for the laser-induced fluorescence spectrum of $Ba^+$ in LXe. Thus the laser-induced fluorescence bands of $Ba^+$ in liquid xenon around 460 nm, 560 nm and 680 nm with 80 nm in width might be expected for the transitions of $P_{3/2} \rightarrow S_{1/2}$, $P_{1/2} \rightarrow S_{1/2}$, and $P_{1/2,3/2} \rightarrow D_{3/2,5/2}$ respectively. However, there are also other possible decay chains from higher excited states which correspond to the weaker sharp lines in Fig. 7-1(a). They could contribute also to the broad bumps. Therefore it is not possible to identify unambiguously the correspondences between the emission lines and the broad bumps.

## 7-2 Excitation spectra

According to the educated guess for the absorption spectrum of $Ba^+$ in liquid xenon as discussed in Section 4-3, three broad absorption bands covering the $S_{1/2} \rightarrow P_{1/2}$ and $S_{1/2} \rightarrow P_{3/2}$ transitions in the blue and blue-green region may be expected. An argon ion laser with 9 lasing lines from 454 nm to 514 nm is just suitable to excite $Ba^+$. Nine discrete argon ion laser lasing lines were used separately to excite the $Ba^+$ ions in liquid xenon, and the total rate of emission photons was detected by a cooled PMT, as shown in Fig. 5-16. The excitation spectrum will be the same as the absorption spectrum if the emission probability and spectrum after excitation is the same for each wavelength of excitation. The stay laser light was blocked by a color filter OG530 or OG550. The emission for a single ablation pulse was recorded on a multichannel analyzer, and the ion charge reaching the collector plate was also recorded.

Fluorescence and current results for one pulse are shown in Fig. 7-2. The time scale of emission signal was adjusted by a factor of 2 in order to compare to the current signal because the $Ba^+$ ions were excited half way along the drifting distance. Due to the good time correlation between the signals of ion current and emission photons, we believe that this is a true fluorescence signal from the $Ba^+$ ions. Since particles move in the liquid at a different rate, we can reject the uncorrelated scattering signal from particles by accepting fluorescence signal only in a specified time window.

Because $Ba^+$ ions were not created continuously in liquid xenon, excitation spectra were obtained by taking such data for about 10 pulses for each excitation wavelength. The total number of detected emission photons, normalized by the laser power and the $Ba^+$ ion charge, as a function of the excitation wavelengths is shown in

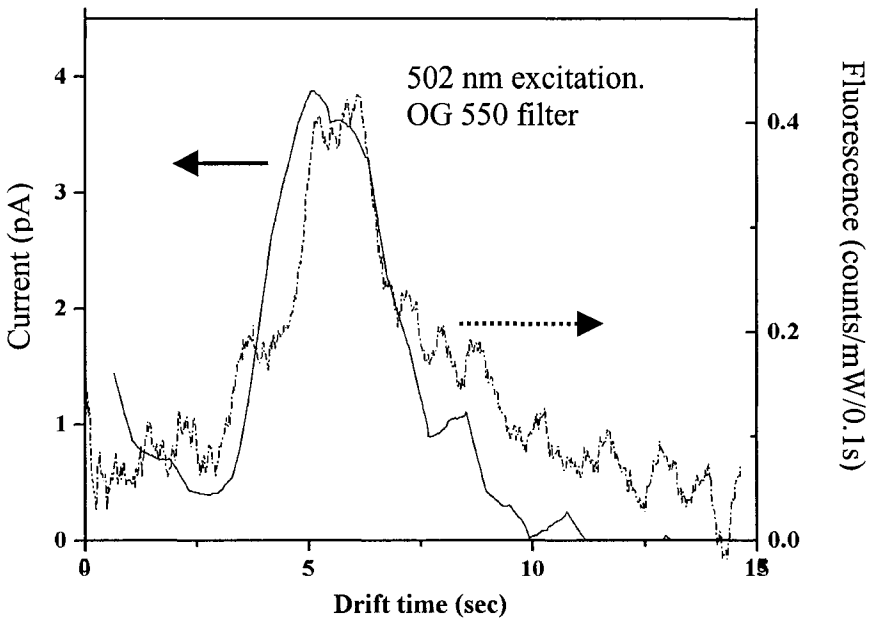


**Figure 7-2 Time correlation of the fluorescence (dot line) and ions drift (solid line) signals from a single pulse of $Ba^+$ ions.**

Fig. 7-3. This is the excitation spectrum. The emission signal excited by 514 nm was ignored because the OG 530 filter cannot attenuate the stray light sufficiently at this wavelength. There are two excitation peaks around 470 nm and 505 nm with only modest broadening (~15 nm) and red shift (10-20 nm) relative to the 6s-6p atomic resonance in vacuum. Whether or not there is a third peak, as we have guessed, below 450 nm is not clear because the error bar of the 454 nm excitation is large due to the small laser power, and no other laser lines with wavelength less than 450 nm were available to excite the $Ba^+$ ions.

These experimental results indicate that the structure of $Ba^+$ in liquid xenon is more like $Ca^+$ in solid argon and $Ba^+$ in liquid helium, which have absorption bands of modest width and shift, than alkali atoms in solid matrices, which show broad absorption bands and large red shifts of the emission. This is an important result in our quest to determine the requirements for single $Ba^+$ ion detection in a $\beta\beta$ decay experiment.

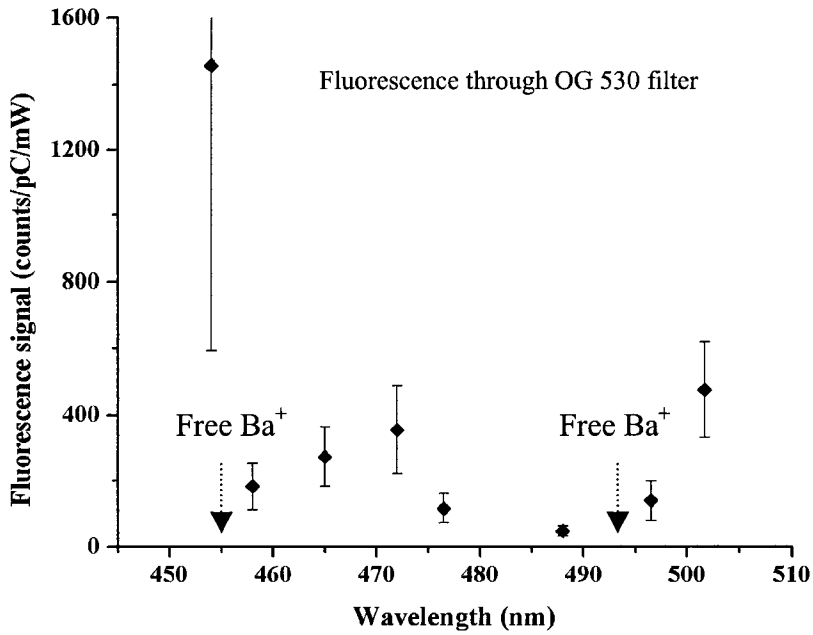


**Figure 7-3 Excitation spectrum of $Ba^+$ in liquid xenon.**

Another run of excitation spectrum where one OG 550 color filter was used to block all the argon laser wavelengths, including 514 nm, is shown in Fig. 7-4. The excitation wavelengths ranged from 488 nm to 514 nm, are covering the expected $S_{1/2} \rightarrow P_{1/2}$ transition only. The result is consistent with the previous data, and indicates a bandwidth of about 13 nm and a maximum excitation wavelength of around 508 nm.

In conclusion, the excitation spectra of $Ba^+$ ions in LXe have been studied, and our preliminary data indicates that the best excitation laser for our final goal is a wavelength around 470 nm or 505 nm in order to excite the $Ba^+$ efficiently. More data is required to improve the quality of these spectra.

## 7-3. Fluorescence spectra

A rough fluorescence spectrum can be obtained by detecting the total number of emission photons through various color filters. Since the color filters have different

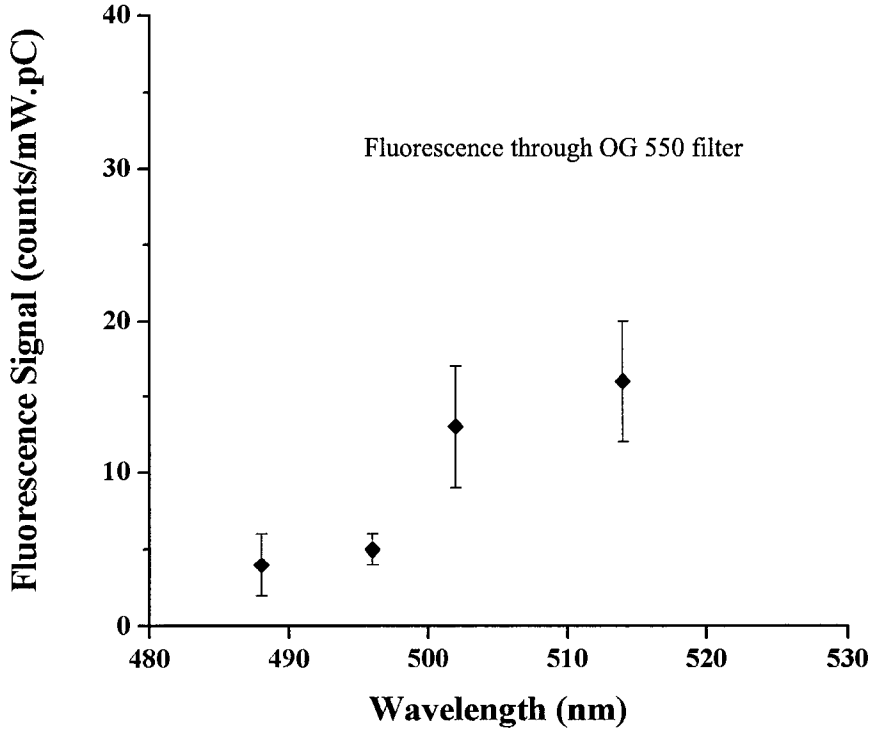


**Figure 7-4 Excitation spectrum of $Ba^+$ ions in liquid xenon.**

transmission ranges for fluorescence, the rough fluorescence spectrum is determined by measuring the emission photons versus color filter cutoff wavelength. Such a measurement is shown in Fig. 7-5, where $Ba^+$ ions were excited by 465 nm, and the total emission photons were detected through the color filters OG 530, OG 550, OG 590, RG 610, RG 665 and RG 695. The emission spectrum should be the negative of the derivative of this curve. Because the detected signal has a big drop around 530 nm, this curve indicates that the center of the fluorescence spectrum might be around 530 nm or below. Unfortunately, the large error bars in the data prevent a firm conclusion.

A detailed spectrum of fluorescence can be obtained by using a spectrometer. An apparatus for laser-induced fluorescence spectrum measured by a spectrometer with PMT in the early experiments is shown in Fig. 5-20. The fluorescence signal for one wavelength was recorded by setting the grating of a spectrometer at this wavelength. The

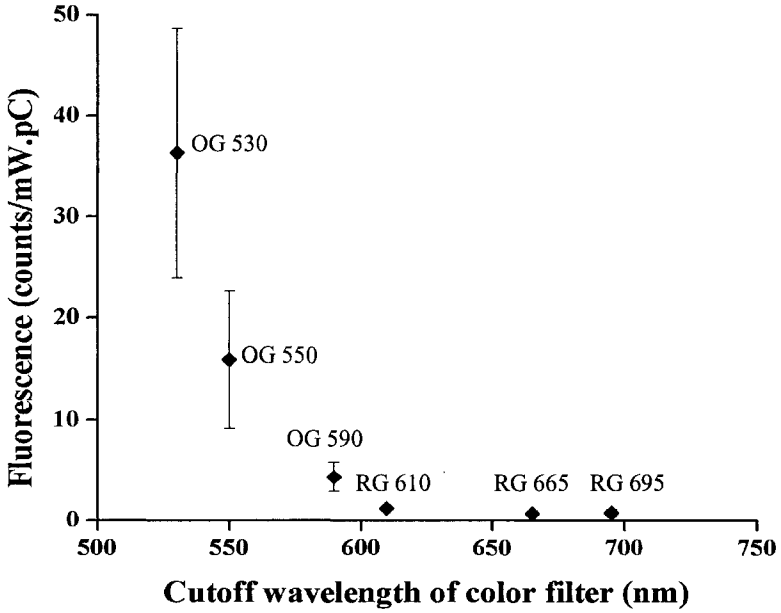


**Figure 7-5 Fluorescence signal of $Ba^+$ in LXe excited by 465 nm and detected through various color filters.**

PMT signal and the ion current signal were both recorded as shown in Fig. 7-6 for example. The fluorescence signal shows spiky peaks perhaps because the ion density was not uniform, and the fluid motion causes the ions to move in and out of the narrow region imaged on the input slit of spectrometer. The whole fluorescence spectrum was obtained by tuning the grating across the interested wavelength regions. Two fluorescence spectra of $Ba^+$ ions in LXe excited by 502 nm are shown in Fig. 7-7. It is not easy to locate the peak in the spectrum by these two results because shot-to-shot variations in the number of ablated ions in the observation volume probably dominate the true wavelength dependence. Nevertheless, it is likely that there is true emission observed in the 510 nm-550 nm regions.

Another method to record the fluorescence spectrum was by scanning the grating continuously (~12 nm/min) while applying laser ablation shots at a high rate of a few Hz.

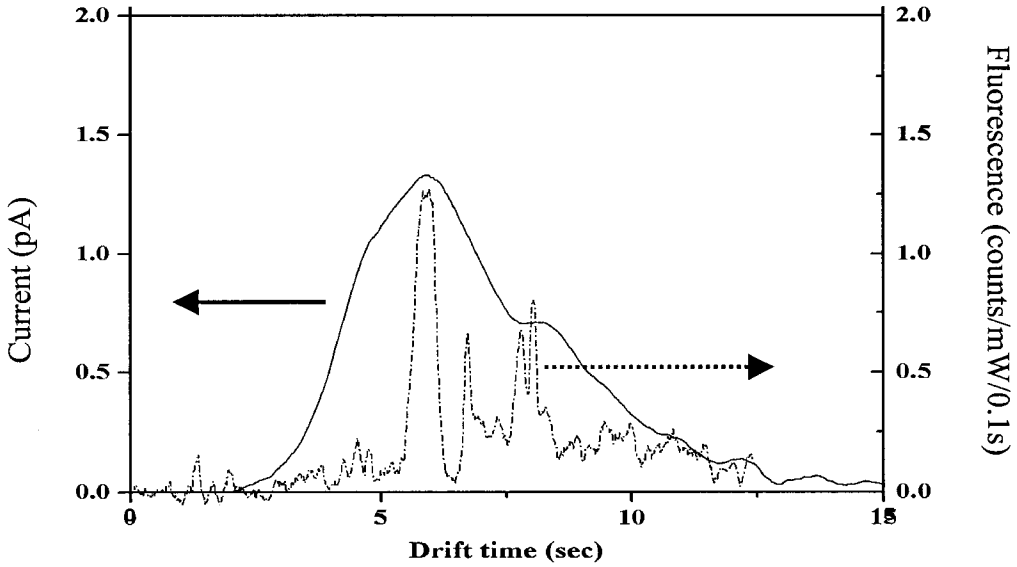


**Figure 7-6 Fluorescence (dot line) excited by 502nm and ion drift signal (solid line) from a single pulse of $Ba^+$ ions. The fluorescence was detected through a spectrometer set at 506nm.**

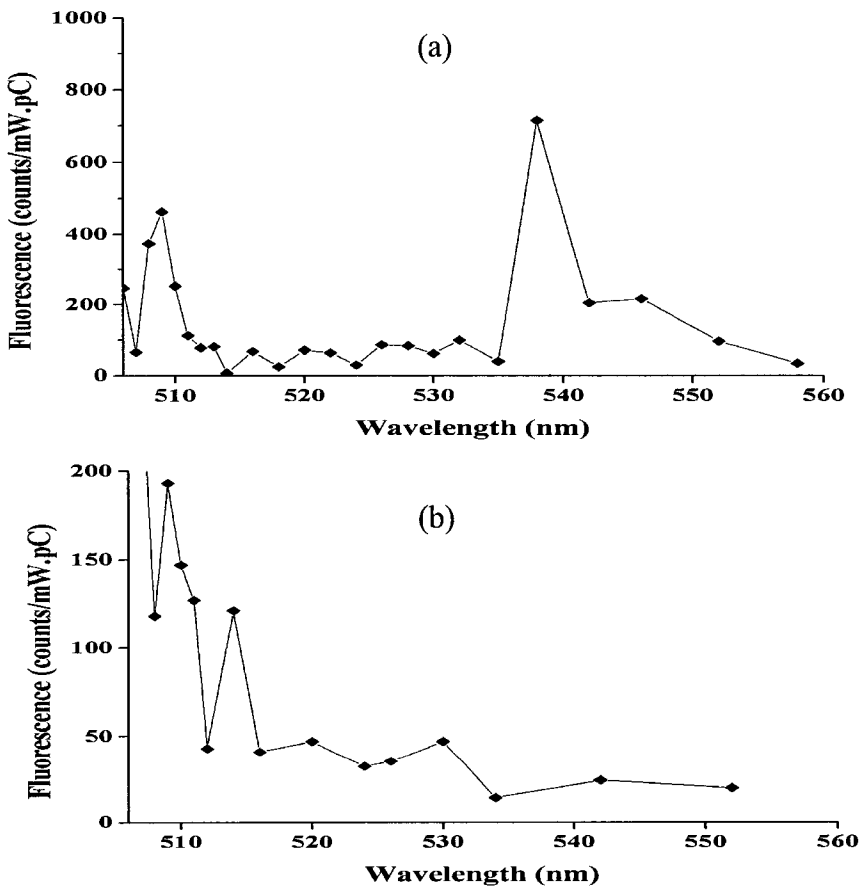


**Figure 7-7 Fluorescence spectrum of $Ba^+$ ions in LXe excited by 502 nm and detected by a spectrometer with a PMT. (a) and (b) were runs on different days.**

Because of the slow movement of the ions through the liquid, this produces, in theory, a nearly continuous ion density in the liquid. The typical results are shown in Fig. 7-8 (a) and (b), with 458 nm and 502 nm excitation respectively. However, due to the large variation of ion production in different laser shots, the whole spectrum again shows very spiky features. Nevertheless, the experimental data indicate the dominant fluorescence might be in the range above 510 nm and possibly also below 490 nm. An increasing signal below 470 nm in Fig. 7-8(a) is due to the stray light getting through the spectrum.

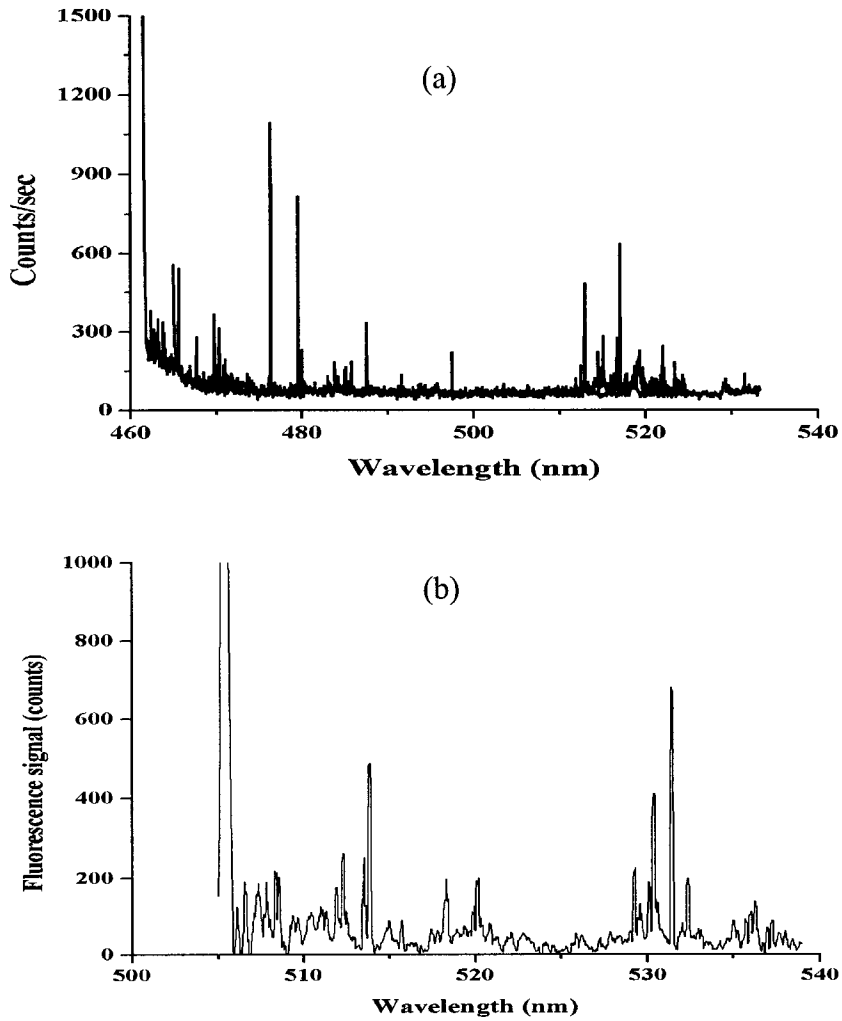


**Figure 7-8 Fluorescence spectra of $Ba^+$ ions in LXe excited by (a) 458 nm and (b) 502 nm with continuously laser ablation and wavelength scanning.**

The problem of shot-to-shot variation in ion production by laser ablation can be solved if the whole spectrum can be recorded by one ablation shot. That is the benefit of using a CCD array detector rather than a PMT. Fig. 7-9 (a)-(e) show recent fluorescence spectra excited by 458 nm, 465 nm, 496 nm, 502 nm and 514 nm and recorded by a CCD array detector at the output of a spectrometer. The results are clearly superior to the previous data. In all cases, a smooth broad emission band is observed.

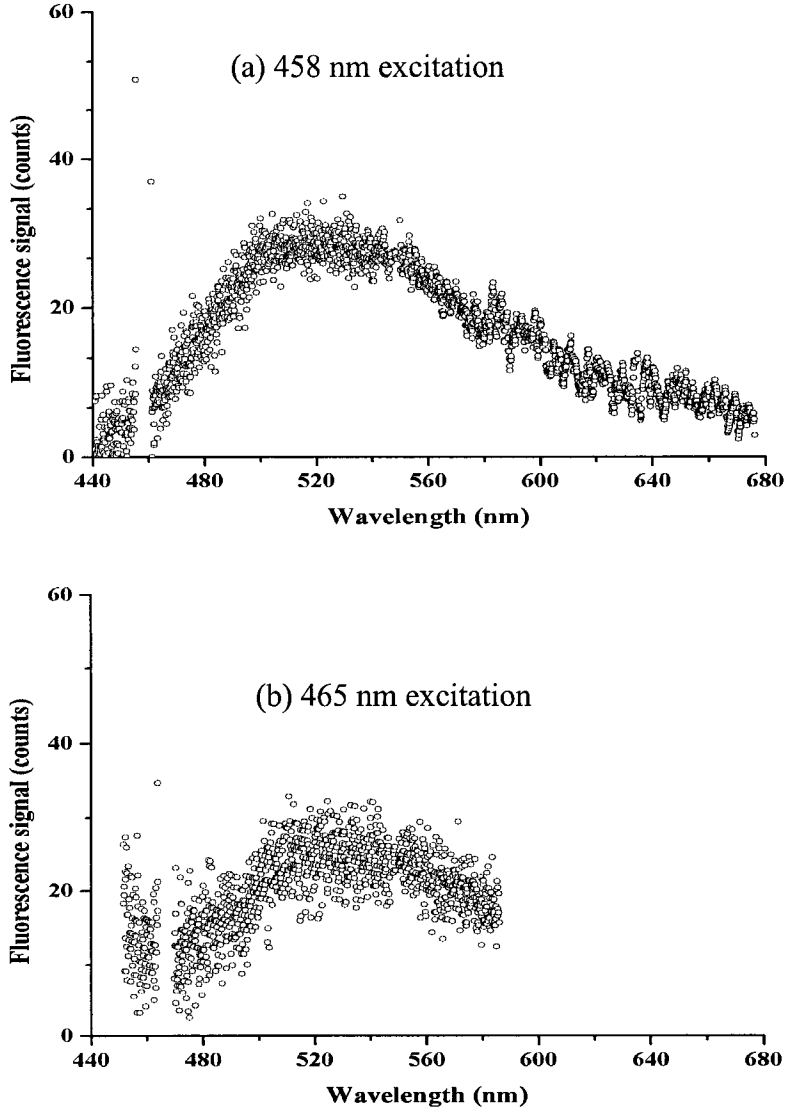


**Figure 7-9 Fluorescence spectra of $Ba^+$ ions in LXe excited by (a) 458 nm, (b) 465 nm, (c) 496 nm, (d) 502 nm and (e) 514 nm.**

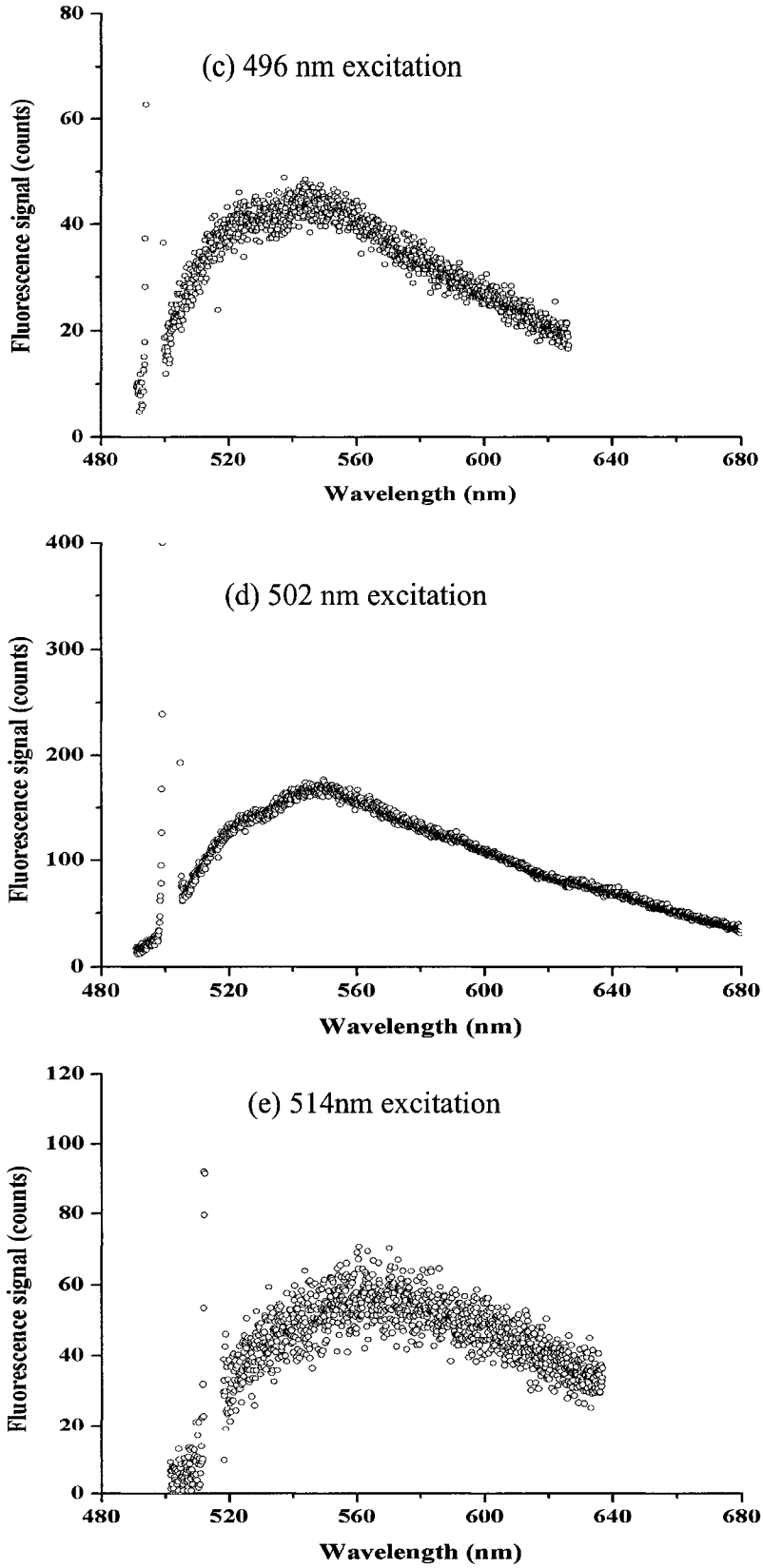


**Figure 7-9 Fluorescence spectra of $Ba^+$ ions in LXe excited by (a) 458 nm, (b) 465 nm, (c) 496 nm, (d) 502 nm and (e) 514 nm.**

There exists a residual peak at the excitation wavelength even though we have used a holographic notch filter to reduce scattered light at the laser wavelength. In order to confirm that the broad bands are not due to scattered stay light in the spectrometer, the detected scattered photons in the peak at the excitation wavelength are summed and compared to the total emission photons in the broad band. The fluorescence counts versus the stray light for three different excitation wavelengths are plotted in Fig. 7-10. There can be two orders of magnitude difference in fluorescence for the same level of scattered light. Thus it is believed that the broad emission is from the real fluorescence signal and not from scattering, e.g. from particles.

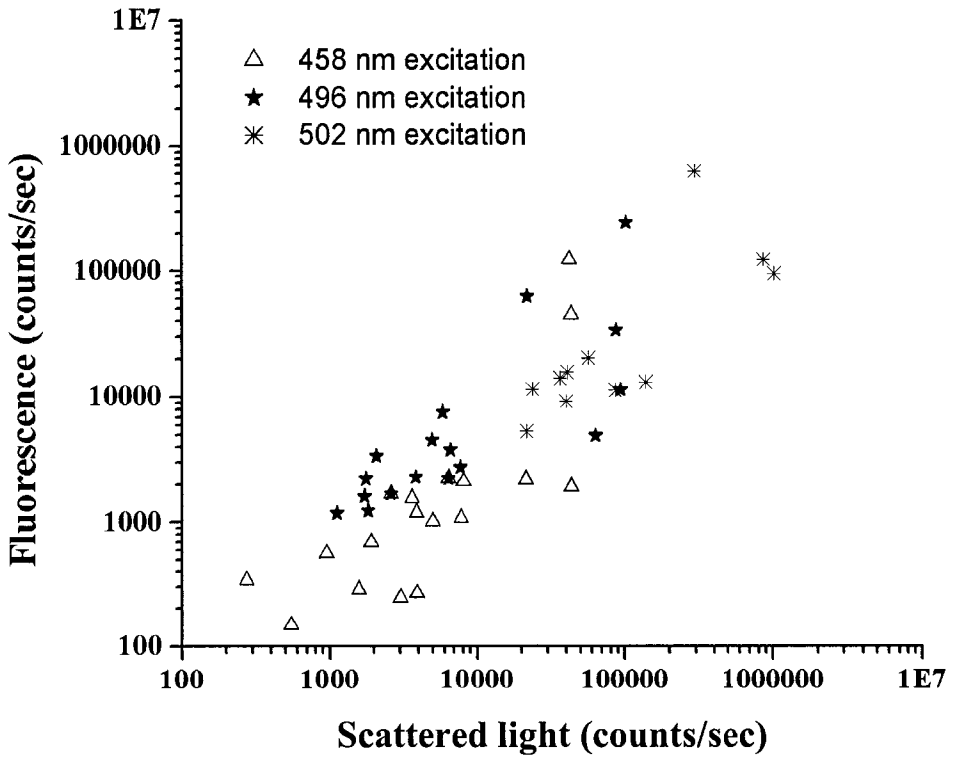


**Figure 7-10 Fluorescence vs. Scattered light for $Ba^+$ ions in LXe excited by 458 nm, 496 nm and 502 nm.**

For excitation of the $S_{1/2} \rightarrow P_{1/2}$ transition at 496 nm, 502 nm, and 514 nm, a broad emission band with a peak around 550 nm and a width of ~ 70 nm is observed. For excitation of the $S_{1/2} \rightarrow P_{3/2}$ transition at 458 nm and 465 nm, the emission peak is around 525 nm. The $S_{1/2} \rightarrow P_{1/2}$ laser-induced fluorescence spectrum is remarkably similar to bump #2 in the plasma emission spectrum of Fig. 7-1(b). The fluorescence spectrum excited by 465nm is consistent with the result of the color filter experiment shown in Fig. 7-5.

Although we have taken spectra out to 1000 nm, we did not see any emission in a second band which might correspond to the P→D transition. It is not clear at present if the P→D emission is absent. Two other possibilities are that the P→D emission is already imbedded in the single broad emission band, or that the emission is beyond 1000nm.

It should be noted that fluorescence spectra such as these were observed for every ablation shot only if the excitation laser was directed just below the liquid xenon level. Thus it is possible that in some cases the $Ba^+$ ions survive only a very short distance from the liquid surface. More research is needed. An onsite impurity monitor might be helpful to clarify the role of impurities in this problem.

In conclusion, our results for fluorescence measurements have shown $Ba^+$ ions in liquid xenon do fluoresce after laser excitation. The spectra obtained by different methods are consistent. Thus, although much remains to be demonstrated, the method for tagging $Ba^+$ daughter by lasers in liquid xenon is promising.

## 7-4 Ion cloud fluorescence image

By using the CCD camera directly in imaging mode, as shown in Fig. 5-23 and Fig. 5-24, it is possible to take snapshots of the fluorescence of the $Ba^+$ ion cloud as the ions drift in liquid xenon and are excited by an expanded $Ar^+$ laser beam. By using an expanded laser beam with diameter around 6 mm, the $Ba^+$ ions can be excited over the whole drift path, and the detected photons signal can tell us how the $Ba^+$ ions move and survive along the path, and are not charge exchanged or joined chemically with the other impurities. Two different types of images are shown in Fig. 7-11, where the exposure time was 5 seconds. The image (a), excited at 502 nm is broad and is thought to be a fluorescence image. The image (b), excited at 476 nm, is sharp, and might be due to particle scattering. Although a notch filter and a color filter were used to block the stay light, some residual particle scattering was still observed.

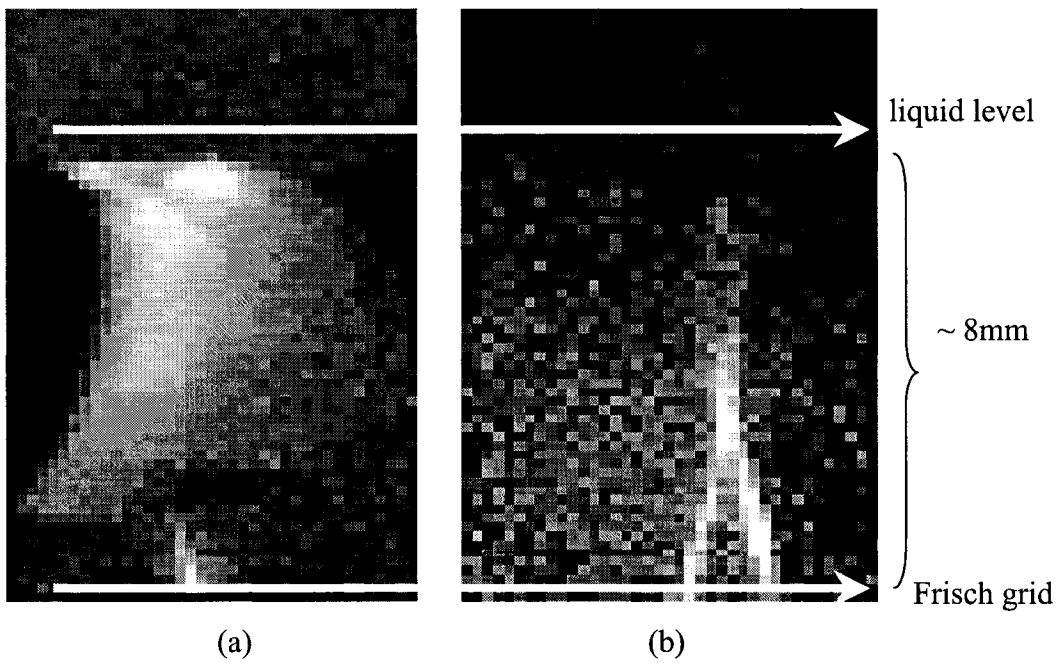


**Figure 7-11 $Ba^+$ cloud fluorescence images excited by (a) 502 nm (possible $Ba^+$ fluorescence) and (b) 476 nm (possible particle scattering).**

We do not have very conclusive results for the fluorescence images at present. More studies in the near future are needed to investigate this approach. It is hoped that the fluorescence image can be used to determine the ion survival time along the path from the magnitude of emission rate. No ion identification has been done in the mobility measurements of Chapter 6. From the data of Fig. 7-2 and from fluorescence images, it may be possible for the first time to relate a measured ionic mobility with an optically identified species.

## 7-5 Comparison of detected signal levels with predictions

The total emission rate of photons upon laser excitation of $Ba^+$ ions in LXe is discussed in section 4-3-2. The total fluorescence count rate, $R$, emitted by one $Ba^+$ ion per second upon excitation by a laser power $P$ without optical pumping is given as

$$R = \frac{\sigma}{A}\frac{P}{h\nu}\varepsilon, \qquad 7\text{-}1$$

and the maximum emitted photons $N$ with optical pumping is given as

$$N = \frac{1-\eta}{\eta}\varepsilon, \qquad 7\text{-}2$$

where $\eta$ is the branching ratio (~0.2 for free $Ba^+$), $\sigma$ is the absorption cross section, $A$, and $h\nu$ are the laser excitation area and photon energy of the excitation laser, respectively. The total detection efficiency, $\varepsilon$, including the quantum efficiency of a detector, collection efficiency of optics, optics and filter transmission *et al.* have been discussed in Section 5-8 and summarized in Table 5-3 for different experimental configurations.

The expected fluorescence photons of $Ba^+$ in LXe excited at 502nm for various experiments are then estimated and summarized in Table 7-1. In the bottom line, a consistent trend is seen that the measured counts are less than predicted for no optical

pumping and are larger than predicted for full optical pumping. This preliminary result indicates that the optical pumping effect might occur partially or that $Ba^+$ ions do not survive 100 % in the detection region because of the impurities. Although our conclusion is not firm, our results might suggest that the optical pumping for $Ba^+$ in liquid xenon is not as severe as in the vacuum. There might be a relaxation channel on the forbidden D to S transition for $Ba^+$ in the liquid xenon environment. Although it is only a partial optical pumping effect, it might be possible to increase the laser-induced emission rate by countering the optical pumping effect with a second laser which excites the D→P transition. In the future, a red diode or a dye laser is needed to study the spectrum of the P↔D transition. If the optical pumping effect is confirmed, one excitation laser for S→P and one optical pumping laser for D→P might be required to fulfill the laser tagging technique.

**Table 7-1 Comparison between predicted and measured fluorescence in three types of experiments.**

| Configuration | | Figure 5-16 Excitation | | Figure 5-20 Fluorescence | | Figure 5-23 Image | |
|---|---|---|---|---|---|---|---|
| Optical pumping | | no | yes | no | yes | no | yes |
| | unit | | | | | | |
| Laser power | mW | 83 | | 21 | | 17 | |
| Wavelength | nm | 502 | | 502 | | 502 | |
| Input photons | $sec^{-1}$ | $2\times10^{17}$ | | $5\times10^{16}$ | | $4\times10^{16}$ | |
| Laser beam area (A) | $cm^2$ | 0.04 | | 0.04 | | 0.36 | |
| Absorption cross section | $1/cm^2$ | $4\times10^{-16}$ | | $4\times10^{-16}$ | | $4\times10^{-16}$ | |
| Emitted photons/ion/sec | | 2080 | 4 | 525 | 4 | 47 | 4 |
| Total detection efficiency | | $1.5\times10^{-5}$ | $1.5\times10^{-5}$ | $4.2\times10^{-6}$ | $4.2\times10^{-6}$ | $8.0\times10^{-4}$ | $8.0\times10^{-4}$ |
| Predicted counts/ion/sec | | $3.1\times10^{-3}$ | $6.0\times10^{-5}$ | $2.2\times10^{-3}$ | $1.7\times10^{-5}$ | $3.8\times10^{-2}$ | $3.2\times10^{-3}$ |
| Transit time | sec | 1 | 1 | 1 | 1 | 1 | 1 |
| Predicted counts/ion | | 0.031 | 0.00006 | 0.0022 | 0.000017 | 0.038 | 0.0032 |
| Measured counts/ion | | 0.0023(9) | | 0.00048(24) | | 0.0058(7) | |
| Ratio: measured/predicted | | 0.07 | 38 | 0.22 | 29 | 0.15 | 1.8 |

# References

1. L.C. Balling and J.J. Wright, J. Chem. Phys. 83, 2614 (1985).

# Chapter 8

## Conclusions

Mobility measurements of alkaline earth ions in liquid xenon are reported for the first time in this thesis. The main systematic error from charge-induced fluid motion is studied and corrected, and a true mobility is obtained by a global fit. The mobility of the ions $Mg^+$, $Ca^+$, $Sr^+$, $Ba^+$ and $Tl^+$ does show a difference, and it may depend on the ionic radius or mass. A more detailed theoretical model is needed in future to understand these differences. The mobility of a $Ba^+$ ion in liquid xenon is found to be small, $0.000201^{+31}_{-21}$ $cm^2V^{-1}s^{-1}$. Therefore it should be easy to follow the slow moving $Ba^+$ in LXe with a tagging laser, and allow for a long tagging time to increase S/N for good single $Ba^+$ ion decay daughter identification. The ionic mobility is finally given as $0.000242^{+33}_{-31}$ $cm^2V^{-1}s^{-1}$, $0.000272^{+37}_{-31}$ $cm^2V^{-1}s^{-1}$, $0.000242^{+51}_{-43}$ $cm^2V^{-1}s^{-1}$, and $0.000171^{+30}_{-19}$ $cm^2V^{-1}s^{-1}$ for $Mg^+$, $Ca^+$, $Sr^+$ and $Tl^+$, respectively.

Laser spectroscopy of $Ba^+$ in liquid xenon is also studied for the first time. No previous fluorescence or absorption spectra exist for any ion in a liquid noble gas except in superfluid helium. A narrower width of absorption and smaller red shift of fluorescence are observed compared to the alkali atoms in solid matrices. It is observed that $Ba^+$ ions do fluoresce in LXe, which is a good sign for our final goal. Consistent $^2P_{1/2} \rightarrow {}^2S_{1/2}$ emission spectra are obtained in different types of experiments. Preliminary results agree with theoretical predictions, assuming some, but not complete optical pumping. These show some D→S decay or D→P excitation by the pump laser may occur.

The laser spectroscopy of the D↔P transitions is uncertain at this time. More investigation of the optical pumping effect is needed to increase the emission rate for the final single ion detection experiment. More careful confirming measurements need to be made to set the final conclusion of laser spectroscopy of $Ba^+$ in LXe.

Impurities in liquid xenon are always an important continuing issue in our studies. An in situ impurity monitor, such as a residual gas analyzer or a radioactive decay energy peak width monitor is needed to analyze the effectiveness of purification system and the residual level of impurities in the gaseous and liquid xenon. Another onsite impurity monitor operated in liquid xenon might be also required to determine the electronegative impurities. The final unambiguous identification of ions might be from their characteristic laser spectroscopy although it is difficult to apply such technique in liquid and not every ion has suitable light source to excite them.

A true test of single ion detection with lasers might be demonstrated by a $Ra^+$ ion rather than a $Ba^+$ ion because single $Ra^+$ ion can be produced and ejected into liquid xenon from a surface by α-decay of $^{221}Fr$ or $^{226}Th$ through the following decay chains,

$^{225}Ac(\alpha,10d)\rightarrow{}^{221}Fr(\beta,4.8m)\rightarrow{}^{221}Ra(\alpha,29s)\rightarrow{}^{217}Rn(\alpha,0.6m)\rightarrow{}^{213}Po(\alpha,4\mu s)\rightarrow{}^{209}Pb$

$^{230}U(\alpha,21d)\rightarrow{}^{226}Th(\alpha,31m)\rightarrow{}^{222}Ra(\alpha,38s)\rightarrow{}^{218}Rn(\alpha,35ms)\rightarrow{}^{214}Po(\alpha,164\mu s)\rightarrow{}^{210}Pb$

Fortunately, the energy levels and the second ionization energy of $Ra^+$ are very close to $Ba^+$ ions as shown in Table 8-1, so that $Ra^+$ should be a good test for $Ba^+$ single ion detection.

Our fluorescence results agree with predictions reasonably well. However, a higher power excitation laser, up to few watts, is needed in order to obtain enough emission to tag a single $Ba^+$ decay daughter. A re-pumping laser for the D→P transition

might be also required. According to our results and discussions of mobility and fluorescence, the proposed fluorescence technique to search for neutrino mass by identification of $0\nu\beta\beta$ decay $^{136}Ba^{+}$ daughters in liquid xenon in a neutrino mass search is very promising. Thus the next generation experiment of $0\nu\beta\beta$ decay of xenon with a large-scale detector mass and this unique and efficient background reduction method has a good chance to reveal the neutrino mass structure.

**Table 8-1 Energy levels of singly charged $Ra^{+}$ and $Ba^{+}$**

| $Ba^{+}$ | | $Ra^{+}$ | |
|---|---|---|---|
| $Ba^{++}$ | 10.004 eV | $Ra^{++}$ | 10.147 eV |
| $6P_{3/2}$ | 2.7218 eV | $7P_{3/2}$ | 3.2495 eV |
| $6P_{1/2}$ | 2.5121 eV | $7P_{1/2}$ | 2.6472 eV |
| $5D_{5/2}$ | 0.7036 eV | $6D_{5/2}$ | 1.7039 eV |
| $5D_{3/2}$ | 0.6043 eV | $6D_{3/2}$ | 1.4983 eV |
| $6S_{1/2}$ | 0 eV | $7S_{1/2}$ | 0 eV |